CONTENTS

ABSTRACTS

Maciej Rosół, Bogdan Sapiński

Autonomous Control System for a Squeeze Mode MR Vibration Isolator in an Automotive Engine Mount

The investigated autonomous control system for a squeeze mode magnetorheological (MR) vibration isolator is based on an ultra-low power microcontroller MSP430F5529. The design structure of the control system and the dedicated real-time sys-tem are briefly presented and the laboratory testing data are summarised.

Artur Ganczarski, Michał Adamski

Tetragonal or Hexagonal Symmetry in Modeling of Yield Criteria for Transversely Isotropic Materials

Present work deals with modeling of failure criteria for transversely isotropic materials. Analysis comprises two classes of symmetry: Tsai-Wu tetragonal and new Tsai-Wu based hexagonal. Detail analysis of both classes of symmetry with respect to their ad-vantages as well as limitations is presented. Finally, simple comparison of differences between limit curves corresponding to cross sections by planes of transverse isotro-py, orthotropy and shear plane is done.

Tomasz Geisler, Piotr Rosikoń, Wojciech Sochacki, Sandra Topczewska

Functional and Structural Analysis of Wing Folding Mechanism Based on Cockchafer (Melolontha Melolontha)

Insects are among nature's most nimble flyers. In this paper we present the functional and structural analysis of wing joint mecha-nism. Detailed action of the axillary plates and their mutual interaction was also described. Because of the small dimensions of the wing joint elements and the limited resolution of the light microscope, the authors used a scanning electron microscope. Based upon the knowledge of working prin-ciples of beetle flight apparatus a wing joint mechanism kinematics model has been developed.

Maciej Ryś

Constitutive Modelling and Identification of Parameters of 316L Stainless Steel at Cryogenic Temperatures

In this work, a macroscopic material model for simulation two distinct dissipative phenomena taking place in FCC metals and alloys at low tem-peratures: plasticity and phase transformation, is presented. Plastic yielding is the main phenomenon occurring when the yield stress is reached, resulting in nonlinear response of the material during loading. The phase transformation process leads to creation of two-phase continuum, where the parent phase coexists with the inclusions of secondary phase. An identification of the model parameters, based on uniaxial tension test at very low temperature, is also proposed.

Tomasz Leszczuk

Evaluation of the Fertilizer Granules Strength Obtained from Plate Granulation with Different Angle of Granulation Blade

The goal of the paper was to assess the strength of the fertilizer granules obtained by non-pressure granulation method. The granulation pro-cess was carried out in plate granulator, according to the three-level experiment plan. A mixture of raw materials prepared in a Polish factory of agrochemicals for agriculture and horticulture was used as a study material and water was used as a wetting liquid. Granulator design pa-rameters and process parameters were treated as entrance sizes of the experiment. Three different angles of granulation blade were used in experiments. This paper presents: the results of study of equivalent diameter size and the impact of changes in the angle of granulating blade on the strength of obtained granulate. Pfost apparatus and a set of sieves used in granulometric sieve were utilized in this study. A relation was suggested $P_\infty = f(\alpha, \chi, n, w_w, t)$. The results were presented in the form of graphs and tables. Conclusions were presented.

Żaneta Anna Mierzejewska, Zbigniew Oksiuta

Failure Analysis of a Femoral Hip Stem Made of Stainless Steel after Short Time of Exposure

This paper describes a case study summarising the failure analysis of a stainless steel femoral stem, which failed prematurely within 36 months of exploitation in human body. In order to determine the mechanism of failure, a broken stem component were analyzed by means of macro-scopic and microscopic obserwations and hardness measurements. Metallurgical obserwations revealed that the tested material does fulfill ASTM requirements. Scanning electron microscopy images revealed the presence of stress-induced cracking. The results of the hardness re-vealed significant nonuniformity from the surface towards the inner part of the stem. It is assumed that any discontinuity or defect on the fracture surface of the stem acted as preferential site for a crack nucleation and propagation by fatigue until the cross section of stem was not able to sustain a load generated by a patient.

Jarosław Czaban, Dariusz Szpica

The Diagnostic System of A-604 Automatic Transmission

Automatic gearbox gains increasing popularity in Europe. Little interest in diagnosis of such type of transmission in Poland results from the fact of small share in the whole market of operated cars, so there is a lack of availability of special diagnostic devices. These factors cause issues of expensive repairs, often involving a replacement of subassembly to new or aftermarket one. To a small extent some prophylactic diagnostic tests are conducted, which can eliminate future gearbox system failures. In the paper, the proposition of diagnostic system of popular A – 604 gearbox was presented. The authors are seeking for the possibility of using such type of devices to functional elaboration of gearboxes after renovation. The built system pursues the drive of the researched object, connected with simulated load, where special controller, replacing the original one, is responsible for controlling gearbox operation. This way is used to evaluate the mechanic and hydraulic parts' state. Analysis of signal runs, registered during measurements lets conclude about operation correctness, where as comparison with stock data verifies the technical state of an automatic gearbox.

Magdalena Łępicka, Małgorzata Grądzka-Dahlke

Effect of Plasma Nitriding Process Conditions on Corrosion Resistance of AISI 440B Martensitic Stainless Steel

Martensitic stainless steels are used in a large number of various industrial applications, e.g. molds for plastic injections and glass moldings, automotive components, cutting tools, surgical and dental instruments. The improvement of their tribological and corrosion properties is a problem of high interest especially in medical applications, where patient safety becomes a priority. The paper covers findings from plasma nitrided AISI 440B (PN-EN or DIN X90CrMoV18) stainless steel corrosion resistance studies. Conventionally heat treated and plasma nitrided in N_2:H_2 reaction gas mixture (50:50, 65:35 and 80:20, respectively) in two different temperature ranges (380 or 450°C) specimens groups were examined. Microscopic observations and electrochemical corrosion tests were performed using a variety of analytical techniques. As obtained findings show, plasma nitriding of AISI 440B stainless steel, regardless of the process temperature, results in reduction of corrosion current density. Nevertheless, applying thermo-chemical process which requires exceeding temperature of about 400°C is not recommended due to increased risk of steel sensitization to intergranular and stress corrosion. According to the results, material ion nitrided in 450°C underwent leaching corrosion processes, which led to significant disproportion in chemical composition of the corroded and corrosion-free areas. The authors suggest further research into corrosion process of plasma nitrided materials and its degradation products.

Olesya Maksymovych, Iaroslav Pasternak, Heorhiy Sulym, Serhiy Kutsyk

Doubly Periodic Cracks in the Anisotropic Medium with the Account of Contact of their Faces

The paper presents complex variable integral formulae and singular boundary integral equations for doubly periodic cracks in anisotropic elastic medium. It utilizes the numerical solution procedure, which accounts for the contact of crack faces and produce accurate results for SIF evaluation. It is shown that the account of contact effects significantly influence the SIF of doubly periodic curvilinear cracks both for isotropic and anisotropic materials.

Tadeusz Kaczorek

Minimum Energy Control of 2D Positive Continuous-Discrete Linear Systems

The minimum energy control problem for the 2D positive continuous-discrete linear systems is formulated and solved. Necessary and sufficient conditions for the reachability at the point of the systems are given. Sufficient conditions for the existence of solution to the problem are established. It is shown that if the system is reachable then there exists an optimal input that steers the state from zero boundary conditions to given final state and minimizing the performance index for only one step ($q = 1$). A procedure for solving of the problem is proposed and illustrated by a numerical example.

AUTONOMOUS CONTROL SYSTEM FOR A SQUEEZE MODE MR VIBRATION ISOLATOR
IN AN AUTOMOTIVE ENGINE MOUNT

Maciej ROSÓŁ*, **Bogdan SAPIŃSKI****

*Faculty of Electrical Engineering Automatics Computer Science and Biomedical Engineering, Department of Automatics and Biomedical Engineering,
AGH – University of Science and Technology, Al. Mickiewicza 30, Kraków, Poland
**Faculty of Mechanical Engineering and Robotics, Department of Process Control,
AGH – University of Science and Technology, Al. Mickiewicza 30, Kraków, Poland

mr@agh.edu.pl, deep@agh.edu.pl

Abstract: The investigated autonomous control system for a squeeze mode magnetorheological (MR) vibration isolator is based on an ultra-low power microcontroller MSP430F5529. The design structure of the control system and the dedicated real-time system are briefly presented and the laboratory testing data are summarised.

Key words: MR Vibration Isolator, Control System, Controller

1. INTRODUCTION

The last decade has witnessed a major interest in squeeze-mode MR vibration isoslators (VI-MRs) (Farjoud et al., 2011; Kim et al., 2008; Zhang et al., 2011). The majority of previous research has been focused mainly on theoretical studies, e.g. Jolly and Carlson (1996) and Stanway et al. (2000). It is worthwhile mentioning that certain solutions for these type of VI-MRs have been patented (Kim, 2012; Sapiński, 2013).

The investigated autonomous control system (ACS) is designed to be used for control of a prototype squeeze-mode MR vibration isolator (VI-MR). The VI-MR is intended for use as an actuating element in a semi-active engine automotive mount system designed to reduce the engine's vibrations due to fluctuating inertia forces (caused by unbalanced element of the crank system), to fluctuations of the drive torque transmitted from the engine onto the drive system components and to the action of some random forces (Kamiński and Pokorski, 1983; Snamina and Sapiński, 2014).

The ACS is based on an ultra low power microcontroller MSP430F5529 (MSP430) (Texas Instruments INC, 2013). Prior to the fabrication of ACS, testing was done on a previously developed power driver dedicated for VI-MR and based on an integrated interface VNH2SP30-E (Rosół and Sapiński, 2014).

The ACS requires a dedicated real-time clock system, to enable the measurement of process variables and to develop the control method with the predetermined sampling period (Philip and Laplante). The quaranteed constatnt sampling period enables the usie of the theory of discrete control systems in developing control algorithms for VI-MR. Besides such approach allows to employ model-based design method in simulation, testing and implementation of regulators on the target hardware platform.

Measurement data from the ACS are monitored and processed using a serial bus Controller Area Network (CAN) (Bosch GmBH, 1991). This bus was selected as it is intended for use in control of the VI-MR to be installed in the engine mount in the vehicle where CAN acts as the primary data transmission interface.

The engineered ACS was tested in the laboratory conditions in two configurations: the open loop and in the feedback loop (with a PID controller) systems. Testing was done under the loading applied through the electromagnet coil whose resistance and induction were similar to the parameters of the control coil in the VI-MR.

2. DESIGN STRUCTURE

The block diagram of the ACS, shown in Fig. 1, comprises the following units: the MSP430 block with analogue and digital signal outputs, the measurement block, the CAN interface, the power-supply and the USB interface.

The key component of the ACS is the MSP430 supporting the measurement and control application. The MSP430 features high program memory and data memory capacity, numerous integrated peripherals (USB, SPI, 12C, UART, an A/D converter, a multiply unit) and the supply voltages can be generated via an USB port. The major technical parameters of the MSP430 are summarised in Tab. 1.

The MSP430, the measurement block and the CAN bus block are supplied with voltages +5 V and +3/3 V from the power supply block. The ACS may be supplied via a micro-USB port (+5 V) or from a power supply unit delivering the voltage in the range (+3.3, +12) V.

The measurement block incorporating the system for conditioning four analogue signals enables the gain and offset control, so the sensors operating in the voltage range ±10 V can be easily connected to the ACS. The voltage range handled by the measurement block necessitates the use of a DC/DC +5 V/±15 V converter in the power supply block. The MSP430 has an integrated USB interface which can be utilised for programming and data exchange with the microprocessor. The current levels to be han-

dled by the USB interface block are limited to 100 mA and the data lines D+ and D- are surge-voltage protected.

The CAN bus block enables the ACS communication with peripheral devices via the CAN bus. This block is implemented on an integrated SPI/CAN converter and a CAN transceiver. The maximal data transmission throughput is 1 Mbit/s.
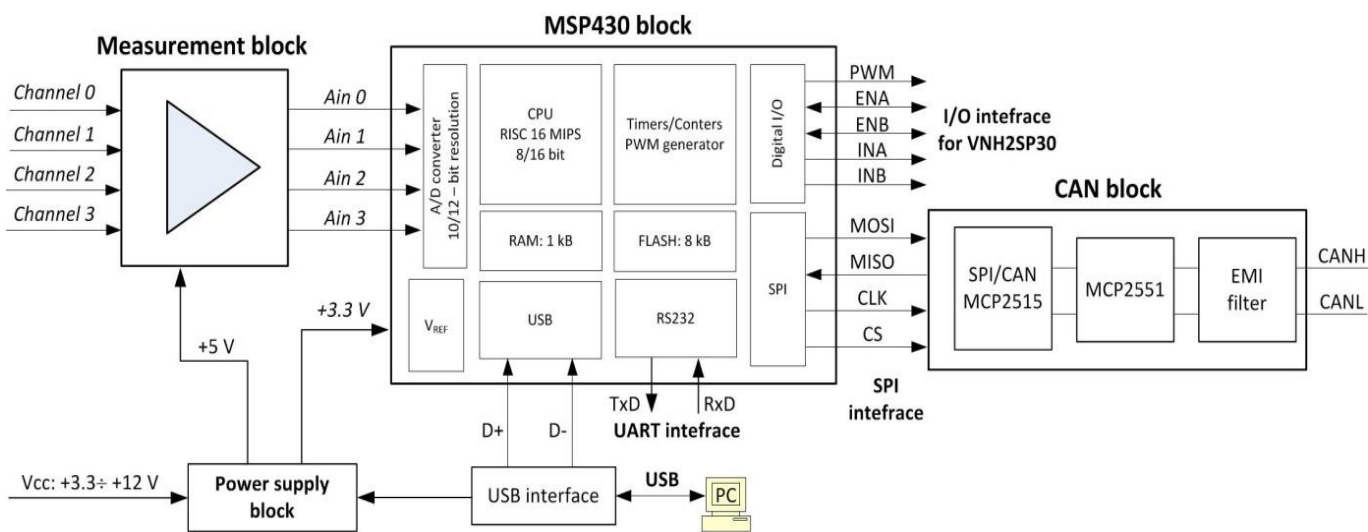

Fig. 1. Block diagram of the ACS

Tab. 1. Technical parameters of MSP430

Parameter	Description
Program memory	128 kB
Data memory SRAM	8+2 kB (additional 2 kB without USB)
I/O number	Max. 63
Number of Timers/Counters	4
Watchdog	Yes
PWM mode	Yes
Communication protocols (USCI)	Channel A: UART/LIN/IrDA/SPI Channel B: I2C/SPI
DMA	3 channels
Multiply unit (MPY)	32×32
Comparator	Yes
Integrated temperaturę sensor	Yes
A/D converter	12 channels, 12-bit
Integrated USB interface	Yes

3. TESTING

3.1. Laboratory setup

The schematic diagram of the laboratory set-up for ACS testing is shown in Fig. 2. The power interface and ACS are supplied from the battery +12 V. The monitoring and data acquisition are supported by a purpose-developed application written in the Lab-View and activated on a PC. The data transmission between the ACS and PC is effected via a sbRIO-9639 card equipped with the CAN interface (ACS connection) and the Ethernet (PC connection). The power interface ensures the current levels 11−12 A to be as required in the electromagnet coil.
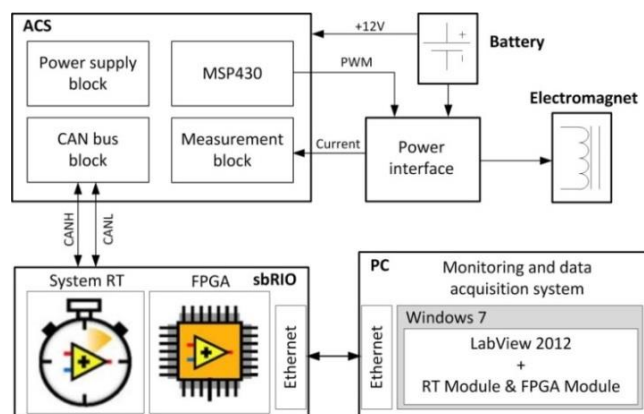

Fig. 2. Block diagram of the test configuration

The application supporting the operation of measurement sensors and control of the electromagnet coil is MSP430 enabled. The primary function of this application, written in the C/C++ language in the Code Composer Studio (CCS) environment is to generate the command signal basing on the current measured in the electromagnet coil, so that the current should be maintained on the preset level. Besides, the application configures and handles the digital analogue signals from the microcontroller (including the signals from the PWM signal generator, an A/C converter and the SPI interface supporting the communication with the SPI/CAN converter). To lend the controller a deterministic feature, the control algorithm is activated in the procedure of interruption from the timer. The time interval of this interruption is set to be 1 kHz. This value was selected basing on the transmissibility characteristics of the power interface, obtained for the VI-MR, shown in Fig. 3. The gain Mg is derived from formula (1).

$$\left| M_g \right| = 20 \log_{10} \left(\frac{I(f)}{\alpha(f)} \right) \tag{1}$$

where: I(f) – amplitude of current in the electromagnet coil at the frequency f, α(f) – amplitude of the PWM factor at the frequency f.

It appears that the maximal frequency of variations of the command signal is 188 Hz, which means that the minimal sampling frequency of the control algorithm should be equal to 376 Hz. The set-up for ACS testing is shown in Fig. 4.
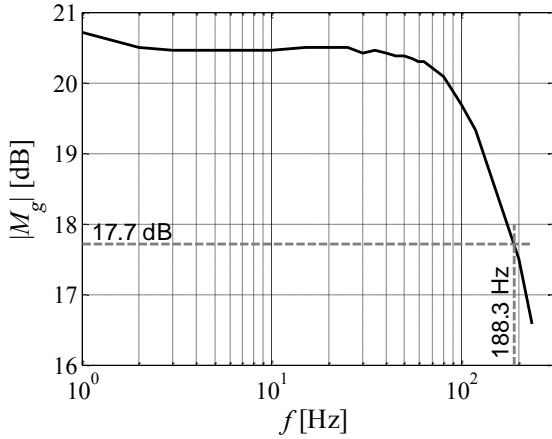

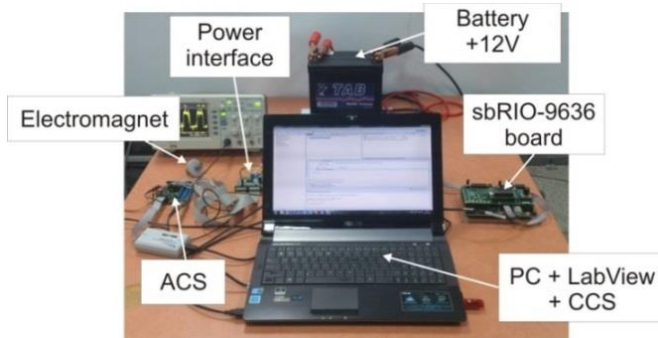**Fig. 3.** Transmissibility characteristics of the power interface for the VI-MR

Fig. 4. Set-up for ACS testing

3.2. Results

Testing was done on the ACS system in the open loop configuration (ACS-O) and in the closed-loop configuration (ACS-PID). The applied control signal was current i in the electromagnet coil. Electrical parameters of the electromagnet coil were: resistance 1.059 Ω, induction 1.13 mH.

The PI version of the PID controller, used in the ACS-PID system, is governed by the equation (2).

$$u(t) = u_0 + K_p \varepsilon(t) + \frac{1}{T_i} \int_o^t \varepsilon(\tau)d\tau \qquad (2)$$

$$\varepsilon(t) = i_0 - i(t) \qquad (3)$$

where: u(t) – control, u_0 – control value in the steady state, $\varepsilon(t)$ – control error, i_0 – preset current level in the coil, K_p – controller gain, T_i – integration time.

The parameters of the PI controller chosen using the parametric optimisation methods are: $K_p = 49.3$; $T_i = 1.74 \times 10^{-4}$. The integration function of the PI controller is approximated by the rectangle method.

Tab. 2. Time required for reaching the preset current level in the control coil

ACS \ i_0	1 A	3 A	5 A
ACS-O	1.92 ms	2.1 ms	1.96 ms
ACS-PID	1. 32 ms	1.36 ms	1.16 ms
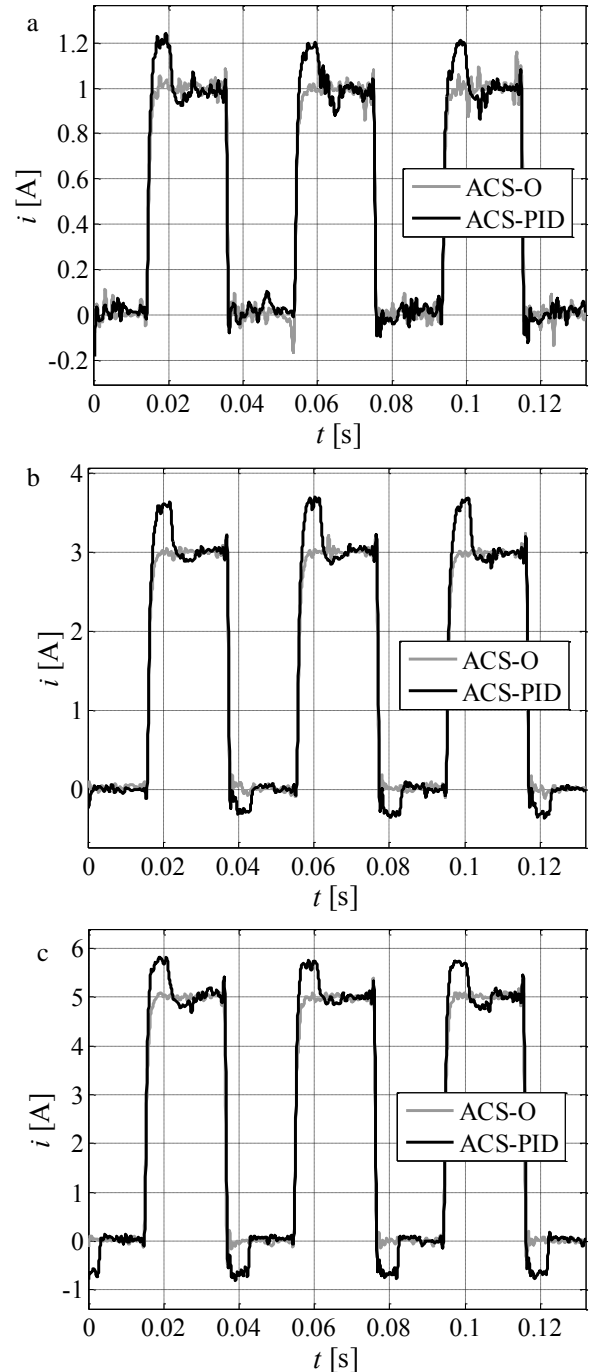
Fig. 5. Time patterns of current i: a) i_0=1 A, b) i_0=3 A, c) i_0=5 A

Testing of the ACS-O and ACS-PID system was done for the pre-defined PWM signal frequency (5 kHz) and the duty cycle α was varied from 0 to 1 with the step 0.1. As it was mentioned previously, the primary function of the ACS-PID system is to stabilise the current level in the electromagnet coil. This configuration of the system was tested for the preset current levels i_0: 1, 2, 3, 4, 6 A. The patterns of the PWM control and current in the coil

registered for the ACS-O and ACS-PID configurations are shown in Fig. 5, for i_0=1 A, i_0=3 A and i_0=5 A. The current $i(t)$ plots show that the required current level i_0 was reached in the electromagnet coil, both in the ACS-O and the ACS-PID configuration. Application of the PI controller allowed a 30% reduction of the time needed to reach the preset current level (see Tab. 2). One has to bear in mind, however, that for smaller values of i_0 these time intervals can become decidedly shorter.

4. SUMMARY

This paper summarises the structure design of an MSP430-based ACS and laboratory test data are provided. The engineered ACS was tested in the laboratory conditions in two configurations: the open loop and in the feedback loop configuration (with a PID controller). Testing was done under the loading applied to the power interface VI-MR through an electromagnet coil. Experimental results show that application of the PI controller allowed a 30% reduction of the time needed to reach the preset current level and force produced by VI-MR in real application.

It is worthwhile to mention that the selected microcontroller MSP430 has a sufficient computational power to implement algorithms and allows for expanding the ACS structure such that it should incorporate extra sensors and actuators. ACS tests will be repeated once the final version of the vibration isolator VI-MR has been developed.

REFERENCES

1. **Bosch GmBH** (1991), *CAN Specification, Version 2.0*, Stuttgart, www.bosch-semiconductors.de.
2. **Farjoud A., Craft M., Burke W., Ahmadian M.** (2011), Experimental investigation of MR squeeze mounts, *Journal of Intelligent Material Systems and Structures*, 22, 1645-1652.
3. **Jolly M. R., Carlson J. D.** (1996), *Controllable Squeeze-film Damping using MR fluid*, Proc. of Actuator, Bremen, Germany, 333−336.
4. **Kamiński E., Pokorski J.** (1983), *Dynamics of automobile suspensions and drive systems*, WKŁ, Warsow.
5. **Kim J. H.** (2012), Damping control device with magnetorheological fluid and engine mount having the same, *United States Patent Application Publication* US 2012/0132492A1.
6. **Kim K. J., Lee Ch. W., Koo J. H.** (2008), Design and modeling of semi-active squeeze film dampers using magnetorheological fluids, *Smart Materials and Structures*, 17, 035006, 12.
7. **Phillip. A. Laplante** (1997), *Real-Time Systems Design and Analysis*: An Engineer's Handbook, 2nd ed., 59.95, IEEE Press,. Piscataway, N.J., USA.
8. **Rosół M, Sapiński B.** (2014), Prototyping of a control system for a magnetorheological vibration isolator, *Modelling in Engineering* (to be published).
9. **Sapiński B.** (2013), Vibration isolator with MR fluid, *Bulletin of Polish Patent Office*, 17 (1034), 27.
10. **Snamina J., Sapiński B.** (2014), Analysis of an automotive vehicle engine mount based on squeeze-mode MR damper, *Journal of Cracow University of Technology* (to be published).
11. **Stanway R., Sims N. D., Johnson A. R.** (2000), *Modelling and control of a magnetorheological vibroisolator*, Proc. of SPIE, 3989, 184−193.
12. **Texas Instruments Inc.** (2013), *MSP430F5529 mixed signal microcontroller. Technical data*, www.ti.com.
13. **Zhang X. J., Farjud A., Ahmadian M., Guo K. H., Craft M.** (2011), Dynamic Testing and Modelling of an MR Squeeze Mount, *Journal of Intelligent Material Systems and Structures*, 22, 1717-1728.

TETRAGONAL OR HEXAGONAL SYMMETRY IN MODELING OF FAILURE CRITERIA FOR TRANSVERSELY ISOTROPIC MATERIALS

Artur GANCZARSKI[*], Michał ADAMSKI[*]

[*]Institute of Applied Mechanics, Department Mechanical Engineering,
Cracow University of Technology, 31-864 Kraków al. Jana Pawła II 37, Poland

artur.ganczarski@pk.edu.pl, michal.a.krakow@gmail.com

Abstract: Present work deals with modeling of failure criteria for transversely isotropic materials. Analysis comprises two classes of symmetry: Tsai-Wu tetragonal and new Tsai-Wu based hexagonal. Detail analysis of both classes of symmetry with respect to their advantages as well as limitations is presented. Finally, simple comparison of differences between limit curves corresponding to cross sections by planes of transverse isotropy, orthotropy and shear plane is done.

Key words: Transverse Isotropy, Tetragonal and Hexagonal Symmetry, Tsai-Wu Criterion

1. INTRODUCTION

Formulation of the initial yield or failure criteria for modern materials has to consider material anisotropy, tension-compression asymmetry or hydrostatic pressure sensitivity. In general, there exist two competitive but complementary schools to capture the above behaviours. The first explicit approach is based on a direct concept of common invariants of stress and anisotropy tensors (Sayir, 1970; Goldenblat and Kopnov, 1966; Tsai and Wu, 1971; Murakami, 2012; etc.) The second implicit approach is based on a direct extension of the isotropic-type yield/failure criteria to capture anisotropic behaviour as well as strength differential effect and pressure sensitivity by the use of linear transformation tensors for single stress invariants (Khan et al., 2007; Cazacu and Barlat, 2004 and others). Although the common invariants-based formulation is more mathematically rigorous, but complicated by the use of the second-, fourth-rank structural tensors, a direct extension of classical isotropic criteria to anisotropy is very efficient and broadly examined (Ganczarski and Skrzypek, 2014).

Basic result of the present paper is to propose the new orthotropic criterion of failure initiation, being the extended Tsai-Wu type equation. This new criterion is capable of capturing orthotropic limit surface description, without ellipticity loss even for arbitrarily high orthotropy degree. This is by contrast to the classical Tsai-Wu (1971) criterion (eg. Ottosen and Ristinmaa, 2005), where for high orthotropy degree inadmissible degeneration of the limit surface may occur. This enhanced Tsai-Wu's type limit surface is represented by the elliptic paraboloid, the axis of which is different from hydrostatic axis in the space of principal stresses, hence the criterion no longer satisfies the property of deviatoricity.

The other important feature of the proposed criterion is concerned with the particular case of transversely isotropic hexagonal symmetry, for which it is possible to achieve coincidence with the same proportion of isotropic Huber-von Mises-Hencky condition in the transverse isotropy plane, which may occur beneficial when compared to the deviatoric Tsai-Wu formulation for which above reducibility does not hold.

2. TRANSVERSELY ISOTROPIC TSAI-WU FAILURE CRITERION

In a general case of brittle materials that exhibit anisotropy (e.g. concrete, ceramic materials, rocks, composite materials, etc.) and tension-compression asymmetry, a transversely isotropic Tsai-Wu criterion of initial failure (Tsai and Wu, 1971) is applicable:

$$F[(\sigma_y - \sigma_z)^2 + (\sigma_z - \sigma_x)^2] + H(\sigma_x - \sigma_y)^2 + 2L\tau_{xy}^2$$
$$+ 2M(\tau_{zx}^2 + \tau_{zy}^2) + P(\sigma_x + \sigma_y) + Q\sigma_z = 1 \tag{1}$$

Eq. (1) contains only 5 independent material coefficients referring to appropriate tensile and compressive strengths k_{tx}, k_{cx}, k_{tz}, k_{cz} and shear strength k_{zx}, hence, in order to calibrate it the following tests must be performed:

$$\sigma_x = k_{tx} \quad \rightarrow \quad (F+H)k_{tx}^2 + Pk_{tx} = 1$$
$$\sigma_x = -k_{cx} \quad \rightarrow \quad (F+H)k_{cx}^2 - Pk_{cx} = 1$$
$$\sigma_z = k_{tz} \quad \rightarrow \quad 2Fk_{tz}^2 + Qk_{tz} = 1 \tag{2}$$
$$\sigma_z = -k_{cz} \quad \rightarrow \quad 2Fk_{cx}^2 - Qk_{cz} = 1$$
$$\tau_{zx} = k_{zx} \quad \rightarrow \quad 2Mk_{zx}^2 = 1$$

Solution of Eqs. (2) with respect to F, H, M, P and Q takes the form:

$$F = \frac{1}{2k_{tz}k_{cz}} \quad H = \frac{1}{k_{tx}k_{cx}} - \frac{1}{2k_{tz}k_{cz}} \quad M = \frac{1}{2k_{zx}^2}$$
$$P = \frac{1}{k_{tx}} - \frac{1}{k_{cx}} \qquad Q = \frac{1}{k_{tz}} - \frac{1}{k_{cz}} \tag{3}$$

Magnitude of material coefficient L, referring to shear strength in plane of transverse isotropy, is not independent and can be calculated from the following known relation (see Chen and Han, 1995 and Ganczarski and Skrzypek, 2013):

$$2L = 2(F + 2H) = \frac{4}{k_{tx}k_{cx}} - \frac{1}{k_{tz}k_{cz}} \tag{4}$$

Hence, after substitution of Eqs. (3)–(4) to Eq. (1) one can get

final form of the transversely isotropic Tsai-Wu criterion:

$$\frac{\sigma_x^2+\sigma_y^2}{k_{tx}k_{cx}} + \frac{\sigma_z^2}{k_{tz}k_{cz}} - \left(\frac{2}{k_{tx}k_{cx}} - \frac{1}{k_{tz}k_{cz}}\right)\sigma_x\sigma_y - \frac{\sigma_y\sigma_z+\sigma_x\sigma_z}{k_{tz}k_{cz}}$$
$$+\left(\frac{4}{k_{tx}k_{cx}} - \frac{1}{k_{tz}k_{cz}}\right)\tau_{xy}^2 + \frac{\tau_{yz}^2+\tau_{zx}^2}{k_{zx}^2} \tag{5}$$
$$+\left(\frac{1}{k_{tx}} - \frac{1}{k_{cx}}\right)(\sigma_x+\sigma_y) + \left(\frac{1}{k_{tz}} - \frac{1}{k_{cz}}\right)\sigma_z = 1$$

It is obvious that material coefficients in plane of transverse isotropy that precede terms $\sigma_x\sigma_y$ and τ_{xy} are not fully independent since they contain not only in-plane tensile and compressive strengths k_{tx}, k_{cx} but also out-of-transverse isotropy plane tensile and compressive strengths k_{tz}, k_{cz}. Consequently, Eq. (5) can be classified as the tetragonal transversely isotropic Tsai-Wu criterion of initial failure.

3. CONVEXITY LOSS IN CASE OF HIGH ORTHOTROPY

Applicability range of Tsai-Wu transversely isotropic criterion (5) to properly describe initiation of failure in some engineering materials that exhibit high orthotropy degree, is bounded by a possible elliptic form loss of the limit surface. In other words, a physically inadmissible degeneration of the single convex and simply connected elliptic limit surface into two concave hyperbolas surfaces occurs. The following inequality bounds the range of applicability for Hill's criterion (see Ottosen and Ristin-maa, 2005; Ganczarski and Skrzypek, 2013):

$$\frac{1}{k_{tz}k_{cz}}\left(\frac{4}{k_{tx}k_{cx}} - \frac{1}{k_{tz}k_{cz}}\right) > 0 \tag{6}$$

Substitution of the dimensionless parameter $R = 2(k_{tz}k_{cz}/k_{tx}k_{cx}) - 1$ (extension of Hosford and Backofen (1964) parameter), leads to the simplified restriction:

$$R > -0.5 \tag{7}$$

If the above inequalities (6)–(7) do not hold, elliptic cross sections of the limit surface degenerate to two hyperbolic branches and the loss of convexity occurs. To illustrate this limitation, the failure curves in two planes: the transverse isotropy (σ_x, σ_y):

$$\sigma_x^2 - \frac{2R}{1+R}\sigma_x\sigma_y + \sigma_y^2 + (k_{cx} - k_{tx})(\sigma_x+\sigma_y) = k_{tx}k_{cx} \tag{8}$$

and the orthotropy plane (σ_x, σ_z):

$$\sigma_x^2 - \frac{2}{1+R}\sigma_x\sigma_z + \frac{2}{1+R}\sigma_z^2 + (k_{cx} - k_{tx})\sigma_x$$
$$+k_{tx}k_{cx}\left(\frac{1}{k_{tz}} - \frac{1}{k_{cz}}\right)\sigma_z = k_{tx}k_{cx} \tag{9}$$

for various R–values, are sketched in Fig. 1a, b respectively. It is observed that when R, starting from R = 3, approaches the limit R = −0.5, the curves change from closed ellipses to two parallel lines in transverse isotropy plane or parabola in orthotropy plane, whereas for R < −0.5, concave hyperbolas appear. In general case of strong orthotropy, when the convexity condition (6) does not hold, the Tsai-Wu criterion (5) becomes useless. This effect is decribed in details for the case of Hill's (1948) orthotropic yield criterion (see Ganczarski and Skrzypek, 2013) from which Tsai-Wu's criterion obviously inherits all inconvenient features since the structure of quadratic terms of both conditions is analogous.
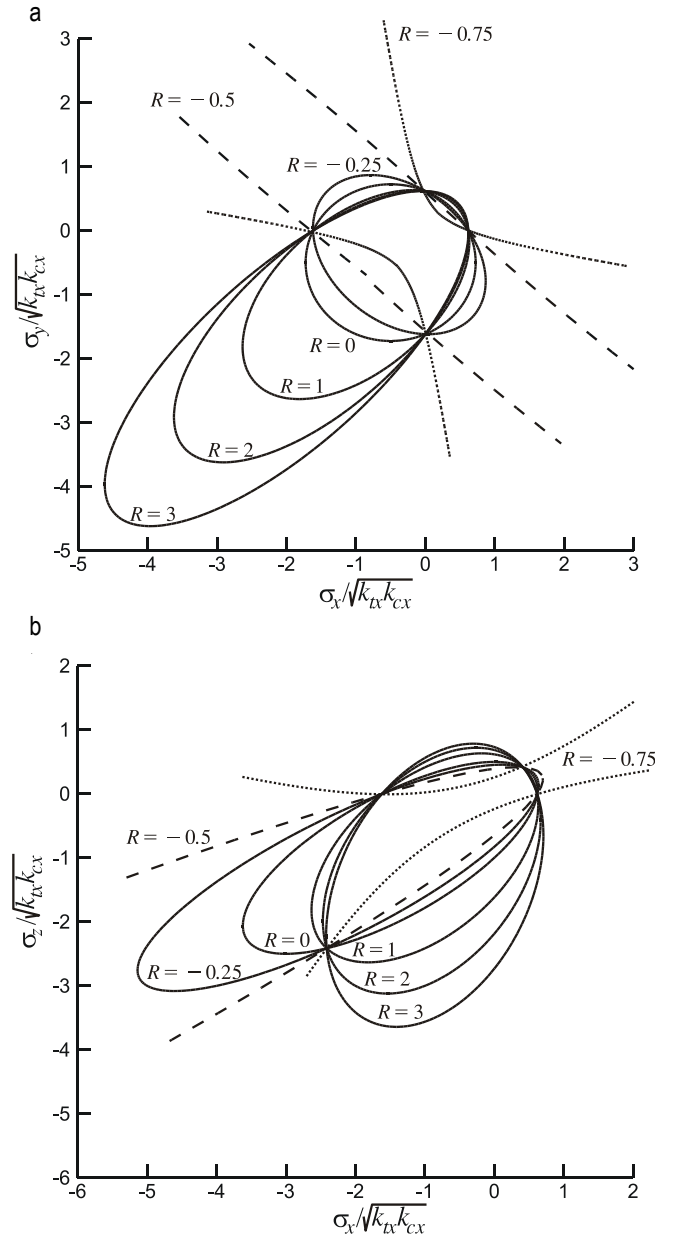
Fig. 1. Degeneration of the Tsai-Wu limit surface with the magnitude of the generalized Hosford and Backhofen parameter R: a) transverse isotropy plane, b) orthotropy plane

4. MODIFIED TSAI–WU BASED HEXAGONAL FAILURE CRITERION

Except the tetragonal transversely isotropic Tsai-Wu criterion Eq. (5) one can introduce hexagonally isotropic Tsai-Wu failure criterion:

$$\frac{\sigma_x^2-\sigma_x\sigma_y+\sigma_y^2}{k_{tx}k_{cx}} + \frac{\sigma_z^2}{k_{tz}k_{cz}} - \frac{\sigma_y\sigma_z+\sigma_x\sigma_z}{k_{tz}k_{cz}} + \frac{3}{k_{tx}k_{cx}}\tau_{xy}^2 +$$
$$\frac{\tau_{yz}^2+\tau_{zx}^2}{k_{zx}^2} + \left(\frac{1}{k_{tx}} - \frac{1}{k_{cx}}\right)(\sigma_x+\sigma_y) + \left(\frac{1}{k_{tz}} - \frac{1}{k_{cz}}\right)\sigma_z = 1 \tag{10}$$

in which coefficients that precede terms $\sigma_x\sigma_y$ and τ_{xy}^2 are always positive. These prevent elliptic form of failure curves from degeneration and reduce Eq. (10) to the Huber-von Mises-Hencky ellipse "shifted" outside the origin of co-ordinate system in case of transverse isotropy plane. Since the Huber-von Mises-Hencky

criterion exhibits isotropy in hexagonal sense, therefore the Tsai-Wu failure criterion can also be classified as hexagonal in the plane of transverse isotropy. Consequently, condition (10) never violates the Drucker stability postulate, which is not guaranteed by equation (5). However, the hexagonally isotropic Tsai-Wu failure criterion cannot be presented in explicitly deviatoric form (1) which means that the axis of appropriate limit surface in the principal stress space is not parallel to the hydrostatic axis.

5. RESULTS

Both the Tsai-Wu transversely isotropic initial failure criteria: tetragonal Eq. (5) and new hexagonal type Eq. (10) are compared for columnar ice in plane of transverse isotropy (σ_x, σ_y) in Fig. 2, in plane of orthotropy (σ_x, σ_z) in Fig. 3 and in plane of transverse isotropy (σ_x, τ_{xy}) in Fig. 4. The experimental data of columnar ice was established by Ralston (1997) in Tab. 1.

Tab. 1. Experimental data for columnar ice, after Ralson (1997)

Tensile strength		Compressive strength	
k_{tx}	1.01 MPa	k_{cx}	7.11 MPa
k_{tz}	1.21 MPa	k_{cz}	13.5 MPa

Cross sections of the limit surface are ellipses, that exhibit strong aspect ratio in case tetragonal symmetry, the centers of which are shifted outside the origin of co-ordinate system towards the quarter referring to compressive stresses. In case of cross section by plane of transverse isotropy (see Fig. 2) the symmetry axis has obviously inclination equal 45° to the axes of coordinate system, in other words it overlaps projection of hydrostatic axis at the transverse isotropy plane (σ_x, σ_y), contrary to the cross section by plane of orthotropy (see Fig. 3) the main semi-axis of ellipse is inclined by 71.1°.

Fig. 2. Comparison of transversely isotropic Tsai-Wu initial failure criteria of tetragonal and hexagonal types for columnar ice in case of plane of transverse isotropy (σ_x, σ_y)

It has to be emphasized that, in case of columnar ice, compressive strength along othotropy axis k_{cz} is over 10 times great-

er than tensile strength k_{tz}, whereas analogous ratio k_{cx}/k_{tx} is approximately equal to 7 in case of transverse isotropy plane. Moreover, ratio of semi-axes for Tsai-Wu tetragonal ellipse in (σ_x, σ_y) plane essentially exceeds analogous ratio for Huber-von Mises-Hencky like ellipse, contrary to the case of Tsai–Wu hexagonal ellipse.
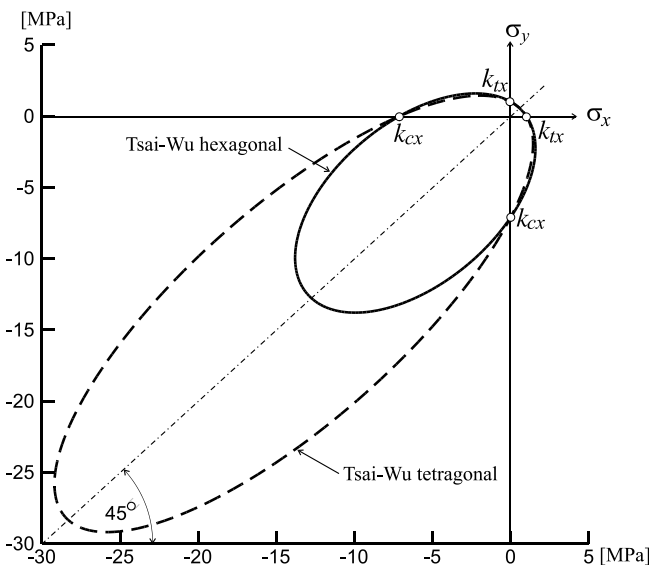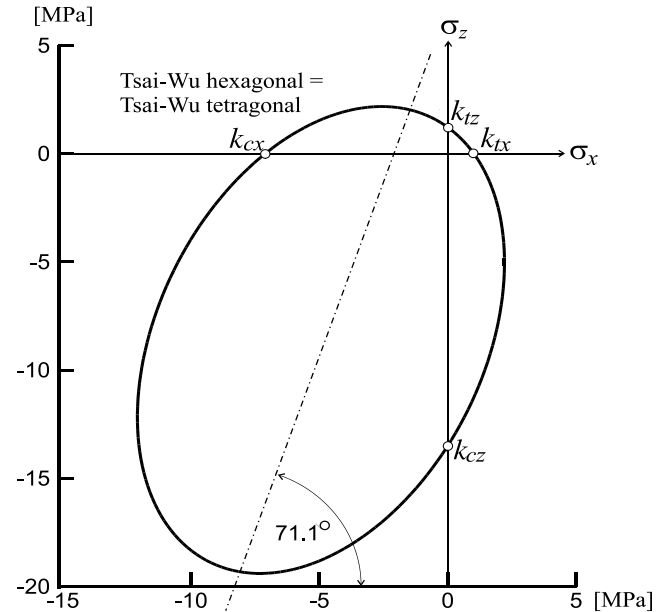

Fig. 3. Comparison of transversely isotropic Tsai-Wu initial failure criteria of tetragonal and hexagonal types for columnar ice in case of plane of orthotropy (σ_x, σ_z)

In case of cross sections of the limit surface in shear plane (σ_x, τ_{xy}) both ellipses referring to tetragonal and to hexagonal symmetry have comparable aspect ratio along tension-compression direction mainly resulting from aforementioned strength difference ratio k_{cx}/k_{tx} however the criterion (10) performs ellipse slightly broder than the criterion (5).
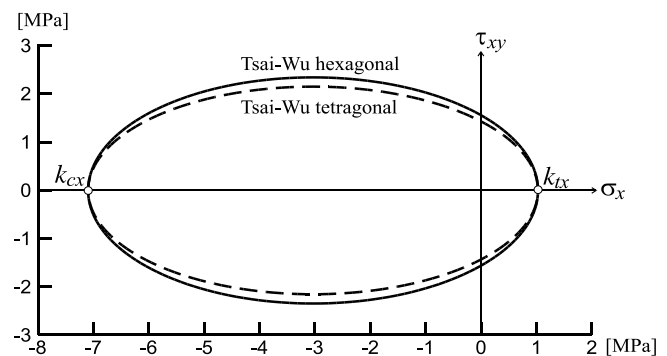
Fig. 4. Transverse isotropic Tsai-Wu initial failure criteria of tetragonal and hexagonal types for columnar ice in case of plane of transverse isotropy (σ_x, τ_{xy})

It is also worth to emphasize that although the tetragonal transversely isotropic Tsai-Wu failure criterion Eq. (5) and the hexagonal transversely isotropic Tsai-Wu failure criterion Eq. (10) contain the same number of 5 independent strengths k_{tx}, k_{cx}, k_{tz}, k_{cz} and k_{zx}, only criterion (10) is free from convexity loss and simultaneously truly transversely isotropic in sense of hexagonal class of symmetry.

6. CONCLUSIONS

Both transversely isotropic failure criteria: Tsai-Wu tetragonal and Tsai-Wu hexagonal perform paraboloidal surfaces in the space of principal stresses. However, the tetragonal criterion is represented by elliptic paraboloid which axis is parallel to the hydrostatic axis contrary to the hexagonal one, which represents elliptic paraboloid which axis is not parallel to the hydrostatic axis. Hence, hexagonal Tsai-Wu failure criterion does not satisfy deviatoric property; this is a consequence of its coincidence with Huber-von Mises-Hencky like criterion in the plane of transverse isotropy as well as a property of saving elliptical nature despite of high ratio of orthotropy. Choice of appropriate transversely yield criterion either tetragonal or hexagonal depends on coincidence with experimental tests done on real materials, that can be subjected to one or other class of symmetry, but also can exhibit properties different than aforementioned cases. Key point for proper classification of real transversely isotropic material to one of symmetry class (tetragonal, hexagonal) is the shape of limit curve belonging to the plane of transverse isotropy.

REFERENCES

1. **Cazacu O., Barlat F.** (2004), A criterion for description of anisotropy and yield differential effects in pressure-insensitive materials, *International Journal of Plasticity*, 20, 2027-2045.
2. **Chen W.F., Han D.J.** (1995), *Plasticity for Structural Engineeres*, Springer Verlag, Berlin-Heidelberg.
3. **Ganczarski A., Skrzypek J. (2013)**, *Mechanics of novel materials*, Wydawnictwo Politechniki Krakowskiej (in Polish).
4. **Ganczarski A., Skrzypek J.** (2014), Constraints on the applicability range of Hill's criterion: strong orthotropy or transverse isotropy, *Acta Mechanica*, 225, 2563−2582.
5. **Goldenblat I. I. Kopnov, V. A.** (1966): A generalized theory of plastic flow of anisotropic metals, *Stroitielnaya Mekhanika*, 307-319, (in Russian).
6. **Hill R.** (1948), A theory of the yielding and plastic flow of anisotropic metals, *Proceedings of Royal Society, London*, A193, 281−297.
7. **Hosford W. F., Backofen W. A.** (1964), Strength and plasticity of textured metals, in W. A. Backhofen, J. Burke, L. Coffin, N. Reed and V. Weisse (eds), *Fundamentals of deformation processing*, Syracuse University Press, 259-298.
8. **Khan A. S., Kazmi R., Farrokh B.** (2007), Multiaxial and non-proportional loading responses, anisotropy and modeling of Ti-6Al-4V titanium alloy over wide ranges of strain rates and temperatures, *International Journal of Plasticity*, 23, 931-950.
9. **Murakami S.** (2012), *Continuum Damage Mechanics,* Springer Verlag, Berlin.
10. **Ottosen N. S., Ristinmaa M.** (2005), *The mechanics of constitutive modeling*. Elsevier, Amsterdam.
11. **Ralson T.D.** (1997), Yield and plastic deformation of ice crushing failure*, ICSLAIDJEX Symposium on Sea Ice-Processes and Models,* Seattle, Washington.
12. **Sayir M.** (1970), On yield condition in theory of plasticity, *Ingenieurarchiv*, 39, 414-432 (in German).
13. **Tsai S. T., Wu E. M. (**1971), A general theory of strength for anisotropic materials, *Journal of Composite Materials*, 5, 58-80.

FUNCTIONAL AND STRUCTURAL ANALYSIS OF WING FOLDING MECHANISM
BASED ON COCKCHAFER (MELOLONTHA MELOLONTHA)

Tomasz GEISLER[*], **Piotr ROSIKOŃ**[*], **Wojciech SOCHACKI**[*], **Sandra TOPCZEWSKA**[*]

[*]Institute of Mechanics and Machine Design Foundations, Department of Mechanical Engineering and Computer Science,
Częstochowa University of Technology, J.H. Dąbrowskiego 73, 42-201 Częstochowa, Poland

t.geisler@imipkm.pcz.pl, p.rosikon@imipkm.pcz.pl, w.sochacki@imipkm.pcz.pl, s.topczewska@imipkm.pcz.pl

Abstract: Insects are among nature's most nimble flyers. In this paper we present the functional and structural analysis of wing joint mechanism. Detailed action of the axillary plates and their mutual interaction was also described. Because of the small dimensions of the wing joint elements and the limited resolution of the light microscope, the authors used a scanning electron microscope. Based upon the knowledge of working principles of beetle flight apparatus a wing joint mechanism kinematics model has been developed.

Key words: Bionic, Wing, Geometry, Joint, Folding

1. INTRODUCTION

Millions of years of evolution have enabled insects to develop substantial skill both in flight and active control of wing orientation. Long process of formation and profiling functions of individual biological components and their optimization is comparable to multigenerational research, carried out in order to improve the existing mechanism. Interdisciplinary science that includes a structural and functional analysis of living organisms, either for the construction of technical equipment or in order to adapt them in technology, as well as for the research purposes, is bionics.

In recent years there has been an increase in the number of research and literature in the field of bionics, and in particular in number of studies related to the ability of active flight of insects. An example of research work, in which an attempt to tentative reconstruction of the evolutionary pathway to insect flight was made, is paper of Hasenfuss (2008). In the work of Hass and Beutel (2001) functional morphology of insect wings was described.

Attempts of creating wing membrane folding patterns have also been made. The model introduced by Haas and Wootton (1996), included flexagon consisted of four flat facets that converge at a common node. Frantsevich (2011) and Geisler (2012) developed this flexagon pattern idea. Frantsevich (2011) work, apart from analysis of wing cover rotation mechanism in Coleoptera insects, also includes a flexagon model of the Haas and Wootton's type, as well as helical model introduction. Geisler (2012) study presents an analysis of both structure and internal folding and flexing structure mechanism of beetle wings. Both wing structure folding and their reciprocal motions were defined. In addition, in the work of Geisler (2011) the wing structure and folding of selected families of beetles, indicating biological characteristics as well as wings, covers and insect weight correlation, was described.

Intensification of work on creating a mechanically reproduced wing of various insects is also apparent. Efforts to follow the bending movement and the construction of an artificial beetle wing were shown in the work of Muhammad et al. (2009 and 2010).

In Bhayu et al. (2010) and Nguyen et al. (2010) publications not only the design of the wing, but also a flying model that mimics the movement of the wings of an insect were presented.

Undoubtedly, the dominant feature of the wing is to allow flight, but some insects evolved also ability to fold and bend some parts of the wings. All these movements are carried out by using wing joint.

Although there is a broad spectrum of work and intensive research in the field of insect flight apparatus, but so far very little was done in regard to the terms of mechanical and kinematic analysis of an important mechanism, which is a combination of wing joint and body of an insect.

The structural composition and functional scope of the individual components of the wing joint are very complex. The aim of this study is to geometrically analyse the properties of wing and body joint, and to create structural model simulating simplified mobility of this connection.

2. GENERAL STRUCTURE AND FUNCTIONS OF FLYING BEETLE WINGS

One of the main features specific to insects, representing the most numerous animal taxa, are wings - diverse in their structure and shape. These structures are a highly specialized flight apparatus, which are tailored to meet the individual demands of different families of insects.

The fully developed wing (Fig. 1) is made of double-layered membrane supported by an exoskeleton constructed of rigid structures and veins. Winged insects *(Pterygota)* usually have two pairs of wings located on middle *(mesothorax)* and the most posterior *(metathorax)* thoratic segment. In the examined beetle families the front pair of wings was transformed into hard covers (elytra). Heavily chitinized covers provide protection for the thorax and second pair of wings. Natural long-chained polymer in the form of chitin is the main component of the exoskeletons of arthropods, which, thanks to strong intermolecular hydrogen bonding, gives increased mechanical strength.

An unquestionable consequence of this evolutionary transformation is a significant increase of flight surface of the hind wings relative to the covers. Moving the locomotor functions to the hind wings, observed by Szwanwicz (1956), is related to this increase. Since the front wings are chitinised and the hind wings flight surface is increased, beetles at rest place their hind wings on dorsal sclerite of a thoracic segment (*notum*), protecting them under the hard elytra. But in order to do this, they must not only bend the second pair of wings, but also fold it due to its significant surface increase relative to the front pair.

Using the wing joint apparatus and bending joint, beetles can spread the wings out, fold and flap.

3. ANATOMICAL AND FUNCTIONAL ANALYSIS OF WING JOINT

The combination of wing to thorax joint is one of the most mechanically complex systems in the body of an insect. According Szwanwicz (1956), one of its primary functions is to allow flapping while simultaneously keeping this motion within strict boundaries. However, the same mechanism also determines the ability of the folding and spreading wings out, which have been developed by some insects.
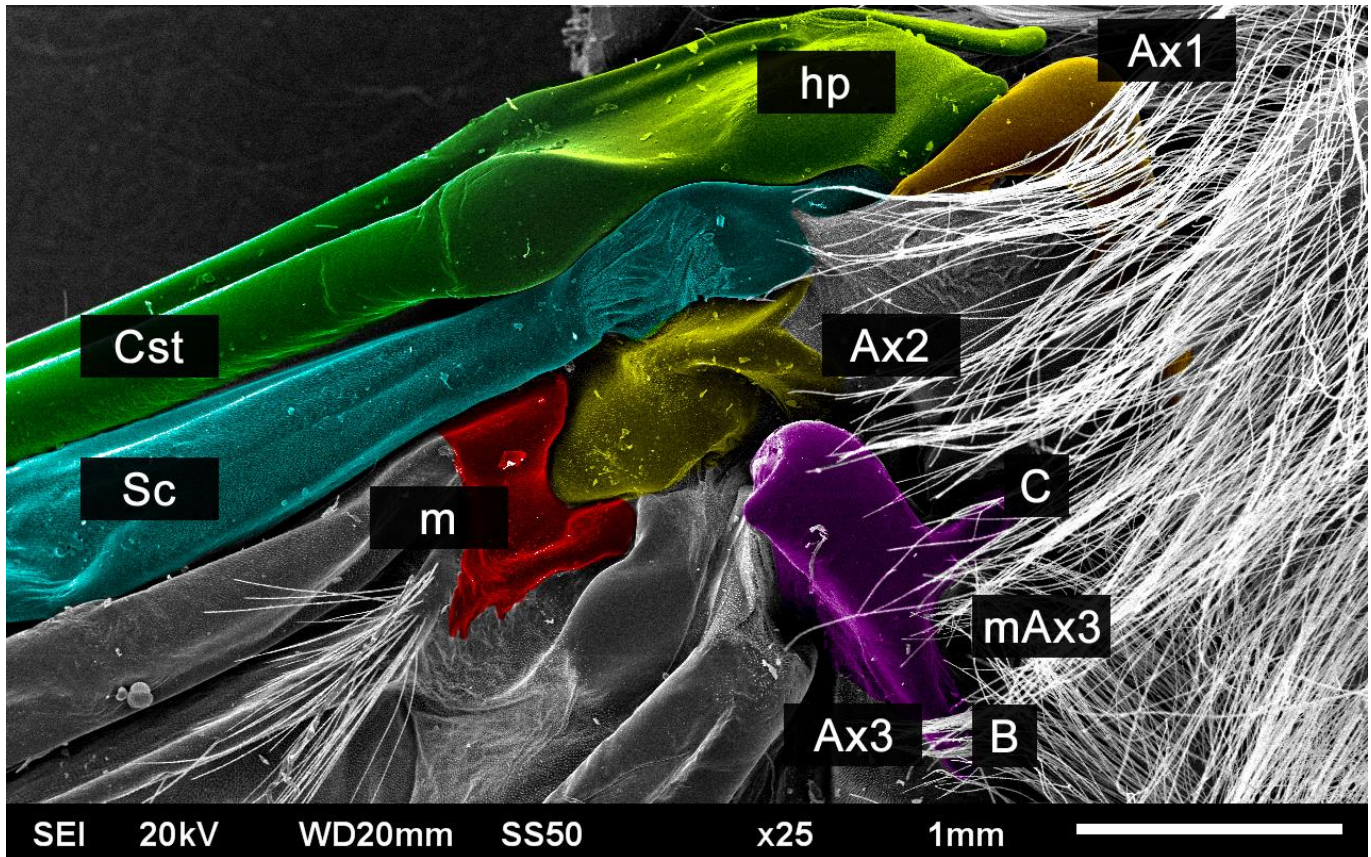

Fig. 1. Beetle wing: Melolontha Melolontha (L.) with separated structural components (individual elements are highlighted). Image was taken with scanning electron microscope

The structural composition and thus the features of axillary apparatus (wing joint) are diversified among the winged insects. This diversity has its basis in a form of adaptation to the prevailing conditions of life, obtaining food or colonizing new areas, typical only for the family of insects. In addition, insects have different mechanisms of changing the size of the wings surface, including different ways of wing folding. Further an anatomical analysis of wing joint on the example of selected species of insect – cockchafer, *Melolontha Melolontha* (L.1758), order: Beetles (*Coloptera*) family: Scarab Beetles (*Scarabaeidae*), subfamily: *Melolonthinae*, genus: *Melolontha* was performed.

From a morphological point of view, wing joint is composed by sclerites in the form of small joint plates, located between the thorax and the veins of insect wings. Sclerite is a hardened body part of an animal. It was formed, originally or secondarily, by separating from the outer product of invertebrate epithelium.

It is important that the location of the wing joint lies on the line between the bases of veins and thorax, so that the bases of veins do not reach the insect. Spatial layout of this system is equally important. Wing joint is not a construction build out of closely adjacent elements, but ending at a distance from each other, surrounded by a wing membrane. This very important aspect was described in the work of Szwanwicz (1956).

This allows insects to dispose a great freedom of wing movement, while maintaining the possibility of creating a stable configurations of the internal structures of selected wing functions, i.e. folding, flapping and spreading the wings out. Forming a relatively stable systems allow wings to choose the correct trajectory for selected type of movement, even though the main driving force are the indirect flight muscles according to the conclusions drawn by Dudley (1999) and Szwanwicz (1956).

4. WING STRUCTURE SEPARATION

Because of the small dimensions of the wing joint elements and the limited resolution of the light microscope (4x to 25x), proper structure isolation would be relatively difficult to obtain. Therefore the authors used a scanning electron microscope (JOEL JSM-6610LV), which enables one to record video with a magnification up to 300 000x (with practical application to 100 000x). Biological specimens, such as tissues or tissue components, must first be fixed to preserve their native structure. Hydrated samples, like most biological specimens, must first be dehydrated before placing it in the SEM sample chamber. The wings had therefore been divided into small specimens and prepared for the requirements of the vacuum-imaging environment.

During the analysis a number of internal wing structures were distinguished. For the further analysis three structures S1, S2 and S3 were adopted. The structures division was made on the basis of functional criteria.

4.1. S1 structure

The *Ax1+hp+Cst+Sc* system creates a structure marked as S1 (Fig. 1). Symbols were adopted in accordance with the indications given by Razowski (1987, 1996) and Wotton (1979). If the insect body flexibility is excluded, the *Ax1* sclerite remains firmly attached to the base formed out of the wing segment of insect thorax. One of *Ax1* sides is positioned at the dorsal plate segment of the insect body (*tergum*) and the second, while the wing is unfolded, is combined with *Sc* vein and *hp* sclerite. The *Ax1* sclerite is not situated perpendicular to the longitude axis of the insect body, but it remains tilted at an angle towards the *hp* sclerite. In a location closest to the *hp* sclerite and the *Sc* vein, *Ax1* has a double recess. The *Sc+Cs*t veins are a part of the leading edge of the wing. The *Cst* vein starts next to sclerite described as *hp*, while *Sc* starts with a process coming out of a vein base narrowing.

The S1 structure is used as wing blocking mechanism when it reaches the maximum angle of the leading edge in the outward movement of the wing with respect to the body. During the outward movement, the wing leading edge (*Cst+Sc*) rotates around its axis while simultaneously rotating around a point marked as A (Fig. 1). The maximum deflection of the leading edge in the wing plane is determined by inserting an *Sc* vein process into the *Ax1* sclerite recess. This system is additionally supported by the *hp* sclerite surface, which is in linear contact with the *Ax1* sclerite.

4.2. S2 structure

Another separated structure is composed out of Ax3 sclerite and mAx3 muscle. The Ax3 sclerite is shaped similar to triangle, which in the rest position of the wing takes position similar to perpendicular to the longest axis of the insect body. The mAx3 muscle is attached to this sclerite, making it the unique combination of muscle and sclerite in wing and thorax joint.

During the microscopic observation of the folding and spreading out the wings, the axis of *Ax3* sclerite rotation was determined. Rotation axis was described by defining its end points as B and C (Fig. 1). In the unfolded wing position, *mAX3* muscle remained contracted, while *Ax3* sclerite remains close to the veins base, which shows its triangular shape. The process of wing folding is related to *mAx3* muscle length changes, which causes approximation of the edge opposite to the rotation axis (starting from the common vertex B) to the insect's body. Folding and spreading out the wings is also related with tension and relaxation of subalar and basalar muscles.

Rotary movement of *Ax3* sclerite, using attached mAx3 muscle of S2 structure is the mechanism responsible for the folding and spreading out the wings. With the approximation of one of the sclerite edges to the body, veins, the bases of which converge around the axillary apparatus, are also approximated. Thus the wing begins folding process, starting from the jugal area (Ju) that is located nearest to the insects' abdomen.

4.3. S3 structure

Separated S3 structure was analysed based on spread wings prepared to fly. The S3 structure is composed of the elements of the S1 structure (*Ax1+C+Sc+hp*), which were complemented by m and *Ax2* sclerites. The S1 structure, as was written before, allows blocking the wing at maximum deflection angle of the leading edge, while spatially extended *Ax2+m* sclerites allow bending of blocked wing.

Having the elements in a specific location and with specific functionality, a structure that allows the wing flapping simultaneously stiffening wing joint, while preserving the limited spatial trajectory of the wings, was obtained. There is a possibility of forcing an additional bending the wing structure; nevertheless it results from the shape and elastic properties of the material of S3 structure components, therefore the system can be considered as rigid.

5. GEOMETRICAL WING ANALYSIS

In order to provide an analytical presentation of insect's wing geometry movement, a Cartesian coordinate system was introduced. Using three mutually perpendicular planes, allowed marking the location of defined points in three-dimensional space.

The origin of the body-fixed Cartesian reference is set at a point located between two preaxillary sclerites: humeral plate (*humeralis*) at the base of the *Cst* vein and tegula (*tegulae*) anterior to the base of *Cs*t vein and the highest point of *Ax1* element (Fig. 2). Axes were defined as x, y, z.

The x-axis is shifted by the line segment *c* - parallel to auxiliary line *b*, which is the axis of symmetry of the insects longitudinal thorax segment. Both the *xy*-axes and the auxiliary line lie on a horizontal plane α. This plane divides insect at an altitude of the vertical axis so that it runs through the origin of the system while maintaining perpendicularity with reference to this axis. Insect's location, relative to the reference system, is longitudinal in reference to x-axis and in accordance with its direction.

The *a* line was determined from the end of the wing leading edge to the origin of the coordinate system, providing thus a simplified variant of the analyzed edge. Two position of this line were also defined: a_{min} and a_{max} representing the resting position of the wings leading edge and its maximum spread, respectively.

The ω angle indicates the line *a* resting position deviation in respect to the x-axis, while ψ angle indicates its maximum deflection in respect to the a_{min}. The method of line *a* movement

is carried out in an arc motion, taking place in two dimensions with the centre of rotation located in the origin of coordinate system. The *a* line displacement, in the range of a_{min} to a_{max}, is accompanied by a local rotation with respect to its own axis. The rotation angle was labelled as φ. As mentioned, trajectory of points belonging to the moving *a* line is not perpendicular to the x-axis.

Though it can be visualized as arc shaped points' movement, whose path is partly negative along the z-axis and thus moving below the *a* plane α. The angle of maximum reduction in the *a* line was labelled as τ.
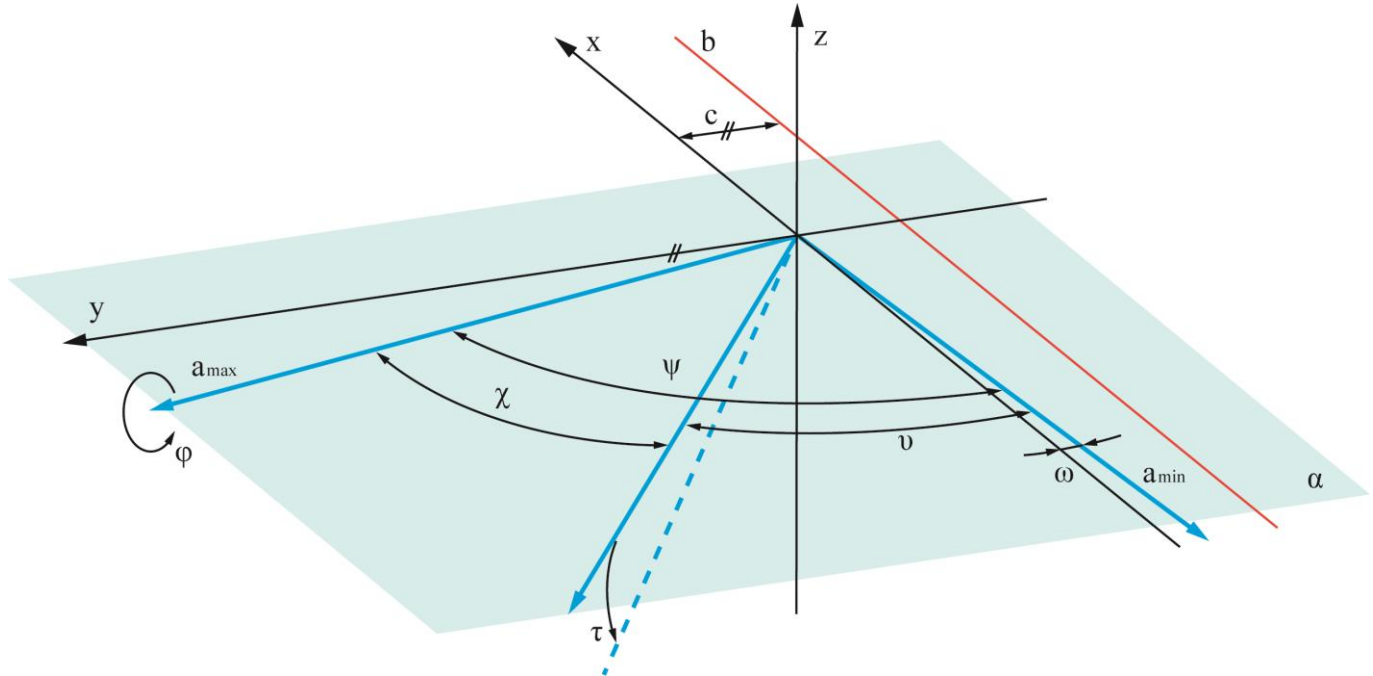

Fig. 2. Cockchafer's wing geometry. Coordinate system was adopted for the left side of insect body

6. RESULTS: KINEMATIC MODEL OF WING FOLDING

The complex wing joint mechanics arise from the high number of components, therefore the authors have defined its functionality using three structures: S1, S2 and S3.

According to Felis et al. (2008), Miller (1996) and Morecki et al. (2002) elementary and rigid components with undivided functionality and with the ability to perform relative movement are referred to as bodies. Therefore one can relate to the S1, S2 and S3 components as bodies.

The detailed action of the axillary plates and their mutual interaction to produce circular wing motion is difficult to describe. Thus, several underlying assumptions must be specified.

Motion may thus be either relative (performed by the axillary plates) or it may be absolute (performed by the separated structures S1, S2 and S3). In what follows, the thorax will be assumed to be at rest and all the motions referred to it will be considered as absolute. In Figs. 3, 4 and 5 the wing is placed along the abdomen (resting wing position), while in Fig. 1 the wing is laterally outspread. Each of these pictures was taken from the same position.

6.1. Structure movement analysis

It was noticed that in order to complete both the outward and the inward wing movement, the local rotation of *Cst + Sc* bodies is performed. This assumption is supported by the visibility changes of these components. One may observe that the *Cst +*

Sc components are highly visible in Fig. 1, whereas they are partially hidden in Fig. 3. In regard to the above and to the fact that both of the images were taken from the same position, one must conclude that local rotation is essential in order to unfold the wing.

The wing opening causes surface contact between the *Ax1* and *hp* bodies. This action "locks" the insect wing, allowing reaching no more than the maximum deflection angle (ψ in Fig. 2) of the wing leading edge (*a* in Fig. 2). This reflects the anatomical limits to the wing motion.

Simultaneously, the furthest segment of the *hp* (in the form of protuberance apex) is inserted into the socket aperture of *Ax1*. It is accomplished through a slide movement. It was noted that the sliding movement character also allows local rotation of the *Cst + Sc* bodies.

Taking into account the indirect participation of other structures bodies, *S1* structure action may be described as "locking wedge mechanism". It should be noted that the resilient part of this mechanism allowing pulling the hp apex out of the socket, is implemented directly in the member *mAX3*. Given the nonadjacent spatial distribution of the wing joint and its embedding in the membrane of the wing, it was noticed that other structure members have an indirect role in the transmission of the *mAx3* contraction and relaxation.

A characteristic feature of wedge mechanism is the lack of motor connections, whereas its elements are connected solely by means of sliding pairs. Therefore it was assumed that a flexible kinematic pair is present in the S1 structure, allowing the wedge part to enter and exit the socket part of the mechanism.
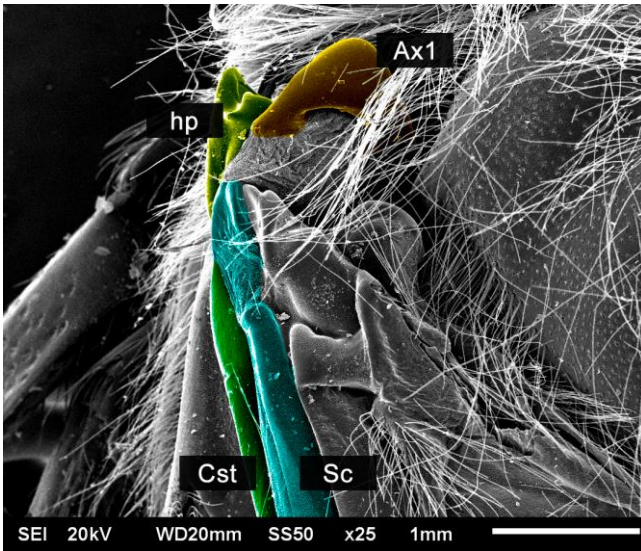
Fig. 3. First structure bodies

The *Ax3* plate rotation is reflected by the S2 elements motions, starting from its triangular position hidden under the thorax (Fig. 4) to a full spread, when its shape resembles a pyramid (Fig. 1). Two points: *B* and *C* (Figs. 1 and 4) define the rotation axis. Rotation is possible due to the adjacent muscle *mAx3* (Figs. 1 and 4) release. Muscle contraction causes the wing folding and hence hiding a part of *Ax3*.

The S2 structure, as a mechanism responsible for the wings folding and unfolding, is a ball joint type mechanism. The S2 structure is also a rotational III-class kinematic pair (lower) and allows the body rotations in the three axes: ψ – wingspread, τ – wing lowering during the folding and unfolding, φ – local wing rotation (Fig. 2). In addition, *mAx2* is a resilient member of the locking wedge mechanism of the S1 structure.
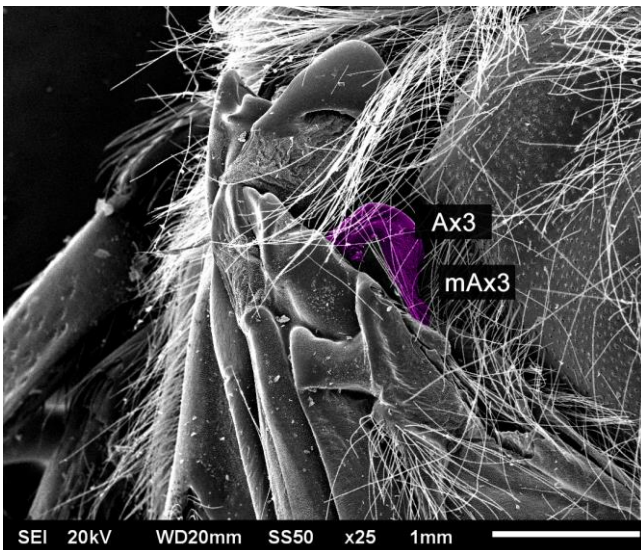

Fig. 4. Second structure bodies

The last of the separated structures marked as S3, is a combination of all S1 structure members and additional two elements: *m* and *Ax2*. The m member, apart of one fixed point, is being significantly shifted during the wing opening movement. Also the *Ax2* body is being slightly shifted and somewhat raised.

This allows for the adjustment of both members. "Locking" to the maximum angle of attack and the emplacement of *hp* apex in *Ax1* socket in association with the *m* and *Ax2* movement, stiffens the wing structure so that it could be temporarily treated as a solid plane.

The S3 structure, using the restriction imposed by S1 (ψ – the maximum angle of attack according to the notation of Fig. 2) and taking away the next two degrees of freedom, creates a joint with one degree of freedom of the characteristics of the hinge. This action is particularly important because it allows the wing to work as a single rigid structure, enabling it to perform flapping.
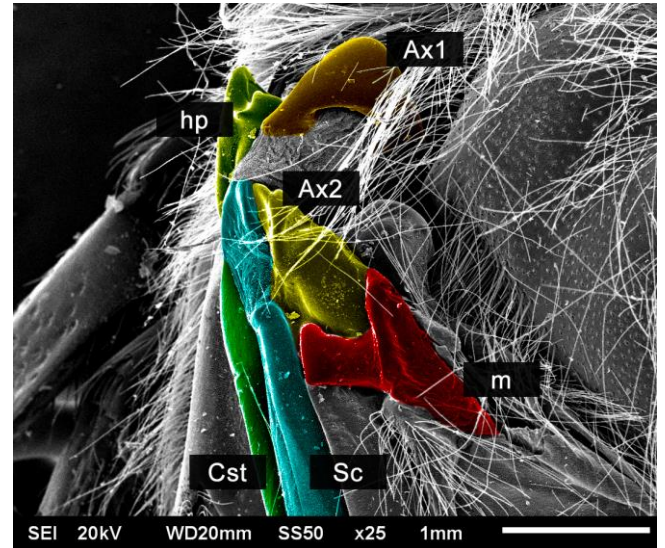
Fig. 5. Third structure bodies

6.2. The flexagon model

The idea of using flexagons as basic figures in the attempt of non-biological imitations of kinematic structures as a flight apparatus is not new.

In geometry, flexagons are complex three-dimensional models, characterized by polygonal surfaces called facets, which are mutually oblique planes. This structure is composed of a material folded in such way that the individual facets reveal themselves only when the structure is bent along the folds. It is possible to create different relative positions of the facets in a flexagon. Flexagonal structures are the basis for models described in the work of Frantsevich (2011) and Geisler (2012).

Based on the geometric, structural and kinematic wing joint analysis, the flexagon model (Fig. 6) was proposed as a solution for the flight apparatus movement implementation of the selected insect. It could be assumed that this model could be also applied for other beetle families that fold wings.

The facets (or a combination of facets) derive from the components of the S1, S2 and S3 structures. They are to be mechanical equivalents of the biological structures. It is therefore assumed that:

- Facet BCD is stationary;
- Facet BDE is the equivalent of the Ax3 plate, wherein the BD section is a rotation axis corresponding to the BC section of Fig. 1;
- Facets ABW+AHW are the equivalents of the *Ax2* plate;

− Facets EFW+FGW+GHW re the equivalents of the *m* plate;
− Broken lines indicate downward edges.

It was assumed that the points A and B are rigidly mounted to the leading edge of the wing, while the leading edge is parallel to the straight line between these points.

One of the main movements performed by the wing is unfolding. Given the fact that the direct force only acts on a rotating facet BDE, it is necessary to transfer this power to the leading edge through intermediary facets. Rest position of the BDE facet is associated with the right angle (δ in Fig. 6) relative to the BCD facet. The unfolding is related with an increase of this angle. The springiness of the material enables returning to the starting position without "passing through" the dead centre position.

Due to the movement of the BDE facet, the change of BEG and ABG facets is forced. BEG facet changes its initial angle (90°) relative to the ABG facet striving to achieve an obtuse angle. However ABG facet rotates in such a way that the BG segment is directed towards the BD segment.

The primary function of wings is to allow translocation by flight, pursued by the flapping. This movement was mechanically described as a hinge movement. The BDE facet of the proposed model (Fig. 6, point c) creates a fixed base, so that it becomes a pair of hinge.

tion is the spatialization of model planes segments, implemented by lowering GHW and FGW facets. The W point that is the common vertex of facetes restricted by ABEG points is being raised. The ABW, AHW and BEW converge externally in the vertex W. The common edge GW of facets FGW and GHW is directed downwards thereby prevents free mutual "breaking" of the structures. The wing must remain forced open.

The structures spatialization should meet the requirements of angles and lengths of the individual structures edges compatibility. Moreover, in the case of non-parallel structures the internal angle of collapsible structures will be determined by specifying the angle range.

It is possible to change the vertex position and to adapt new facets proportions or to increase their number. The proposed system provides a basis for further analysis and better representations of the wing components composition.

6.3. The scheme of flexagonal model

During the wing joint kinematics research, the anatomical and functional analysis as well as the wing structures separation were performed. The wing geometry was also described. The simplified motion model was based on the flexagonal model, which could be reduced to the planar mechanism with a kinematic pair of first class.

The kinematics model (Fig. 7) includes the wing movement in the range from rest to operating position.
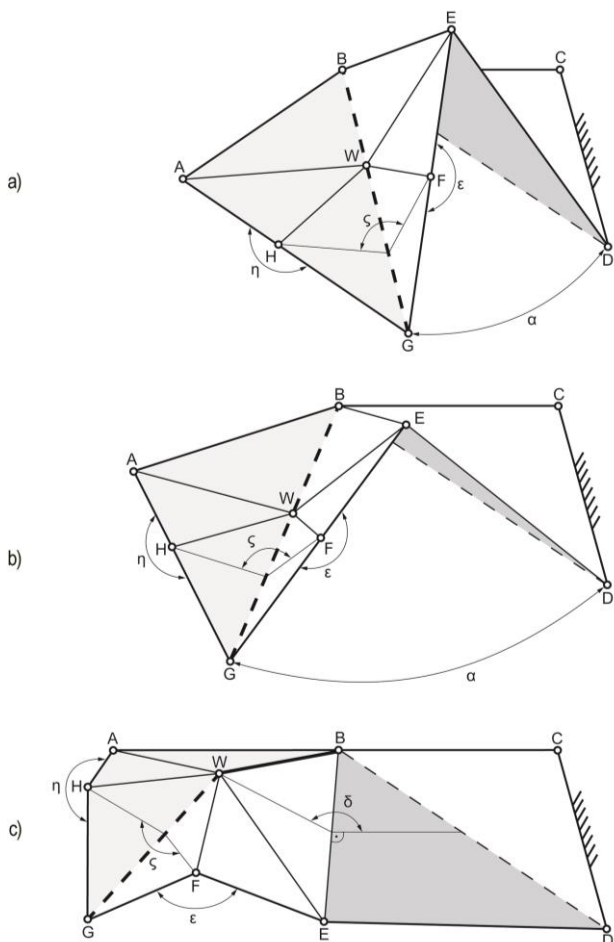
Fig. 6. Geometry and unfolding of proposed flexagon model

Fig. 7. Model of the kinematics

It became necessary to introduce such stiffen of the structures restricted by ABEG points, that could prevent structure folding while the movements of the hinge pair (wing flapping). The solu-

The kinematic chain consists of three moving bodies and one fixed body (three kinematic pairs of I-class). The auxiliary angle ρ takes the value between 0° – 80° (90°). In the particular case the μ angle is constant and amounts to 45°. The λ angle takes the value in the range of 0° – 170°(180°), while the θ angle is between 90° – 170° (180°). The E point position is the vector sum of L_2, L_3 and L_4 in the adopted coordinate system.

The number of freedom degrees is given by the planar chain mobility formula:

$$W = 3(n_c - 1) - \sum_{i=1}^{2}(3 - i)p_i \qquad (1)$$

where: n_c – total number of joints, p_i – kinematics pairs.

The given number of freedom degrees equals 3 in accordance with the actual system. The facet shape imposes the position

of the axis of rotation between the separated bodies of the kinematic chain.

7. CONCLUSIONS

Biomimetic engineering is an effective design approach, therefore future research may be oriented to creating a mechanical models based on extensive kinematic. Flapping wing mechanisms may be implemented in the micro air vehicles (MAV's).

Flight behaviour of insects is closely connected with their mechanical properties. This study provides geometric and functional basis of the insect's wing joint.

In order to carry out this analysis, the authors used not only the light microscope but also an scanning electron microscope. On the basis of the microscopic observation, a number of key wing structures were isolated and described in mechanical terms. Studies on the kinematic pairs in the wing mechanisms were also carried out.

The authors made an attempt at applying the results of geometric and functional analysis to a flexagonal model that would mimic the flight apparatus motions of Melolontha Melolontha. The created model is designed based on the working principles of the axillary plates mutual movement and meets the anatomical limits of the beetle's wing motion.

REFERENCES

1. **Bhayu P.R., Nguyen Q.V., Park H.C., Goo N.S, Byun D.** (2010), Artificial Cambered-Wing for a Beetle-Mimicking Flapper, *Journal of Bionic Engineering*, Vol. 7, 130–136.
2. **Dudley R.** (1999), *The Biomechanics of Insect Flight: Form, Function, Evolution*, Princeston University Press, New Jersey.
3. **Felis J., Jaworowski H., Cieślik J.** (2008), *Analiza Mechanizmów*, t.1, Wyd. 2, Wydawnictwa AGH, Kraków.
4. **Frantsevich L.** (2011), *Mechanisms Modeling the Double Rotation of the Elytra in Beetles (Coleoptera)*, Journal of Bionic Engineering, Vol. 8, 395–405.
5. **Geisler T.** (2011), Beetle wing construction and folding of selected families (Coleoptera), Biuletyn Częstochowskiego Koła Entomologicznego, Nr 10 11/2011, 12-21, (in Polish).
6. **Geisler T.** (2012), *Analysis of the structure and mechanism of wing folding and flexion in Xylotrupes Gideon beetle (L.1267 Coleoptera, Scarabaeidae)*, Acta mechanica et automatica, Vol. 6, 37-44.
7. **Gronowicz A., Miller S., Twaróg W.** (2000), Theory of machines and mechanisms. A set of analysis and design problems, Oficyna Wydawnicza Politechniki Wrocławskiej, Wrocław, (in Polish).
8. **Haas F, Wootton R. J.** (1996), *Two basic mechanism in insect wing folding*, Proceedings of the Royal Society B: Biological Sciences, Vol. 263, 1651–1558.
9. **Haas F., Beutel R.G** (2001), *Wing folding and the functional morphology of the wing base in Coleoptera*, Zoology, Vol. 104, 123 – 141.
10. **Hasenfuss I**. (2008), *The evolutionary pathway to flight - a Tentative Reconstruction, Arthropod Systematics & Phylogeny*, Vol. 66, 19-35.
11. **Miller S.** (1988), *Kinematic systems. Design basics*, Wydawnictwo Naukowo – Techniczne, Warszawa, (in Polish).
12. **Miller S**. (1996), *Theory of machines and mechanisms: analysis of physical systems*, Wyd. 2, Oficyna Wydawnicza Politechniki Wrocławskiej, Wrocław, (in Polish).
13. **Morecki A., Knapczyk J., Kędzior K.** (2002), *Theory of mechanisms and manipulators. Fundamentals and application examples in practice*, Wydawnictwa Naukowo – Techniczne, Warszawa, (in Polish).
14. **Muhammad A., Nguyen Q.V., Park H.C., Hwang D.Y., Byun D., Goo N.S.** (2010), *Improvement of Artificial Foldable Wing Models by Mimicking the Unfolding/Folding Mechanism of a Beetle Hind Wing*, Journal of Bionic Engineering, Vol. 7, 134-141.
15. **Muhammad A., Park H.C., Hwang D.Y., Byun D., Goo N.S.** (2009), *Mimicking unfolding motion of a beetle hind wing*, Chinese Science Bulletin, Vol. 54, 2416 – 2424.
16. **Nguyen Q.V., Park H.C., Goo N.S., Byun D.** (2010), *Characteristics of a Beetle's Free Flight and a Flapping-Wing System that Mimics Beetle Flight*, Journal of Bionic Engineering, Vol. 7, 77-86.
17. **Razowski J.** (1987), *Etymological dictionary*, PWN, Warszawa, (in Polish).
18. **Razowski J**. (1996), *Dictionary of insect morphology*, PWN, Warszawa – Kraków, (in Polish).
19. **Szwanwicz B.** (1956), *General entomology*, PWRiL, Warszawa, (in Polish).
20. **Wootton R. J.** (1979), *Function, homology and terminology in insects wing*s, Systematic Entomology, Vol. 4, 81-93.

List of Acronyms: Ax1 – first axillary plate, Ax2 – second axillary plate, Ax3 – third axillary plate, Cst – costal vein, hp – humeral plate, m – median plates, mAx3 – third axillary plate muscle attachment, Sc – subcostal vein.

CONSTITUTIVE MODELLING AND IDENTIFICATION OF PARAMETERS OF 316L STAINLESS STEEL AT CRYOGENIC TEMPERATURES

Maciej RYŚ[*]

[*]Institute of Applied Mechanics, Faculty of Mechanical Engineering, Cracow University of Technology,
Al. Jana Pawła II 37, 31-864 Kraków, Poland

maciej_rys@o2.pl

Abstract: In this work, a macroscopic material model for simulation two distinct dissipative phenomena taking place in FCC metals and alloys at low temperatures: plasticity and phase transformation, is presented. Plastic yielding is the main phenomenon occurring when the yield stress is reached, resulting in nonlinear response of the material during loading. The phase transformation process leads to creation of two-phase continuum, where the parent phase coexists with the inclusions of secondary phase. An identification of the model parameters, based on uniaxial tension test at very low temperature, is also proposed.

Key word: Constitutive Modelling; Dissipative Materials; Phase Transformation; Cryogenic Temperature

1. INTRODUCTION

The present paper is focused on the constitutive description and identification of the parameters of the model of austenitic stainless steel 316L for cryogenic applications. Two coupled dissipative phenomena, plastic flow and phase transformation, are considered using a thermodynamically consistent framework. The theory relies on the notion of local state, and involves one state potential for the state laws, and a dissipation potential for the description of the irreversible phenomena regarded in the model. Parameters of the presented model can be easily identified and the model can be implemented into commercial FEM programs like ABAQUS or ANSYS.

The model presented in this paper describes phase transformation that occurs in metastable stainless steels at very low temperatures. Other phenomena, like discontinuous yielding and damage evolution, are not taken into account here (Egner et al., 2014; Egner, 2013; Egner and Skoczeń, 2010). The FCC (face-centered cubic) to BCC (body-centered cubic) phase transformation has an important meaning in constitutive modelling, because of the influence of the martensitic fraction on hardening process during the plastic deformation. The kinetic laws for state variables are driven from normality rule applied to the plastic potential, while the consistency multiplier is obtained from the consistency condition applied to the yield function (Chaboche, 2008). The classical laws of kinematic and isotropic hardening are postulated in the present work. However, the volume fraction of martensite affects the parameters of both kinematic and isotropic hardening.

The physically based transformation kinetics has been developed by Olson and Cohen (1975). The authors have postulated a three parameter model capable of describing the experimentally verified sigmoidal curve that represents the volume fraction of martensite as a function of plastic strain (Fig. 1):

$$\xi = 1 - \exp\{-\beta[1 - \exp(-\alpha\epsilon^p)]^\lambda\} \tag{1}$$

where: α denotes the rate of shear-band formation, β represents the probability that a shear-band intersection will become a martensite nucleation site, and λ is a fixed exponent. The sigmoidal curve is valid for a wide range of temperatures, including room temperature. However, at very low temperatures the rate of phase transformation for an LSFE (low stacking-fault energy) material becomes less temperature dependent, and can be described by a simplified, linearized model (Garion and Skoczeń, 2002):

$$\dot{\xi} = A\dot{p}H\left((p - p_\xi)(\xi_L - \xi)\right) \tag{2}$$

In the above equation A is the model parameter, p denotes accumulated plastic strain, p_ξ stands for the accumulated plastic strain threshold that triggers the formation of martensite, while ξ_L is a limit of martensite content, above which the martensitic transformation rate vanishes. Symbol H denotes the Heaviside step function. Relation (2) introduces a simplified evolution law for the martensite content, with respect to the linear part (region II) of the sigmoidal curve (Fig. 1).
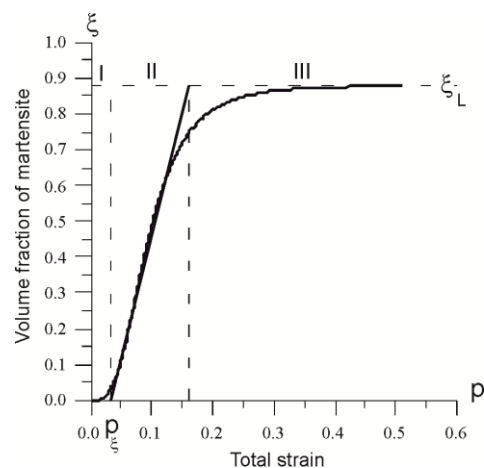
Fig. 1. Volume fraction of α' martensite versus accumulated plastic strain (Garion and Skoczeń, 2002)

2. CONSTITUTIVE DESCRIPTION OF THE ELASTIC-PLASTIC TWO PHASE MATERIAL

The author considers a material that is susceptible to two coupled dissipative phenomena: plasticity and phase transformation, that are formalized on the macroscopic level by the use of a proper set of state variables. The motions within the considered thermodynamic system obey the fundamental laws of continuum mechanics (conservation of mass, conservation of linear momentum, conservation of angular momentum) and two laws of thermodynamics, written here in the local form:

− conservation of energy

$$\rho\dot{u} - \dot{\epsilon}_{ij}\sigma_{ij} - r + q_{i,i} = 0 \tag{3}$$

− Clausius-Duhem inequality

$$\pi = -\rho(\dot{\psi} + s\dot{\theta}) + \dot{\epsilon}_{ij}\sigma_{ij} - q_i\frac{\theta_{,i}}{\theta} \geq 0 \tag{4}$$

where: π denotes the rate of dissipation per unit volume, ρ is the mass density per unit volume; σ_{ij} are the components of the stress tensor; u stands for the internal energy per unit mass; ϵ_{ij} denote the components of the total strain tensor; r is the distributed heat source per unit volume; q_i is the outward heat flux; s denotes the internal entropy production per unit mass, ψ stands for Helmholtz' free energy and θ is the absolute temperature.

The RVE based constitutive model presented in the paper is based on the following assumptions (Egner and Skoczeń, 2010):

1. the martensitic platelets are randomly distributed and randomly oriented in the austenitic matrix;
2. rate independent plasticity is assumed, because the influence of the strain rate is small for the considered range of temperatures (2-77 K) (cf. Hecker et al., 1982);
3. infinitesimal strain theory is applied;
4. mixed isotropic/kinematic plastic hardening affected by the presence of martensite fraction is included;
5. the two-phase material obeys the associated flow rule (volume fraction of new phase not exceeding 0.5);
6. isothermal conditions are considered (no fluctuations of temperature are taken into account).

Applying infinitesimal deformation theory to elastic – plastic – two phase material the total strain ϵ_{ij} can be expressed as a sum of the elastic part, ϵ_{ij}^e plastic, ϵ_{ij}^p and bain strain $\epsilon^{bs} = 1/3\Delta vI$, denotes the free deformation describing the transformation induced change of the volume, expressed in terms of the relative volume change Δv.

$$\epsilon_{ij} = \epsilon_{ij}^e + \epsilon_{ij}^p + \xi\epsilon_{ij}^{bs} \tag{5}$$

The presented model is based on the framework of thermodynamics of irreversible processes with internal state variables, where Helmholtz free energy ψ is postulated as a state potential. The state potential depends on the elastic part of the total strain, and set of internal state variables $N_k (k = 1,2 \dots)$, which define the current state of the material:

$$\psi = \psi(\epsilon_{ij}^e, N_k) \tag{6}$$

In the case of elastic-plastic material with phase transformation the current state of the material is described by the set of state variables presented in Tab. 1 (cf. Egner, 2012).

Tab. 1. State variables and corresponding thermodynamic forces

phenomenom	state variables	conjugated forces
mechanical variables: total strain, Cauchy stress	observable state variables ϵ_{ij}	σ_{ij}
plastic flow	internal variables ϵ_{ij}^e (or ϵ_{ij}^p)	σ_{ij} or $(-\sigma_{ij})$
kinematic plastic hardening	α_{ij}^p	X_{ij}^p
isotropic plastic hardening	r^p	R^p
phase transformation	ξ	Z

The Helmholtz free energy of the material can be written as a sum of elastic (*E*), inelastic (*I*) and chemical (*CH*) terms (Abu Al-Rub and Voyiadjis, 2003; Egner, 2013):

$$\psi = \rho\psi^E + \rho\psi^I + \rho\psi^{CH} \tag{7}$$

$$\rho\psi^E = \frac{1}{2}\epsilon_{ij}^e E_{ijkl}\epsilon_{kl}^e \tag{8}$$

$$\rho\psi^I = \frac{1}{3}C^p\alpha_{ij}^p\alpha_{ij}^p + R_\infty^p\left[r^p + \frac{1}{b^p}\exp(-b^p r^p)\right] \tag{9}$$

Term $\rho\psi^{CH}$ in Eq. (7) represents the chemically stored energy:

$$\rho\psi^{CH} = (1-n)\rho\psi_\gamma^{CH} + n\rho\psi_{\alpha'}^{CH} \tag{10}$$

where: n is a function of martensite content such that $n(0) = 0$ and $n(1) = 1$ and define general mixture rule. The terms $\rho\psi_\gamma^{CH}$ and $\rho\psi_{\alpha'}^{CH}$ are the chemical energies of the respective phases, cf. Hallberg et al. (2010), Mahnken and Schneidt (2010). This internally stored energy is different for the two phases and it will affect the generation of heat during phase transformation, as well as the transformation itself.

Using the Clausius-Duhem inequality for isothermal case, one obtains:

$$\pi^{mech} = \sigma_{ij}\dot{\epsilon}_{ij} - \rho\dot{\psi} \geq 0 \tag{11}$$

where: π^{mech} is defined as mechanical dissipation.

The time derivative of Helmholtz free energy (Eq. 6) as a function of internal state variables is given by:

$$\dot{\psi} = \frac{\partial\psi}{\partial\epsilon_{ij}^e}\dot{\epsilon}_{ij}^e + \frac{\partial\psi}{\partial\alpha_{ij}^p}\dot{\alpha}_{ij}^p + \frac{\partial\psi}{\partial r^p}\dot{r}^p + \frac{\partial\psi}{\partial\xi}\dot{\xi} \tag{12}$$

Substituting the rate of the Helmholtz free energy into Clausius-Duhem inequality the following thermodynamic constraint is obtained:

$$\left(\sigma_{ij} - \rho\frac{\partial\psi}{\partial\epsilon_{ij}^e}\right)\dot{\epsilon}_{ij}^e + \sigma_{ij}\dot{\epsilon}_{ij}^p - \rho\frac{\partial\psi}{\partial\alpha_{ij}^p}\dot{\alpha}_{ij}^p - \rho\frac{\partial\psi}{\partial r^p}\dot{r}^p -$$
$$\rho\frac{\partial\psi}{\partial\xi}\dot{\xi} \geq 0 \tag{13}$$

Eq. 13 results in the following thermodynamic state laws for the conjugate thermodynamic forces:

$$\sigma_{ij} = \rho\frac{\partial\psi}{\partial\epsilon_{ij}^e} = E_{ijkl}\epsilon_{kl}^e = E_{ijkl}(\epsilon_{kl} - \epsilon_{kl}^p - \xi\epsilon_{kl}^{bs}) \tag{14}$$

$$X_{ij}^p = \rho\frac{\partial\psi}{\partial\alpha_{ij}^p} = \frac{2}{3}C^p\alpha_{ij}^p \tag{15}$$

$$R^p = \rho \frac{\partial \psi}{\partial r^p} = R_\infty^p [1 - \exp(-b^p r^p)] \tag{16}$$

$$Z = \rho \frac{\partial \psi}{\partial \xi} = \rho \frac{\partial \psi^I}{\partial \xi} + \frac{dn}{d\xi}\left(\rho \psi_{\alpha'}^{CH} - \psi_\gamma^{CH}\right) \tag{17}$$

where: X_{ij}^p, R^p and Z are the thermodynamic forces conjugated to the state variables α_{ij}^p, r^p and ξ, respectively.

It is assumed here that all dissipative mechanisms are governed by plasticity with a single dissipation potential F (Lemaitre 1992):

$$F = F^p\left(\sigma_{ij}, X_{ij}^p, R^p, \xi\right) + F^{tr}(Q, \xi) \tag{18}$$

Plastic potential F^p is here equal to von Mises type yield surface:

$$F^p = f^p = J_2\left(\sigma_{ij} - X_{ij}^p\right) - \sigma_y - R^p \tag{19}$$

and the phase transformation dissipation potential is assumed here in a simple form:

$$F^{tr} = AQ - B^{tr} = 0 \tag{20}$$

The quantity $Q = \sigma_{ij}\epsilon_{ij}^{bs} - Z$ is conjugated to the transformation rate $\dot{\xi}$ and can be treated as a thermodynamic force that drives the phase front through the material (cf. Hallberg et al., 2007, 2010), $A\left(\theta, \sigma_{ij}, \dot{\epsilon}_{ij}^p\right)$, in general, is a function of temperature, stress state and strain rate, and B^{tr} is the barrier force for phase transformation (cf. Mahnken and Schneidt, 2010; Fisher et al., 2000). For rate independent plasticity, isothermal process and small stress variations function A may be treated as a constant value.

Normality rule involves only one plastic multiplier, determined from the consistency condition. The equations involving the dissipation potentials take the form:

$$\dot{\epsilon}_{ij}^p = \dot{\lambda}^p \frac{\partial F^p}{\partial \sigma_{ij}} = \dot{\lambda}^p \frac{\partial f^p(\sigma_{kl} X_{kl}^p, R^p)}{\partial \sigma_{ij}} \tag{21}$$

$$\dot{\alpha}_{ij}^p = -\dot{\lambda}^p \frac{\partial F^p}{\partial \sigma_{ij}} = \dot{\epsilon}_{ij}^p \tag{22}$$

$$\dot{r}^p = -\dot{\lambda}^p \frac{\partial F^p}{\partial R^p} = \dot{\lambda}^p \tag{23}$$

$$\dot{\xi} = \dot{\lambda}^p \frac{\partial F^{tr}}{\partial Q} = A\dot{p}H\left((p - p_\xi)(\xi_L - \xi)\right) \tag{24}$$

The consistency multiplier $\dot{\lambda}^p$ is obtained from the consistency condition:

$$\dot{f}^p = \frac{\partial f^p}{\partial \sigma_{ij}}\left(\dot{\sigma}_{ij} - \dot{X}_{ij}^p\right) + \frac{\partial f^p}{\partial R^p}\dot{R}^p + \frac{\partial f^p}{\partial \xi}\dot{\xi} = 0 \tag{25}$$

The evolution equations for thermodynamic conjugated forces are obtained by taking time derivatives of quantities defined by equations (14) – (16). In particular, the force rates appearing in consistency condition (25) are given by the following formulae:

$$\dot{\sigma}_{ij} = E_{ijkl}\left(\dot{\epsilon}_{kl} - \dot{\epsilon}_{kl}^p - \dot{\xi}\epsilon_{kl}^{bs}\right) \tag{26}$$

$$\dot{X}_{ij}^p = \frac{2}{3}C^p\dot{\epsilon}_{ij}^p + \frac{1}{C^p}\frac{\partial C^p}{\partial \xi}X_{ij}^p\dot{\xi} \tag{27}$$

$$\dot{R}^p = b^p\left(R_\infty^p - R^p\right)\dot{r}^p + \left[\frac{1}{R_\infty^p}\frac{\partial R_\infty^p}{\partial \xi}R^p + \left(R_\infty^p - R^p\right)r^p\frac{\partial b^p}{\partial \xi}\right]\dot{\xi} \tag{28}$$

It has to be mentioned here, that in comparison to previous works (Egner and Ryś 2013, Egner et al 2012) the extended evolution equations for thermodynamic conjugate forces (back stress X_{ij}^p and drag stress R^p) were derived, accounting for additional terms related to phase transformation rate (full coupling, cf Egner 2013).

3. IDENTIFICATION OF PARAMETERS OF THE CONSTITUTIVE MODEL

Identification of the material constants associated with any proposed material model is one of the most challenging issues for researchers, in order to obtain better representation of their material models. If limited test data are available, parameters can be based on the stress-strain data obtained from the uniaxial tension or compression experiments. In the present work a uniaxial tension test for 316L stainless steel at temperature 4.2K is used to determine functions $C^p(\xi)$, $b^p(\xi)$ and $R_\infty^p(\xi)$ occurring in the kinetic laws (Eq. (27) – (28)). The simplest, linear form of these functions is here assumed, namely:

$$C^p(\xi) = C_0^p(1 + h_C\xi), \tag{29}$$

$$R_\infty^p(\xi) = R_{\infty,0}^p(1 + h_R\xi) \tag{30}$$

$$b^p(\xi) = b_0^p(1 + h_b\xi) \tag{31}$$

Eventually the following parameters have to be determined in the present model: C_0^p, h_C, $R_{\infty,0}^p$, h_R, b_0^p, h_b. The value of the parameter A (24) is taken from the paper by Garion et al. (2006). The function which describes the experimental results of martensite content was found in the following form (Garion et al, 2006), (Fig. 2):

$$\xi = 4.3714p - 0.3873, \text{ for } p > p_\xi \tag{32}$$
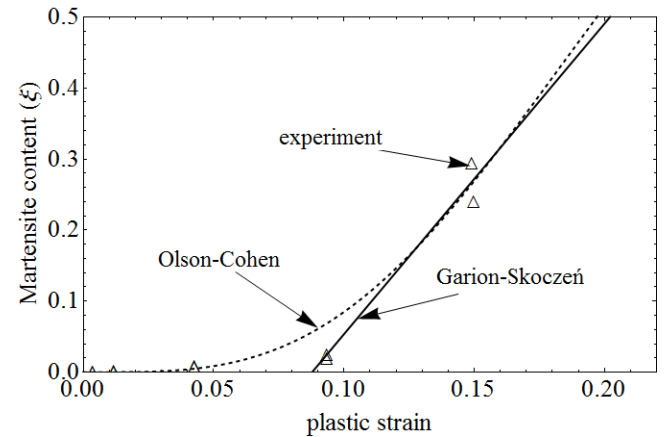
Fig. 2. Martensite content as a function of plastic strain

As was mentioned before, determining of all parameters occurring in kinetic equations is based on the experimental stress-strain curve obtained for 316L stainless steel at 4.2K. The test was performed with use of the cryostat filled up with liquid helium and equipped with tensometers, extensometers and a load cell aligned with the sample. It was concerned that the kinematically controlled tensile test is the most suitable. Moreover, the measurement of the volume fraction of martensite was based on ferro-magnetic properties of the BCC martensitic phase whereas the FCC austenitic matrix is paramagnetic. It has to be mentioned

here that the experiments carried out in liquid helium are expensive and laborious and this is the reason why the identification of the parameters is based only on uniaxial tension test. The stress strain curve was divided into three regions: elastic, plastic and plastic with phase transformation. Every point on the curve within plastic region can be described in the following way (Fig. 3. range II, see also Abu Al-Rub 2004, Lemaitre 1992):

$$\sigma = \sigma_y + X^p(\epsilon^p) + R^p(p) \tag{33}$$

where: σ_y is the yield stress and equations for kinematic, $X^p(\epsilon^p)$, and isotropic, $R^p(p)$, hardening in the case of uniaxial state of stress are exspressed as:

$$X = C_0^p \epsilon^p; R^p = b_0^p\left(R_{\infty,0}^p - R^p\right)p \tag{34}$$

Now the standard least-square minimization method was used to find the parameters C_0^p, $R_{\infty,0}^p$, b_0^p and fit the model to the data points.
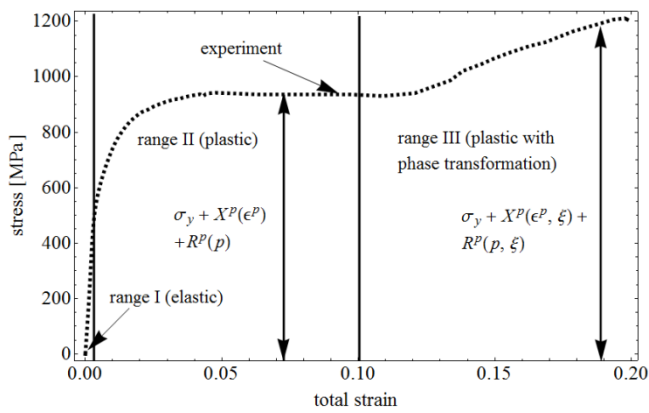

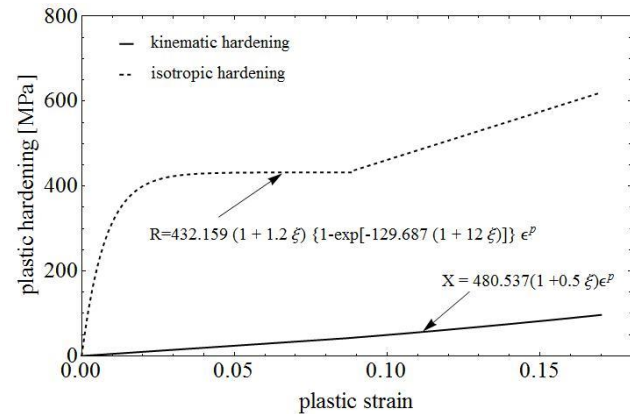**Fig. 3.** Stress-strain curve for 316L stainless steel at 4.2K

Fig. 4. Evolution of the plastic hardening forces

Every point within inelastic region can be described as follows (Fig. 3. Range II and III):

$$\sigma = \sigma_y + X^p(\xi, \epsilon^p) + R^p(\xi, p) \tag{35}$$

where:

$$X^p(\xi, \epsilon^p) = C_0^p(1 + h_C \xi)\epsilon^p \tag{36}$$

$$R^p(\xi, p) = b_0^p(1 + h_b \xi)\left(R_{\infty,0}^p(1 + h_R \xi) - R^p\right)p \tag{37}$$

where: p is equal to ϵ^p in the case of uniaxial tension and parameters: C_0^p, $R_{\infty,0}^p$, b_0^p are already known. Again, the standard least-square minimization method was used to find the rest of the unknown parameters. All values of the identified parameters are listed in Tab. 2. The curves plotted in Fig. 4 represent the synergetic effects of the combined isotropic and kinematic hardening associated with plasticity found for the present model.
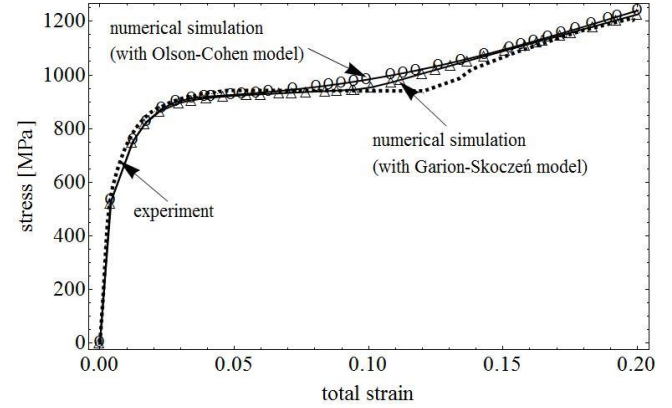
Fig. 5. Stress-strain curve for 316L stainless steel

Accounting for two dissipative phenomena: plasticity and phase transformation in the present constitutive model allows to obtain a satisfactory reproduction of the experimental stress-strain curve for 316L stainless steel subjected to uniaxial tension at cryogenic temperatures (see Fig. 5). A small difference between numerical and experimental results is caused by damage which is not included in the present model. Using Garion-Skoczeń linear kinetic law of phase transformation also exacerbates the numerical results. However, the model presented here is easy to identify experimentally because the number of material parameters is reasonably small. It should be pointed out that the experiments carried out in liquid helium or liquid nitrogen are laborious, expensive and usually require complex cryogenic installations to maintain stable conditions (constant or variable temperature). Therefore, any justified simplification leading to reduction of the number of parameters to be determined is of great importance.

Tab. 2 Material data for 316L stainless steel at the temperature of 4.2K

Young modulus [GPa]	176.818
Poisson ratio	0.3
Proportionality limit [MPa]	470
C_0^p [MPa]	480.537
$R_{\infty,0}^p$ [MPa]	432.159
b_0^p	129.687
h_C	0.5
h_R	1.2
h_b	12
Δv	0.02
p_ξ	0.0886
ξ_L	0.9
A	4.3714

5. CONCLUSIONS

The constitutive model presented in the paper includes two dissipative phenomena: plastic yielding and plastic strain induced phase transformation. A consistent thermodynamic framework was used in order to describe dissipative phenomena. Two kinetic laws of phase transformation were used: Olson-Cohen and Garion-Skoczeń model. As shown in Fig. 5 and Fig. 2, the use of simplified Garion-Skoczeń linear phase transformation law allows for a very good approximation of the second stage of Olson-Cohen sigmoidal curve (see Fig. 1) and a stress-strain curve. A great advantage of the presented model is a relatively small amount of parameters that can be determined in the simple way. A standard uniaxial tension test and least squares method were used to identify the model parameters. Validation of the model is based on the available experimental data and very rare experiments carried out at extremely low temperatures. Such tests are extremely laborious, complex, costly and time consuming and are not common even in the centers, where the low temperature research belongs to the standard activities (like CERN). For this reason, given the scarce experimental background, the model has been validated on one single test only. As the results, however, seem to be very encouraging, the author believes that the model performs correctly and can be further applied to a larger class of problems of low temperature material behaviour. As soon as some more experimental data is available, the validation of the model will certainly be confirmed.

REFERENCES

1. **Abu Al Rub R. K** (2004), M*aterial length scales in gradient-dependent plasticity/damage and size effects: theory and computation*, Ph.D. Thesis, , Lousiana State University, Louisiana, USA.

2. **Abu Al Rub R. K, Voyiadjis G.Z.** (2003), On the coupling of anisotropic damage and plasticity models for ductile materials, *International Journal of Plasticity*, 40, 2611-2643.

3. **Chaboche, J.** (2008), A review of some plasticity and viscoplasticity constitutive theories, *International Journal of Plasticity,* 24, 1642-1693.

4. **Egner H.** (2012), On the full coupling between thermo-plasticity and thermo-damage in thermodynamic modeling of dissipative materials, *International Journal of Solids and Structures,* 34, 61-92.

5. **Egner H.** (2013), Constitutive modelling of coupled problems of dissipative materials mechanics, *Seria Mechanika, Monografia 444,* Kraków (in Polish).

6. **Egner H., Egner W., Ryś M.** (2012), *Thermodynamics-based constitutive modeling of coupled dissipative phenomena in engineering materials*, Research and Applications in Structural Engineering, Mechanics and Computation – Zingoni, Taylor&Francis Group, London

7. **Egner H., Ryś M.** (2012), Modeling of coupling between damage and phase transformation in austenitic stainless steel at cryogenic temperatures, *Czasopismo Techniczne,* 8-M/2012, 22, (in Polish).

8. **Egner H., Skoczeń B.** (2010), Ductile damage development in two-phase materials applied at cryogenic temperatures, *International Journal of Plasticity,* 26, 488-506.

9. **Egner H., Skoczeń B., Ryś M.** (2014), Constitutive and numerical modeling of coupled dissipative phenomena in 316L stainless steel at cryogenic temperatures, *International Journal of Plasticity, 64, 113-133.*

10. **Fischer, F.D., Reisner, G., Werner, E., Tanaka, K., Cailletaud, G., Antretter, T.** (2000), A new view on transformation induced plasticity (TRIP), *International Journal of Plasticity,* 16(1-8), 723-748.

11. **Garion C., Skoczeń B.** (2002), Modeling of plastic strain induced martensitic transformation for cryogenic applications, *Journal of Applied Mechanics,* 69, 6, 755-762.

12. **Garion C., Skoczeń B., Sgobba S.** (2006), Constitutive modelling and identification of parameters of the plastic strain induced martensitic transformation in 316 L stainless steel at cryogenic temperatures, *International Journal of Plasticity,* 22, 7, 1234-1264.

13. **Hallberg H., Hakansson P., Ristinmaa M.** (2010), Thermo-mechanically coupled model of diffusionless phase transformation in austenitic steel, *International Journal of Solids and Structures,* 47, 1580-1591.

14. **Hallberg, H., Hakansson, P., Ristinmaa M.** (2007), A constitutive model for the formation of martensite in austenitic steels under large strain plasticity, *International Journal of Plasticity,* 23, 1213-1239.

15. **Hecker S. S., Stout M. G., Staudhammer K. P., Smith J. L.** (1982), Effects of strain state and strain rate on deformation-induced transformation in 304 stainless steel: Part I. Magnetic measurements and mechanical behaviour. *Metallurgical Transactions,* A 13A, 619626.

16. **Lemaitre H.** (1992), *A course on damage mechanics.* Springer-Verlag, Berlin and New York.

17. **Mahnken, R., Schneidt, A.** (2010), A thermodynamics framework and numerical aspects for transformation-induced plasticity at large strains, *Archives of Applied Mechanics,* 80, 229-253.

18. **Olson, G. B., Cohen, M.** (1975), Kinetics of strain-induced martensitic nucleation, *Metallurgical Transactions,* 6A, 791-795.

EVALUATION OF THE FERTILIZER GRANULES STRENGTH OBTAINED
FROM PLATE GRANULATION WITH DIFFERENT ANGLE OF GRANULATION BLADE

Tomasz LESZCZUK*

* Faculty of Mechanical Engineering, Bialystok University of Technology, ul. Wiejska 45C, 15-351 Bialystok, Poland

tomasz.leszczuk@wp.pl

Abstract: The goal of the paper was to assess the strength of the fertilizer granules obtained by non-pressure granulation method. The granulation process was carried out in plate granulator, according to the three-level experiment plan. A mixture of raw materials prepared in a Polish factory of agrochemicals for agriculture and horticulture was used as a study material and water was used as a wetting liquid. Granulator design parameters and process parameters were treated as entrance sizes of the experiment. Three different angles of granulation blade were used in experiments. This paper presents: the results of study of equivalent diameter size and the impact of changes in the angle of granulating blade on the strength of obtained granulate. Pfost apparatus and a set of sieves used in granulometric sieve were utilized in this study. A relation was suggested $P_\infty = f(\alpha, \chi, n, w_w, t)$. The results were presented in the form of graphs and tables. Conclusions were presented.

Key words: Non-Pressurized Granulating, Granulating Blade, Kinetic Strength of Granules, Agriculture and Horticulture Fertilizer

1. INTRODUCTION

One of the principal reasons for granulation of fine-grained materials is a need to eliminate dust. Furthermore, an additional advantage is that the material in granular form does not aggregate and can be dispensed easily. Solid horticultural and agricultural fertilizers are most frequently obtained during such process. Granulation process which involves aggregation of mostly small particles into larger assemblies is conducted in the presence of moistening liquid (Biskupski et al., 2008). So called non-pressure granulation is a process of production of solid particles with a certain size or shape from the fine material (Gluba et al., 2009a, b; Heim et al., 1991). Two mechanisms may take place during this process: the particles binds together without any other material, or the bonding forces are transmitted by the material bridges formed with a binder (Gluba et al., 2005, 2009c).

The vast majority of manufactured fertilizers are in the form of granules. In the considerable part, the position of fertilizer on the market depends on the method of its granulation and its application. In our country, we produce huge quantities of fertilizers, much more than it can be used. In this situation the manufacturing plants take steps to make their products more attractive. Therefore the share of granulated fertilizers in the total amount of manufactured fertilizers increases fertilizers properties are more adapted to the needs of customers and the properties of granulated fertilizers are improved (Borowik et al., 2012; Urbanczyk et al., 2008).

The mechanical strength of the granules is one of the basic properties of the granulation products which is decisive of its usefulness for further processing (Khan et al., 1997). Various methods of determination of granulate resistance refer to the different technological operations starting from obtaining a granulate up to its application. Two kinds of forces influence granules: the dynamic forces that accompany transport and static forces which act during storage. The kinetic and static strength (hard-ness) of granules are affected by many factors (Iveson et al., 1998a, b, c) including factors associated with physicochemical features of the raw materials and a method for the preparation of the pre-granulation, factors associated with the design of granulating system and technical and operational factors (Hejft et al., 2012; Zawiślak et al., 2010; Salman et al., 2004).

The knowledge of the impact of various parameters on the strength of the resulting granules allows for such a selection that product with best mechanical properties is obtained (Reynolds et al., 2005; Walker et al., 2003).

2. PAPER GOAL

The goal of the paper was to investigate the effect of changes in the angle of the granulation blade in plate granulator on the kinetic strength of the product obtained in the process of wet plate granulation.

3. APPARATUS AND METHODS OF MEASUREMENT

The study was conducted in a laboratory plate granulator. Scheme of the post is shown in Fig. 1. Scheme of the research post is presented in Fig. 2.

A granulator plate with a diameter of 0.5 m (1) was driven by an electric motor via a belt drive (3). The transfer of power from the transmission belt on a granulation plate was made via a gear mechanism (2). Frequency inverter (4) was used to determine the constant rotation speed of the plate.

The amount of drawn moistening liquid was showed by weight display (7), on which a moisturizing liquid container (5) was placed. Moisturizing liquid was delivered through rubber lines at a high pressure generated by the compressor (6).

The raw material was dosed into the bottom of the plate with the dispenser (8) and pre-wetted with a pneumatic spray nozzle (9) in the upper part. Rotational movement of the plate provided fluid delivery to the surface of bulk material. Constant intensity of liquid inflow was established with the use of rotameter (10). The granulation plate along with the instrumentation is fixed on supportive structure (11) (load-bearing structure).

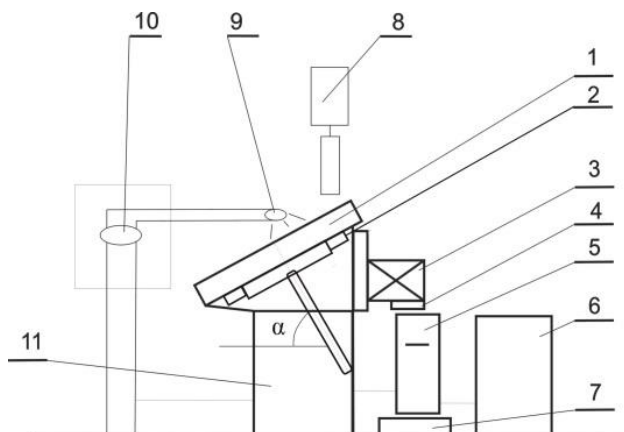**Fig. 1.** View of the research position of granulation harrow

Fig. 2. Scheme of the research post for plate granulation: 1 – replaceble granulation plate, 2 – a gear mechanism, 3 – electric motor with belt drive, 4 – frequency inverter, 5 – moisturizing liquid container, 6 – compressor, 7 – scales, 8 – raw material dispenser, 9 – spray nozzle, 10 – rotameter, 11 – supporting structure

A mix of raw materials, which has been manufactured and prepared at the factory of Polish manufacturer of agrochemicals for agriculture and horticulture, was used in the study. In the technological process, the mixture which is used as a raw material, is transformed into the granulated agricultural fertilizer. Water with a density $\rho = 1000 \, kg/m^3$ at constant flow rate was used as the moistening liquid.

The analysis of granulation was conducted in the periodic way, at fixed weight of the granulated batch equal 2.52 kg. Tests were performed according to the study of Hartley PS/DS-P: Ha5 (Polański, 1984) in which:
- considered amount of entrance sizes $i = 5$;
- considered number of plan arrangements $X = 27$;
- plan star shoulder $\xi = 1$;
- amount of levels of the given entrance size
  $n_x = 3 \,(+1, 0, -1)$.

The selection of independent variables (experiment entrance sizes) was based on a literature review.
Entrance sizes:
- $x_1 = \alpha$ – the angle of the granulation plate;
- $x_2 = \chi$ – the angle of the blade in the plate granulation;
- $x_3 = n$ – the rotation speed of the granulation plate;
- $x_4 = w_w$ – mass of water added into the plate during the granulation process;
- $x_5 = t$ – material stay time in the granulator.

Before the beginning of the process – granulation plate and granulation blade were placed at the determined angle. Powdered material was placed in the bottom part of the granulation plate. The poured deposit was rinsed with proper amount of granulation liquid. Granulator drive was started and the speed of the plate was set. The process continued until the established time of material stay in granulator ended. The change of the granulation blade tilt angle was presented in the Fig. 3, 4, 5. Fig. 3 Blade position at the angle of 60°. Fig. 4 Blade position at the angle of 90°. Fig. 5 Blade position at the angle of 120°.

Geometric parameters of the granulation blade were determined on the basis on preliminary tests, which results were also included in the publication of Hejft and Leszczuk (2012).
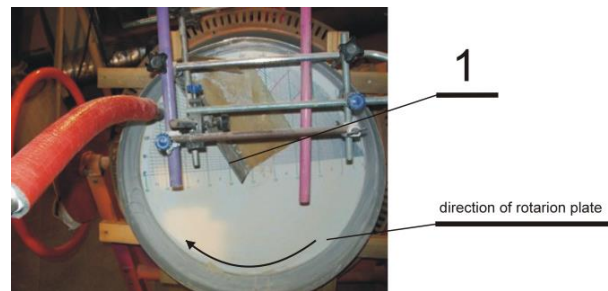

Fig. 3. The position of the granulation blade in the granulation plate at the angle of 60°, 1 – granulation blade

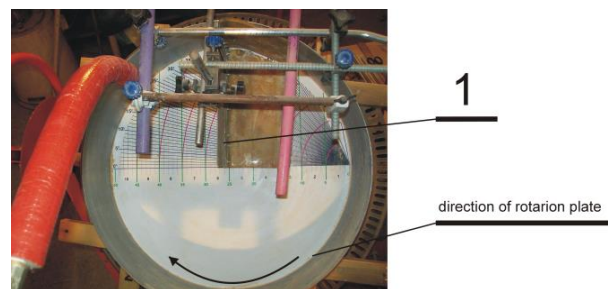

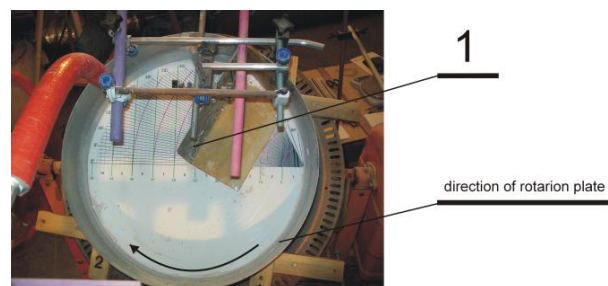**Fig. 4.** The position of the granulation plate in the granulation plate at the angle of 90°, 1 – granulation blade

Fig. 5. The position of the granulation blade in the granulation plate at the angle of 120°, 1 – granulation blade

Sieve analyser was used to determine the equivalent diameters of the obtained granulate. Dry sieve analysis was performed according to ISO 2591-1: 2000, using a mechanical shaker (MULTISERW Morek type LPzE-2e). The post was described on Fig. 6.

Fig. 6. Place of the determination of granules equivalent diameter

The principle of this analysis is based on a mechanical sieving of the sample through a set of sieves and weighing the individual fractions. In this method, grain material was divided into fractions containing particles with different sizes, by sieving through a set of sieves. As a result, the grain with given diameters stayed on successive sieves (with decreasing mesh sizes). Randomly selected granule samples with the weight of 0.300 kg were taken for analysis. Individual size factions were weighed at the electronic scale. After weighing of individual grain classes, the percentage share of material which stayed on every sieve against the whole material was determined. Based on received results, a substitute diameter of the set of particles dm was calculated on the basis of the formula (Urbańczyk et al., 2008) (model 1).

$$d_m = \sum_{i=1}^{n} m_i \cdot d_{\text{śri}} \tag{1}$$

In case of sieve analysis parameter: $d_{\text{śri}}$ – the arithmetic mean of the extreme dimensions of the fraction i – the average size of largest and smallest mesh for the given class of grain, m_i – mass share of individual grain classes.

Kinetic strength of the obtained granulate P_∞ was determined according to PN-R-64834: 1998. Pfosta apparatus is rectangular, metal tank with specific dimensions with the transversely placed plate. The testing machine was presented in Fig. 7.
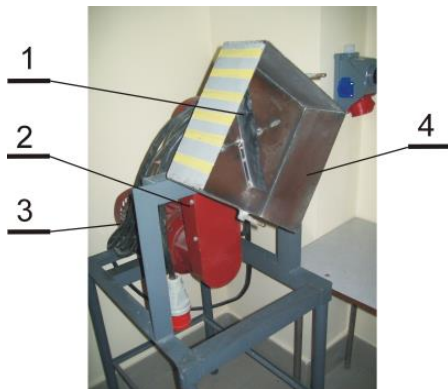

Fig. 7. Apparatus for testing the kinematic strength of granules:
1 – stationary steel plate, 2 –transmission belt, 3 – electric motor,
4 – tester box

Rotary tester has a chamber (box) (4) with dimensions of $285x285x120$ mm, in which the steel plate (1) with dimensions of $230x50x2$ mm is placed. The drive of apparatus is accomplished by an electric motor (3) and transmission belt (2).

A sample with mass of c.a. 500 g was inserted into the box of the testing machine. It rotated for 10 min at 50 rpm/min. After the test, particles which disintegrated were separated on a sieve with a mesh diameter $\phi = 1$ mm. The kinetic strength of the granules P_∞ is defined as the ratio of sample weight after the test m_2 (without the share of $0 \div 1$ mm fraction) to the weight of sample charged into the tester m_1 (Błasiński et al., 1981) (model 2):

$$P_\infty = \frac{m_2}{m_1} \cdot 100 \tag{2}$$

3. RESEARCH RESULTS

Based on the obtained research results an analysis of the influence of granulation blade tilt angle on kinetic strength of obtained granules was made tilt. To make the results more clear they were divided into three groups. Table 1 contains the results obtained for granulate at the angle tilt of 60°. Tab. 2. contains the test results of the obtained granulate at the granulation vane tilt angle of 90°. Tab. 3 contains the test results obtained for granulate at the granulation blade tilt angle of 120°.

Tab.1. Test results (angle of the blades 60°)

	independent variables						
	1	**2**	**3**	**4**	**5**	**6**	**7**
plan	$x_1 = \alpha$	$x_2 = \chi$	$x_3 = n$	$x_4 = w_w$	$x_5 = t$	P_∞	d_m
number	[°]	[°]	[rpm]	[kg]	[min]	[%]	[mm]
2.	30	60	21.6	0.324	14.0	92.9	69.01
4.	50	60	7.2	0.252	8.0	84.4	3.1
6.	50	60	7.2	0.324	14.0	51.2	4.91
8.	30	60	21.6	0.252	8.0	92.2	3.71
10.	50	60	21.6	0.324	8.0	57.8	11.71
12.	30	60	7.2	0.252	14.0	86.4	4.28
14.	50	60	21.6	0.252	14.0	86.2	4.7
16.	30	60	7.2	0.324	8.0	85.2	6.23
20.	40	60	14.4	0.288	11.0	89.8	9.46

Tab. 2. Test results (angle of the blades 90⁰)

	independent variables						
	1	**2**	**3**	**4**	**5**	**6**	**7**
plan	$x_1 = \alpha$	$x_2 = \chi$	$x_3 = n$	$x_4 = w_w$	$x_5 = t$	P_∞	d_m
number	[°]	[°]	[rpm]	[kg]	[min]	[%]	[mm]
17.	50	90	14.4	0.288	11.0	82.2	4.31
18.	30	90	14.4	0.288	11.0	92.0	8.07
21.	40	90	21.6	0.288	11.0	94.5	3.62
22.	40	90	7.2	0.288	11.0	90.6	2.33
23.	40	90	14.4	0.324	11.0	91.6	8.05
24.	40	90	14.4	0.252	11.0	91.8	3.60
25.	40	90	14.4	0.288	14.0	95.4	6.45
26.	40	90	14.4	0.288	8.0	93.6	4.45
27.	40	90	14.4	0.288	11.0	95.0	5.97

Tab. 3. Test results (angle of the blades 120^0)

	independent variables						
	1	**2**	**3**	**4**	**5**	**6**	**7**
plan	$x_1 = \alpha$	$x_2 = \chi$	$x_3 = n$	$x_4 = w_w$	$x_5 = t$	P_∞	d_m
number	[°]	[°]	[rpm]	[kg]	[min]	[%]	[mm]
1.	50	120	21.6	0.324	14.0	36.8	8.93
3.	30	120	7.2	0.252	8.0	74.8	1.72
5.	30	120	7.2	0.324	14.0	45.2	6.98
7.	50	120	21.6	0.252	8.0	82.1	2.32
9.	30	120	21.6	0.324	8.0	85.8	9.14
11.	50	120	7.2	0.252	14.0	87.2	1.85
13.	30	120	21.6	0.252	14.0	93.4	5.20
15.	50	120	7.2	0.324	8.0	78.0	4.31
19.	40	120	14.4	0.288	11.0	87.2	6.35

Based on the obtained results (Tab. 1, 2, 3), relationship of granule kinetic strength P_∞ in a function of the input parameters of the experiment (model 3) was developed:

$$P_\infty = -631.62 + 10.27\alpha + 1.61\chi + 4.77n$$
$$+ 2562.41w_w - 0.08\alpha^2 + 0.01\alpha\chi$$
$$- 13.61\alpha w_w - 0.04\alpha t - 7.1$$
$$\cdot 10^{-3}\chi^2 - 2.6 \cdot 10^{-3}\chi n$$
$$- 1.72\chi w_w - 0.04\chi t - 0.04n^2 \qquad (3)$$
$$- 1.78n w_w + 0.13nt$$
$$- 2435.97w_w^2 - 60.69w_w t$$
$$+ 0.09t^2$$

On the basis of the test results and the regression equation (model 3) significant effects of all independent variables on the value of the average kinetic strength of granules was shown. As presented on the Fig. 7 kinetic strength is highest when the granulation plate is at the angle of about $38° \div 42°$ and the granulation blade at the angle of $90° \div 80°$.
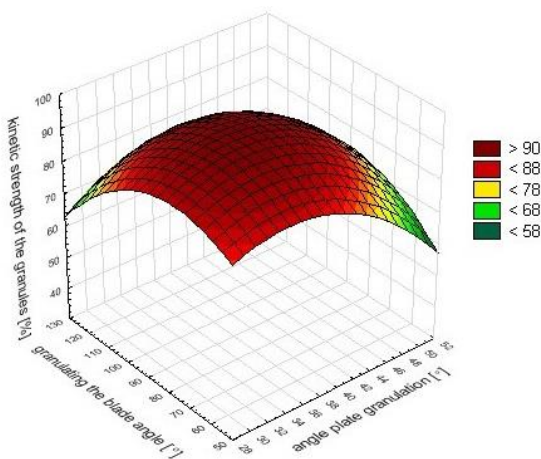

Fig. 8. The influence of the design parameters (blade and granulation plate tilt angle) on the granule kinetic strength measured by Phost apparatus

Fig. 9 depicts an exemplary association between granulation blade χ tilt angle and granules kinetic strength P_∞.

The change of granulation time from 8 min to 11 min (at the granulation plate tilt angle of $\alpha = 30°$, granulation plate rotation

speed $n = 14.4$ rpm/min, amount of liquid added to the granulation plate $w_w = 0.324$ kg) results in decrease of the granule kinetic strength P_{dx} from the value of 85,9 % to 69.9 %.
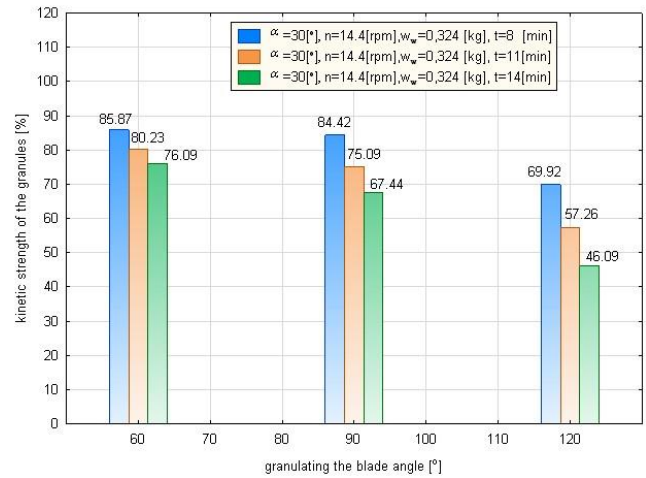

Fig. 9. Impact of the granulation blade tilt angle on the granule kinetic strength measured by Phosta apparatus

At the total time of granulation $t = 11$ min (the rest of granulation parameters: granulation plate tilt angle $\alpha = 30°$, granulation plate rotation speed $n = 14.4$ rpm/min, amount of liquid added to the granulation plate $w_w = 0.324$ kg) the granule kinetic strength P_{dx} changes from the value of 80.2 % through 75.1 % to 57.3 %.

Similar situation occurs when the granulation time is $t = 14$ min. At that time granule kinetic strength P_{dx} decreases from the value of 76.1 % to 46.1%.

The change of the granulation blade tilt angle from 60° to 120° (at the granulation plate tilt angle of $\alpha = 30°$, granulation plate rotation speed $n = 14.4$ rpm/min, amount of liquid added to the granulation plate $w_w = 0.288$ kg) during the granulation time $t = 14$ min results in the decrease of the granule kinetic strength P_{dx} for 26.3 % from the value of 87.6 % to 61.3 % (Fig. 10).
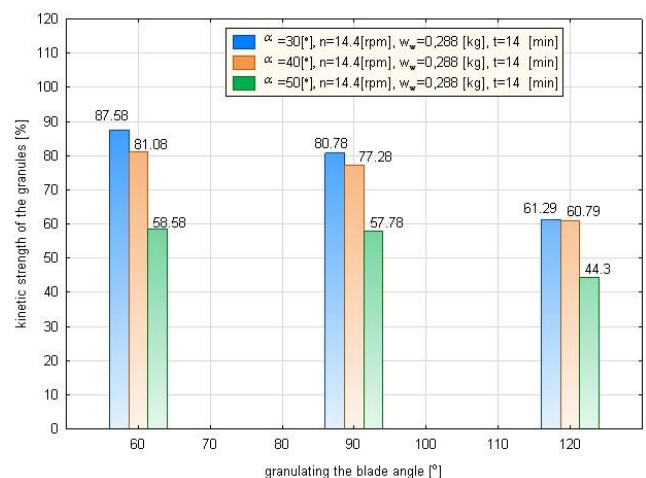

Fig. 10. Impact of the granulation blade tilt angle on the granule kinetic strength measured by Phosta apparatus

The change of the granulation blade tilt angle from 60° to 120° (at the granulation plate tilt angle $\alpha = 40°$, granulation plate rotation speed $n = 14.4 \, \text{rpm/min}$, amount of liquid added to the granulation plate $w_w = 0.288 \, \text{kg}$ and granulation time $t = 14 \, \text{min}$) results in the decrease of the granule kinetic strength P_{dx} for 20.3 from the value of 81.1 % through 77.3 % to 60.8 %.

The change of the granulation blade tilt angle from 60° to 120° (at the granulation plate tilt angle $\alpha = 40°$, granulation plate rotation speed $n = 14.4 \, \text{rpm/min}$, amount of liquid added to the granulation plate $w_w = 0.288 \, \text{kg}$ and the granulation time $t = 14 \, \text{min}$) results in the decrease of the granule kinetic strength P_{dx} by 14.3 % from the value of 58.6 % to 44.3 %.

4. CONCLUSIONS

- The kinetic strength of the product obtained by wet granulation substantially depends on the design parameters of the granulator. The placement of the granulation blade in the granulator plays here a key role.
- Obtained results show that the greatest granules kinetic strength is received when the granulation blade tilt is at the angle of 60°.
- Granulation blade tilt at the angle of 120° (in each point of the experiment) was associated with the accumulation of granules in the upper part of plate, right at the working surface. This resulted in the formation of granules with reduced mechanical properties.
- Analyses have also shown that the surface of the granulation blade is an obstacle for the bulk material particles located on the plate, which, by interaction with the powder material results in higher density of grains in the granules. An increasing number of contacts between the grains increases the binding strength due to greater convergence of grains. This results in the increase of resistance of granules towards the external forces, including compressive forces.
- The use of granulating blade at the angle of 60° and 90° (at different process - apparatus parameters) affects the increase in the equivalent diameter of the collection of particles (determined from the sieve analysis). It is the result of a more intense movement of the bed on a plate, affecting the frequency and strength of the interactions between the pouring deposit particles.

REFERENCES

1. **Biskupski A., Picher W.** (2008), Granulation method used in domestic fertilizer factories and properties of the obtained products, *Chemist*, 9, 398-408.
2. **Błasiński H, Gluba T.** (1981), Methods and apparatus for measuring the strength of the agglomerates, *Chemical Engineering and Equipment*, 4, 29-33.
3. **Borowik M., Malinowski P., Biskupski A., Dawidowicz M., Schab S., Rusek P., Igras J., Kęsik K.** (2012), Technology of fertilizer nitrogen-sulfur-calcium based on phosphogypsum and urea, *Chemist*, 66, 5, 535-540.
4. **Gluba T., Obraniak A.** (2009a), Evaluation of resistance to abrasion of the granular compound fertilizers Lubofoska, *Chemical Engineering and Equipment*, 4, 48-49.
5. **Gluba T., Obraniak A.** (2009b), Evaluation of the wet granulation harrow product, *Chemical Engineering and Equipment*, 4, 50-51.
6. **Gluba T., Obraniak A.** (2009c), The kinetics of agglomeration of particulate material in the granulator harrow, *Chemical Engineering and Equipment*, 4, 46-47.
7. **Gluba T., Obraniak A., Gawot-Młynarczyk E., Błaszczyk M.** (2005), Influence of the wetting parameters on the compressive strength of the granules, *VII National Granulation Symposium 2005, Puławy-Kazimierz Dolny.*
8. **Heim A., Gluba T., Kochański B.** (1991), Evaluation of mechanical properties of products from tumbling granulation, *IV National Granulation Symposium, Puławy.*
9. **Hejft R., Leszczuk T.** (2012), Effect of the scraping elements in the granulator harrow for the process, *Chemist*, 66, 5, 370-375.
10. **Iveson S. M., Litster J. D.** (1998a), Liquid – bound granule impact deformation and coefficient of restitution, *Powder Technology*, 99, 234-242.
11. **Iveson S. M., Litster J. D.** (1998b), Fundamental studies of granule consolidation – part 2. Quantifying the effect of particle and binder properties, *Powder Technology*, 99, 243-250.
12. **Iveson S. M., Litster J. D.** (1998c), Growth regime map for liquid – bound granules, *A. I. Ch. E. J.*, 44, 1510-1518.
13. **Khan M. I., Targos G. I.** (1997), Stability of wet agglomerates in granular shear flows, *J. Fluid Mechanics*, 347, 347-348.
14. **Polański Z.** (1984), *Designing experiments in the technique*, PWN, Warsaw.
15. **Reynolds G. K., Fu J. S., Cheong Y. S., Hounslow M. J., Salman A. D.** (2005), Breakage in granulation: A review, *Chemical Enginering Science*, 60, 3969-3992.
16. **Salman A. D., Reynolds G. K., Fu J. S., Cheong Y. S., Biggs Y., Adams C., Gorham M., Lukenics D., Hounslow J.** (2004), Descriptive classification of the impact failure modes of spherical particles, *Powder Technology*, 143-144, 19-30.
17. **Urbańczyk L., Wantuch W., Kotowicz J., Kowalski Z., Biskupski A., Malinowski P.** (2008), Specification of the compound fertilizer granulation using defective materials, *Chemist*, 9, 393-397.
18. **Walker G. M., Moursy H. E. M. N., Holland C. R., Ahmad M. N.** (2003), Effect of process parameters on the crush strength of granular fertilizer, *Powder Technology*, 132, 81-84.
19. **Zawiślak K., Sobczak P., Panasiewicz M., Markowska A.** (2010), Effect of selected technological parameters on the granules kinetic strength, *Acta Sci. Pol., Agraria Technica, 9 (1-2), 3-10.*

FAILURE ANALYSIS OF A FEMORAL HIP STEM MADE OF STAINLESS STEEL AFTER SHORT TIME OF EXPOSURE

Żaneta Anna MIERZEJEWSKA[*], Zbigniew OKSIUTA[*]

[*]Faculty of Mechanical Engineering, Division of Materials and Biomedical Engineering, Bialystok University of Technology,
ul. Wiejska 45c, 15-351 Białystok, Poland

a.mierzejewska@doktoranci.pb.edu.pl, z.oksiuta@pb.edu.pl

Abstract: This paper describes a case study summarising the failure analysis of a stainless steel femoral stem, which failed prematurely within 36 months of exploitation in human body. In order to determine the mechanism of failure, a broken stem component were analyzed by means of macroscopic and microscopic obserwations and hardness measurements. Metallurgical obserwations revealed that the tested material does fulfill ASTM requirements. Scanning electron microscopy images revealed the presence of stress-induced cracking. The results of the hardness revealed significant nonuniformity from the surface towards the inner part of the stem. It is assumed that any discontinuity or defect on the fracture surface of the stem acted as preferential site for a crack nucleation and propagation by fatigue until the cross section of stem was not able to sustain a load generated by a patient.

Key words: Hip Replacement, Endoprosthesis Stem Fracture, Isolated Fracture, Total Hip Arthroplasty Complications, Fatigue Fracture

1. INTRODUCTION

Human locomotor system is composed of interrelated ligaments by means of joints and muscles, which are controlled by the nervous system (Dalaunay et al.,1996). A properly built and functioning hip joint allows for a smooth range of motion in multiple planes. Any disease in the joints may lead to their harm, causing its deformation, pain and loss of functionality. Total hip arthroplasty is one of the most successful practices in orthopedics, which restores the correct function of the hip joint disrupted by fracture or disease (rheumatoid arthritis, hip dysplasia, avascular necrosis of the femur) (Scheerlinck et al., 2004; Griza et al., 2013). This procedure intends to remove damaged articular joints and replace them with an artificial hip joint. During service life, artificial implants are exposed to an aggressive environment such as corrosion, wear and severe loading (Kamachi et al., 2003). These factors results in a wide range of failure mechanisms. One of the most serious complication is isolated stem fracture, consisting in breaking the implant inside the intramedullary canal, without damaging surrounding bone tissue. An incidence of this complication varies with many factors, including the patient population, for example the body mass index (BMI), physical activity, bone sideases or age and the geometry of the implant as well as kind of materials from which the artificial joint is made (Galante et al., 1980; Martens et al., 1974).

Biomaterials belong to the group of modern materials which are used for the replacement and reconstruction of human body. A very important group of biomaterials are metallic alloys, e.g.: stainless steels, Co-Cr alloys and Ti alloys. One of the common biomaterial used for bone implants and surgical instruments are austenitic stainless steels. Good mechanical properties, adequate biocompatibility and relatively low price of those alloys make them very suitable material for biomedical applications. The most popular stainless steels used for medical applications are 316L (ASTM A276-98b) and Rex 734 (ASTM F1586) grade.

An isulated failure of the femoral component after total hip arthroplasty is not a common occurrence from a statistical point of view, however there are some cases of stems fractures reported in the literature (Charnley, 1975; Mollan et al., 1985; Wilson et al., 1992; Malchau et al., 2002; Lakstein et al., 2011).

Roffey et al. (2012) described an isolated fatige fracture of the stem made of austenitic stainless steel after relatively short time of implantation ~ 4.5 years. The microstructure, hardness and chemical analysis of the fractured stem revealed good agreement with ISO standard requirements for such kind of implants. No defects such as cracks, non-metallic inclusions or corrosion were detected during observations of the fractured area. Also, the microstructure of the stem was homogeneous, with fine grains, typical for wrougth austenitic stainless steel. Detailed analysis of the fracture surface revealed two points of fracture initiation located on opposite sides of the stem. The location of these points, and the direction of the propagation of fatigue striations suggested that the stem fracture was caused by torsional loads.

Jarvi et al. (2007) also described an interesting case of a quadruple fracture of stem made of austenitic stainless steel, 316L grade, after 4 years from imlpantation. Around the stainless steel stem granulation tissue was observed, which according to the authors knowladge could be due to wear products of acetabular cup. Striations on the fracture surfaces of the stem were observed as the result of a fatigue failure.

The most curious case of double isolated stem fracture, also made of austenitic stainless steel after 4.5 years of implantation, was described by Sen et al. (2009). On the basis of observations of the fracture area the authors proposed a hypothesis that the damage was caused by cyclic-variable load, leading to fatigue fracture.

Hernandez-Rodriguez et al. (2010) observed failure mechanism of the 316LV stainless steel stem where a main crack was originated on the anterolateral corner section of the material. Note that most of the cases reported in the literature concern the stem

fracture made of 316 LV stainless steel grade, and there is no available information about fracture of the other kind of austenitic stanless steel, e.g. REX 734.

The main goal of this work is to analyse and describe a failure mechanism of a hip stem made of austenitic stainless steel, REX 734 grade, after relatively short time of implantation, less than 3 years.

2. EXPERIMENTAL PROCEDURE

General image of the fractured stem is shown in Fig. 1. After revision, two parts of the fractured stems were prepared to further analysis. A small piece of material was cut from the stem and prepared for metallographic observations according to ASTM E1306-11 standard. The chemical composition of the stainless steel was examined by means of a spark emission spectroscopy (Thermo ARL Quantris, Switzerland). Microstructure observations after etching by means of the Vilella's echant (picric acid 1 g; HCl 5 ml; ethanol 100 ml) were carried out by an optical microscope (OM) a Nikon Eclipse LV1000. The fracture surfaces of stem were examined by means of Scanning Electron Microscopy (SEM) Hitachi S-3000N, equipped with Energy Dispersive Spectroscopy (EDS). Hardness measurements were performed using Vickers universal indenter with a load of 5 kg. Grain size and hardness measurements were performed according to ASTM standards E112 and E384, accordingly.

150 [mm]

Fig. 1. General view of the fractured stainless steel stem

3. RESULTS AND DISCUSSION

The results of chemical analysis of the tested steel, presented in Tab. 1, revealed that the material of stem, in general, fulfils the requirements of ASTM F1586. However, there are some differences in chemical composition of the tested stem in comparison with the ASTM F1586 standard. Sulphur content is slightly higher than specified, whereas the nickel content is slightly reduced. Note that nitrogen, an element that stabilise a Fe-γ phase was not detected in the sample. It is well known that in austenitic stainless steels chrome and nickel concentration and their equivalent elements content play very important role for stabilisation of the FCC phase structure. Chromium and nickel equivalents can be calculated according to Equations (1) and (2).

$$R_{Cr} = (\%Cr) + (\%Mo) + 1.5(\%Si) + 0.5(\%Nb) + 2(\%Ti) \quad (1)$$

$$R_{Ni} = (\%Ni) + 30(\%C + \%N) + 0.5(\%Mn) \quad (2)$$

Calculated Cr- and Ni- equivalents exhibited 12.80% and 22.75%, respectively. Therefore, fully austenitic structure is expected. This was confirmed by the XRD measurements of the tested stem (not presented here).

Tab. 1. Chemical composition of the stems and ASTM F1586 standard (% weight)

	C	Si	Mn	P	S	Nb
ASTM F 1586	0.08[a]	0.75	2-4.25	0.025[a]	0.01[a]	0.25-0.8
Sample	0.036	0.27	4.1	0.002	0.015	0.39
	Cr	Mo	Cu	Ni	N	
ASTM F 1586	19.5-22	2-3	0.25[a]	9-11	0.25-0.5	
Sample	21.14	2.33	0.036	7.05	-	

([a] – maximum content)

SEM-EDS linear analysis was also performed to observe changes in the concentrations of main alloying elements along a cross-section of the stem as it is presented in Fig. 2a. The results presented in Fig. 2b confirmed a homogeneous distribution of alloying elements in the steel matrix.
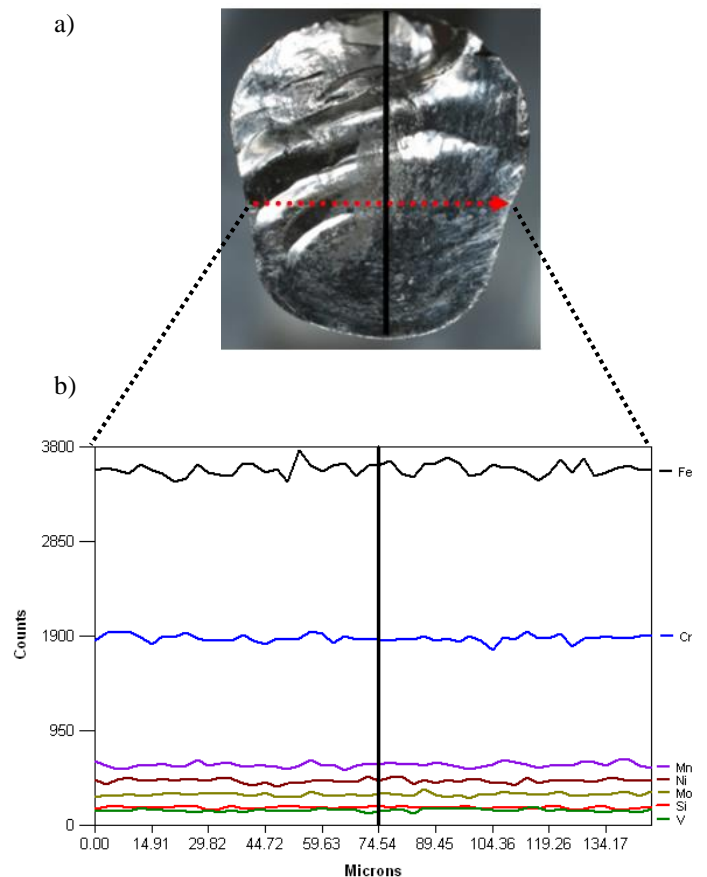
a)

b)

Fig. 2. SEM-EDS linear analysis of the elements concentration on the surface of the stem – (a) macroscopic view (b) – elements distribution

OM image of the etched microstructure of the tested sample, presented in Fig. 3 showed equiaxed austenitic grains and twins characteristic for forged and annealed austenitic stainless steels. Note, that no delta ferrite was observed.

In general, the microstructure is quite homogeneous, with an average grain size of 36±3 μm (no 7 according to ASTM). However, larger grains near the surface of the stem were also observed which may cause an origin of a fatigue crack initiation of the steel (Fig. 3b). This inhomogeneity of the grain size is difficult to explain, however, this may be related to hardness results presented in the section 3.3 (Fig. 6).
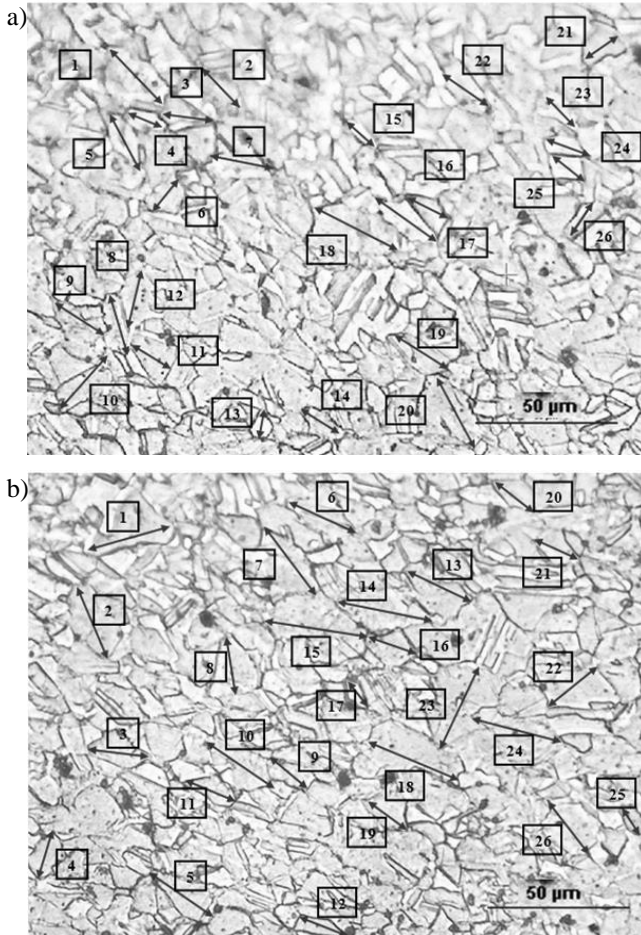

Fig. 3. Typical OM microstructure of the femoral stem;
(a) taken from inside of the stem
(b) taken from an edge of the stem

Fig. 4 shows a general view of the fractured surface of the tested material. The image shows a several distinctive features typical for fatigue fracture: an origin where a crack can be initiated (zone a), fatigue striations (zone b), and a final fracture area (zone c). The fatigue fracture probably was initiated close to the lateral edge of the material, and further propagated until a cross section of the stem was no longer strong enough to bearing the applied load and it finally broke. The fatigue zone is unique to fatigue fractures because it is the region where the crack grows from the origin to the final fracture zone. It should be pointed out that the geometry of the fractured stem did not reveal any changes. No bending of stems was observed. Also, no traces of corrosion were discovered.

Fig. 5 shows SEM images of the fractured surface. Fig. 5a presents the magnified cracks initiation region whereas Fig. 5b shows some of the "beach marks" (progression lines) area. Each mark

or line was created when the crack stops after short distance propagation. These patterns are not clearly visible, probably because the fracture surfaces were severally smashed, as a result of friction of both broken parts during prolonged walking after fracture. There is another possible explanation reported by Brown (2014) and related to very fine microstructure of steel or unchanged load during fatigue damage.
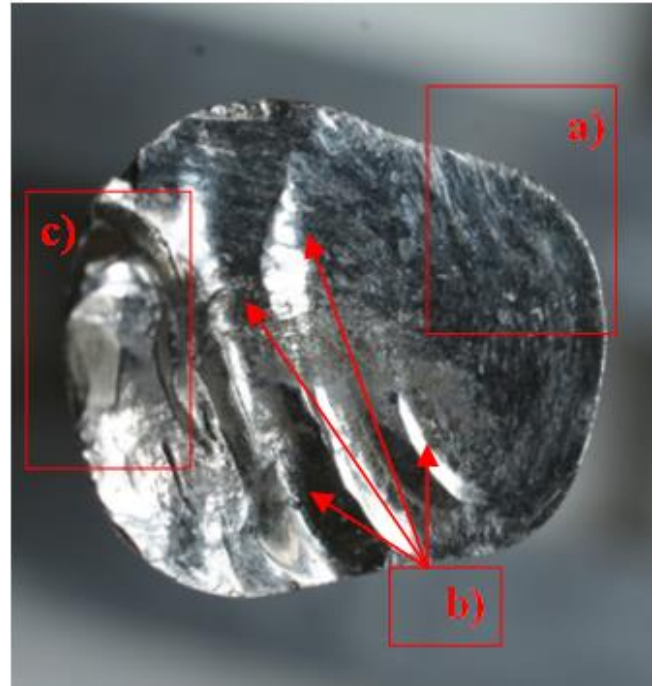
Fig. 4. Fatigue surface with fracture view showing the zones:
a) an origin, b) progression lines
c) and a final fracture zone

As the cracked stem continues to be stressed, the crack progresses across the section. The amount of material carrying the load is decreasing, so the stress is obviously increasing. Fig. 5c confirms extensive friction islands at the fracture surface, however higher magnification image in Fig. 5d shows typical fatigue striations. In Fig. 5e numbers of secondary cracks were observed, propagated perpendicular to the loading direction. The length of these cracks corresponds well to the grain size of the steel. This type of fracture may be caused by the presence of non metallic inclusions. Fig. 5f shows the SEM image of the final fracture stage, where the unbroken area is reduced to the point that the applied stress exceeds the ultimate strength of the material.

The origin of fatigue fracture commonly takes place in the anterolateral site of the hip stem due to the highest stresses created under in-service conditions.

The hardness measurements of both parts of the broken stem was performed few milimeters below and above of the fracture. An average hardness of tested material is ~ 335 HV/5 and fulfils ASTM requirements. However, an interesting effect was observed, not equal and strong dependence of hardness of the measurement site. In the middle of the cross section of the stem the hardness is 360 ± 2 HV/5 and close to the edge of the cross section of the specimen is about 10% lower, 325±5 HV/5 (see Fig. 6).
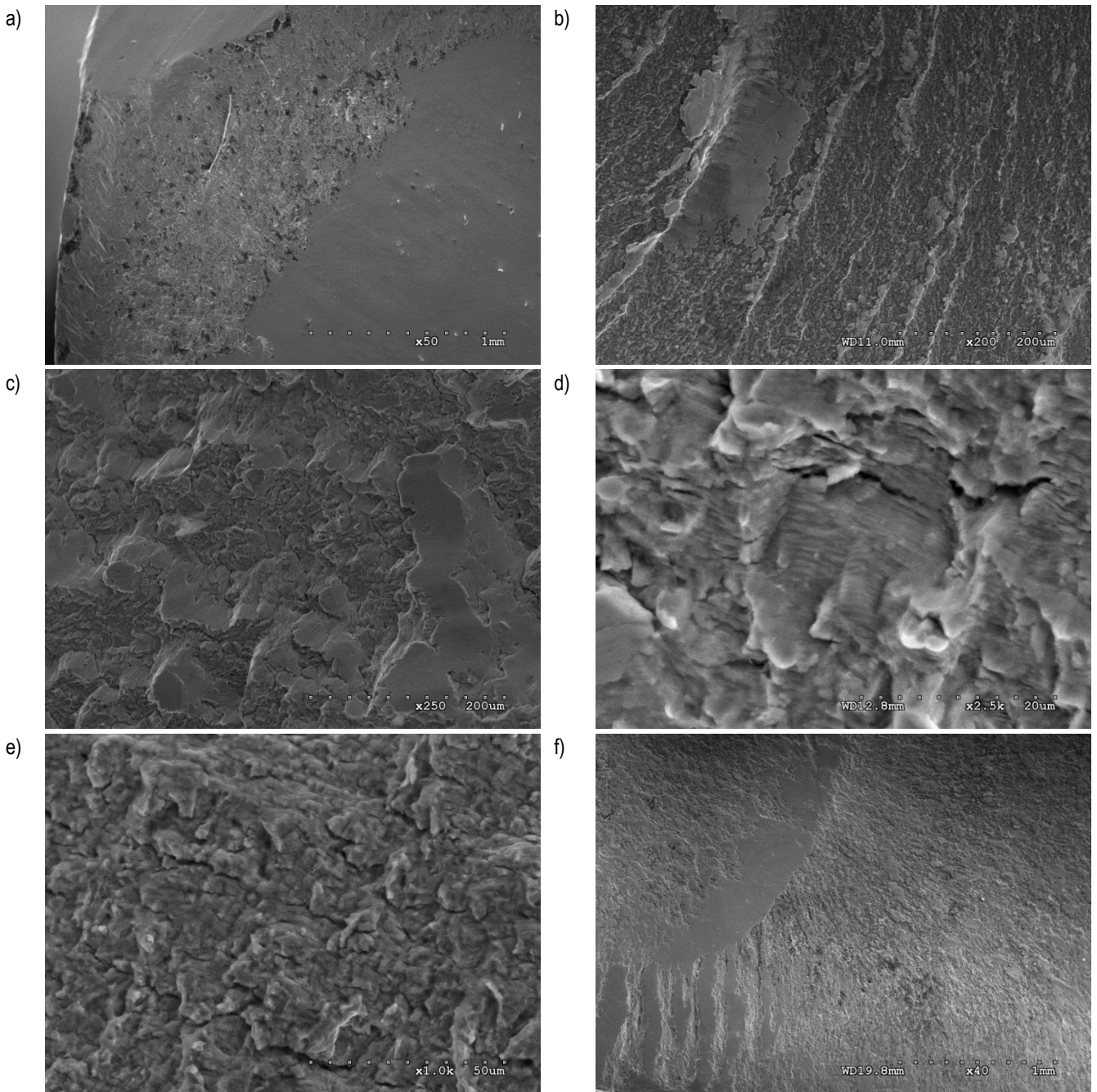
Fig. 5. SEM images of the fracture surfaces of the tested steel failed by fatigue fracture demonstrating: (a) origin of the failure (b) beach marks area; (c) wear islands on the fracture surface ; (d) fatigue striation; (e) secondary cracks and fatigue tears; (f) final fracture area
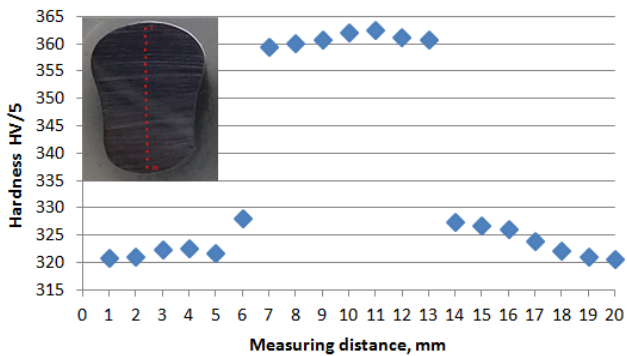
Fig. 6. Hardness measurements of the tested stem as a function of the distance from the edge of the sample

It is not a significant scutter of the hardness of the tested specimen, however it is difficult to explani, because these results are not consistent with the microstructure observations presented in Fig. 3. According to the Hall-Petch equation (Petch, 1953) with decreasing the grain size the ductility and hardness of the material increase. On the other hand this statemant is not valid for some groups of materials, especially with subgrain microstructure.

Stem fracture in the femoral component of total hip arthroplasty may have a complex etiology. The most important factors that cause fracture of metallic stem should be mentioned: the hidden material defects, incorrectly realized thermo-mechanical and /or heat treatment, improper design of the implant (incorrectly matched to the load), improper fixing in the bone or inapropriate exploitation (Galante et al., 1980; Kishida et al., 2012). The fracture of femoral

stem may be also caused by one factor or the combination of factors including: high stress applied in the stem due to high level of activity or fast patient weight gain, undersized prosthesis, poor proximal bone support or fixation, varus orientation of the stem and material defects.

Series of tests conducted in this work revealed that the REX 734 stainles steel in general fulfills ASTM F1586 standard requirements. The microstructure of the stem is homogeneous and possesses relatively small grains. There are no changes caused by intergranular or pitting corrosion, since homogeneous distribution of main alloying elements, especially chromium, were detected.

On the contrary the results of the hardness revealed measurable inhomogeneity coming from the edge towards innert part of the material. This is difficult to explain and more tests have to be conducted.

Macroscopic fatigue striations, commonly known as beach marks, were visible. The beach marks were closely spaced indicating a large number of cycles to failure, which eliminates the possibility of sudden overload failure. Final failure occurred on the lateral side corner. SEM examination of the fractured surface revealed secondary cracks, which are the result of tensile and compressive stresses induced in the material during patient's walking.

4. CONCLUSION

The main goal of this work was to analyse and describe a failure mechanism of cemented hip stem made of austenitic stainless steel, REX 734 grade. The tested material, in general, fulfils ISO 5832-1 standard, however, there are some factors such as: lower Ni and N content, inhomogenous grain size, higher hardness measured in the inner part of the stem and secoundary cracks initiated at the non-metalic inclusions, that can explain early fracture of the hip endoprosthesis after 3 years of implantation.

REFERENCES

1. **Brown T.** (2012) Preventing Mechanical Failures - An Introduction to Failure Mode Identification, *A Culture of Reliability*, Vol. 3, 46-48.
2. **Charnley J.** (1975), Fracture of femoral prostheses in total hip replacement : a clinical study. Clin Orthop, 1 1 1 :105-20.
3. **Delaunay, C. P., Kapandji, A. I. (**1996), Primary total hip arthroplasty with the Karl Zweymuller first-generation cementless prosthesis: a 5 to 9 year retrospective study, *J. Arthroplasty*, 11, 643.652.
4. **Galante J.** (1980), Current Concept Review Causes of Fractures of the Femoral Component in Total Hip Replacement, *Journal of Bone and Joint Surgery*, Vol. 62 (4), Vol. 62(4), 670-673.
5. **Griza S., Vieira dos Santos S., Ueki M. M., Bertoni F., Strohaecker T.R.** (2013), Case study and analysis of a fatigue failure in a THA stem, *Engineering Failure Analysis*, 28, 166–175.
6. **Hernandez-Rodriguez M. A. L., Ortega-Saenz J. A., Cotreras-Hernandez G. R.** (2010), Failure analysis of a total hip prosthesis implanted in active patient, *Journal of the Mechanical Behavior of Biomedical Materials*, Vol. 3 (8), 619-622.
7. **Jarvi K., Kerry R. M.** (2007), Case Report Segmental Stem Fracture of a Cemented Femoral Prosthesis, *The Journal of Arthroplasty*, Vol. 22(4), 612–616.
8. **Kamachi M. U., Sridhar T. M., Eliaz N., Baldev R. A. J.** (2003), Failures of stainless steel orthopaedic devices: causes and remedies, *Corros Rev*, 21, 231-67.
9. **Kishida Y.,Sugano N., Ohzono K., Sakai T., Nishii T., Yoshikawa H.** (2002), Stem Fracture of the Cementless Spongy Metal Lu¨ beck Hip Prosthesis, *The Journal of Arthroplasty*, Vol. 17 (8), 1021–1027.
10. **Lakstein D., Eliaz N., Levi O, Backstein D., Kosashvili Y., Safir O., Gross A. E.** (2011), Fracture of Cementless Femoral Stems at the Mid-Stem Junction, *J Bone Joint Surg Am.*, 93, 57-65.
11. **Malchau H, Herberts P, Eisler T, Garellick G, Soderman P**. (2002), The Swedish Total Hip Replacement Register, *J Bone Joint Surg Am*, 84-A, Suppl 2, 2-20.
12. **Martens M., Aernoudt E., De Meester P., Ducheyne P., Muller J. C., Delangh R., Kestelijn P**. (1974), Factors in the Mechanical Failure of the Femoral Component in Total Hip Prosthesis, *Acta Orthop Scandinavica*, 45(5), 693-710.
13. **Mollan R. A. B., Watters P. H., Steele R., McClelland C. J.** (1984), Failure of the femoral component in the Howse total hip arthroplasty, *C/in Orthop*, 190, 142-7.
14. **Petch N. J**. (1953), The cleavadge strength of policrystalls, *JISi*, 174, 25-28.
15. **Roffey P.** (2012), Case study: Failure of a high nitrogen stainless steel femoral stem, Engineering Failure Analysis, Vol. 20, 173-182.
16. **Scheerlinck T, Druyts P, Casteleyn P**. (2004), The use of primary total hip arthroplasty in university hospitals of the European Union, *Acta Orthop Belg*, 70(3), 231-9.
17. **Sen R. K., Mootha A. K., Saini R., Kumar V**. (2009) Segmental Fracture Of A Cemented Femoral Stem - A Case Report And Review Of Litrature, *The Internet Journal of Orthopedic Surgery*, Vol. 13 (1), 13-15.
18. ***Standard Specification for Wrought Nitrogen Strengthened 21 Chromium-10 Nickel-3 Manganese-2.5 Molybdenum Stainless Steel Alloy Bar for Surgical Implants***, American Society for Testing and Materials, Materals, West Conshohocken, PA, ASTM F1586.
19. **Wilson L. F., Nolan J. F., Wood-Waddington M. B.** (1992), Fracture of the femoral stem of the ring TCH hip prosthesis, J Bone Joint Surg Br, 74(5), 725-8.

THE DIAGNOSTIC SYSTEM OF A – 604 AUTOMATIC TRANSMISSION

Jaroslaw CZABAN*, **Dariusz SZPICA***

*Faculty of Mechanical Engineering, Department of Mechanical Engineering, Bialystok University of Technology,
ul. Wiejska 45C, 15 – 351 Białystok, Poland

j.czaban@pb.edu.pl, d.szpica@pb.edu.pl

Abstract: Automatic gearbox gains increasing popularity in Europe. Little interest in diagnosis of such type of transmission in Poland results from the fact of small share in the whole market of operated cars, so there is a lack of availability of special diagnostic devices. These factors cause issues of expensive repairs, often involving a replacement of subassembly to new or aftermarket one. To a small extent some prophylactic diagnostic tests are conducted, which can eliminate future gearbox system failures. In the paper, the proposition of diagnostic system of popular A – 604 gearbox was presented. The authors are seeking for the possibility of using such type of devices to functional elaboration of gearboxes after renovation. The built system pursues the drive of the researched object, connected with simulated load, where special controller, replacing the original one, is responsible for controlling gearbox operation. This way is used to evaluate the mechanic and hydraulic parts' state. Analysis of signal runs, registered during measurements lets conclude about operation correctness, where as comparison with stock data verifies the technical state of an automatic gearbox.

Key words: Automatic Transmission, Diagnosis, Research

1. INTRODUCTION

An automatic transmission is the car gearbox which shifts gears with the change of load and rotational speed of the car engine, releasing the driver from the necessity of manual shifts. This allows very smooth ride, by optimizing the load to the engine rotational speed. Thus the cars equipped with such type of gearbox reach higher mileages, because the engine is less loaded. The automatic transmission is the most popular in the United States of America, but it gains popularity also in Europe. It is estimated that the share of vehicles with automatic gearbox in the American market is ca. 90%, whereas in Europe it is only 27% (including continuously variable transmissions, semi – automatic and double – clutch gearboxes) (Ślaski, 2010). Even smaller popularity in Poland is due to increased fuel consumption, significant operation costs and eventual repair and higher price of vehicles equipped with automatic gearbox.

In last past years the significant technical development occurred in the field of electronics and control systems, which also got into automatic transmission control systems (Bosch, 2005). Electronic control of these systems significantly simplified the hydraulic block (divider) design and allowed to diagnose the technical state of transmission by means of OBDII/EOBD socket and code readings from the P07xx group (Sobieraj, 2005; Merkisz et al., 2006). Small interest in diagnosis of such transmission type results from the fact of small share in the whole market of operated cars, so there is a lack of availability of special diagnostic devices in Poland. These factors cause issues of expensive repairs, often involving a replacement of subassembly to new or aftermarket one. This situation takes place also in dealer service garages. To a small extent some prophylactic diagnostic tests are conducted, which can eliminate future gearbox system failures.

In spite of the electronics development, the automatic gearbox still remained complex mechanical and diagnostic object and is characterized by complexity of processes performing inside it. As its basic assemblies – converter, planetary gearings, clutches and brakes, hydraulic block, solenoid valves and control system with sensors can be counted. These subsystems can be subjected to failures making it completely impossible for transmission to work or causing its improper operation. The basic assemblies failures are: damage of the fluid coupling (converter), wear of clutches or brakes realizing proper gearings, galling and leaks in valve body, solenoid valve or sensor failures or even the controller failures (Chrysler, Sobieraj, 2005). Accurate diagnose of failures and technical state of automatic gearbox significantly reduces repair time and cost.

As an aim, the elaboration of diagnostic stand of automatic transmission after major renovation was stated. The built system enables drive and load application on researched object, with simultaneous controlling its working parameters via special controller, which replaces the original one. The stand can meet broad usage in plants dealing with renovation of automatic gearboxes.

2. THE DIAGNOSTIC TESTING METHODS OF AUTOMATIC GEARBOXES OPERATION

Already in construction and preliminary research course of automatic transmission there are many factors taken into account, which can influence on powertrain functioning. Multi – surface optimization must reconcile the performance with the riding comfort and, what is recently very important – with ecology of the powertrain (Bemporad et al., 2003). The simulation research allows setting the preliminary automatic transmission configuration (Haj – Fraj et al., 2001), the problem is to optimize the control algorithm. For a few years there are available on the market classic gearboxes eqiupped with double clutches, which are able to shift in automatic cycle (Walker et al., 2001), however also in this

case the biggest challenge is the control algorithm. Automatic gearbox and mechanical gearbox with double clutch have one thing in common – synchronization of clutches operation (Wen – Miin et al., 2011). The transition process connected to gear shift decides about dynamic characteristics, as well as operational capabilities (Kulkarni et al., 2007).

There are many methods which form the basis to verify the transmission operational state. The part of them bases on the sensors mounted inside the gearbox and basing on them the functioning is evaluated (Remond et all, 1998), pointing at failure source in the sensors themselves. The other group of methods is the spectral analysis of vibrations generated by powertrain (Rumble et al., 2000), where by using the signal processing the gearing parameters are optimized (Bozca, 2010). The transmission durability is also predicted by estimation of bearing capacity (Ognjanovic et al., 2013).

The research stands elaborating operational capabilities of gearboxes are produced in different configurations. Basic solutions provide the diagnostic sets dedicated to the workshops dealing with repairs (Power Test, Superflow, Mustangdyne, Klotz), the second group consists of research stands, which are used by vehicle producers, for example Adigitec, whereas to the group of the most advanced solutions can be counted The FEV Group solution. The operation of all of these stands is similar, in every case there is necessary to propel the transmission input shaft, while on the other side to brake on the output shaft to generate the torque inside the researched object. The stands based on specific transmission model are also made, in which the internal combustion engine is used for propelling (Ślaski et al., 2011; Ślaski, 2010; Ślaski, 2012). Such type of solutions reflects the real conditions at the highest level, because the transmission is subjected to the variable loads. They are the result of power unit work periodicity. The problem is the universality, i.e. the ability of usage to the other testing object.

3. A – 604 AUTOMATIC GEARBOX

Automatic gearbox A – 604 made in the USA was mounted in Chrysler vehicles since 90s till present day. It was the equipment of cars with engines with the displacement 2.5 to 3.8 L. Depending on the engine displacement the A – 604 gearboxes had small differences in mounting points.

Automatic gearboxes A – 604 as first, according to producer's information, were equipped with adaptive control system, which by reading the throttle position data and vehicle speed, was selecting the gearing. The gearing selection is performed by solenoid valves operation, which control the hydraulic actuating system. The scheme of A – 604 automatic transmission was presented in Fig. 1. The specific construction of exact gearbox subsystems can be found in Chrysler's Automatic Transmission Service Group documentation.

The A – 604 gearbox has four forward gears and one reverse gear. The selector range can be positioned in five positions: P, R, N, D, L. The D range is used for daily driving. The L range is used for driving in mountain and sinuous roads, because it allows the engine braking. In the case of these two positions, for better transmission oil cooling, the lock – up engage occurs.

The selection of clutches is performed by the solenoid valve block controlled by the electric signal. In table 2 the powering states of solenoid valves for individual gearing are presented.

The transition of state and the time of pressure increase in clutches is the coupling time.
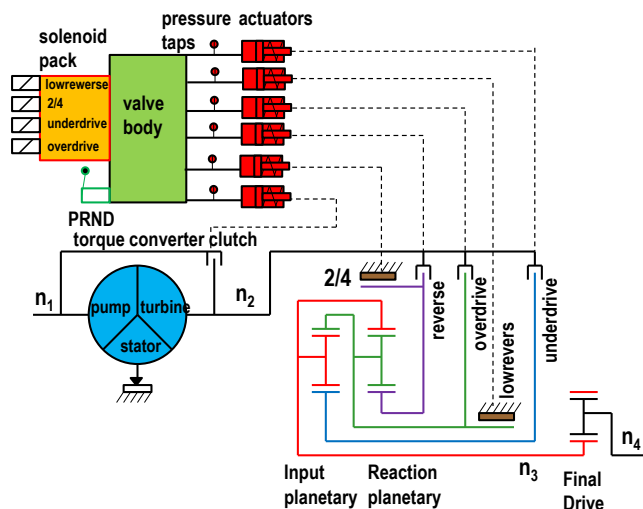

Fig. 1. A – 604 automatic gearbox scheme

The gearing change performs by means of established cooperation of individual clutches. In Tab. 1 the list of engaged clutches depending on the selected gearing are presented.

Tab. 1. Kinds of cooperating clutches depending on gearing (Chrysler)

Transsmision operation state	Clutch				
	Under drive	Overdrive	Reverse	2/4	Low reverse
Park					X
Reverse			X		X
Neutral					X
1st	X				X
2nd	X			X	
3rd	X	X			
4th		X		X	

Tab. 2. Solenoid valve states for individual gearings (Chrysler)

Transmission operation state	Solenoid valve			
	Lowreverse	2/4	Underdrive	Overdrive
Park	X	X		
Neutral		X		
Reverse				
1st	X	X		
2nd				
3rd		X		X
3rd+ lockup	X	X		X
4th			X	X
4th+ lockup	X		X	X

The oil pressure in clutches actuators: lowreverse, overdrive and 2/4, of automatic gearbox is continuously monitored by the gearbox controller by means of pressure sensors in solenoid valve block. Below the sensor states for individual gearings are presented (Tab. 3).

Tab. 3. Sensor states for individual gearings (Chrysler)

Transmission operation state	Lowreverse	2/4	Overdrive
Park	1	0	0
Reverse	0	0	0
Neutral	1	0	0
1st	1	0	0
2nd	0	1	0
3rd	0	0	1
4th	0	1	1

The „zero" state means no pressure in individual clutch (no electrical signal). Whereas „one" means the specific pressure value (voltage).The pressure measurement can also be performed by pressure ports available in gearbox housing.

The gearbox controller is responsible for control of transmission operation. This device is coupled with engine control unit. The controller, basing on the range selector position, measured driving speed, engine rotational speed and converter's slip, engaged proper gear by energizing individual solenoid valves and by means of internal binary sensors of solenoid valve package checked if the pressure values occur in proper ports.

4. TEST STAND FOR AUTOMATIC GEARBOX A – 604

For estimating the technical state of automatic gearbox A – 604 in Department of Construction and Operation of Machines the research stand was designed, which is showed in Fig. 2.
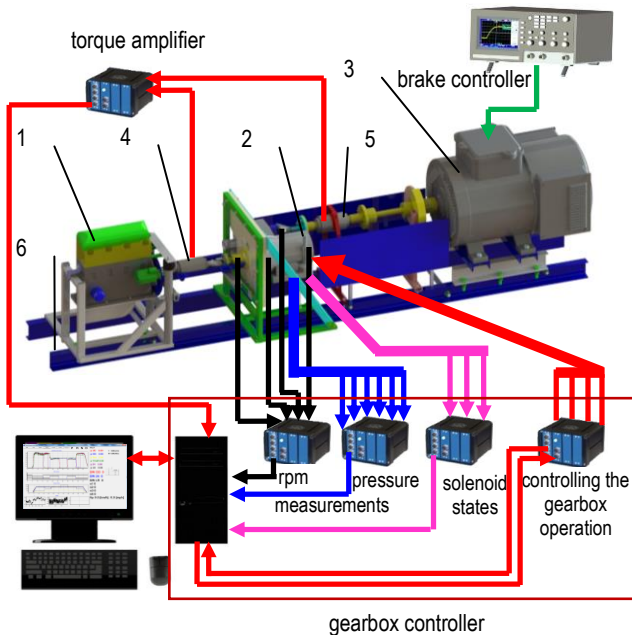

Fig. 2. Test stand for A – 604 automatic gearbox testing:
1 – propeller system, 2 – automatic transmission system,
3 – DC generator, 4, 5 – coupling shafts and torque sensors,
6 – stand frame

It consists of automatic gearbox assembly (2) mounted to the frame (6). For propelling the gearbox the XUD – 9 diesel internal combustion engine (1) was used, whereas for braking – DC generator (3). Propelling and load, which affect the gearbox, are transmitted by shafts and torque sensors (4,5). The modular

construction of the stand allows changing the propeller to electrical engine controlled by inverter, as well as dismantling the braking system.

To allow gear shifting in automatic gearbox and measurement data acquisition the specialized diagnostic controller was made, which is based on AtMega32 microcontroller. The block scheme of the controller is showed in Fig. 3. It consists of input module, to which the rotational speed sensors (7) are connected. They allow determining the engine rotational speed n_1, converter output speed n_2, planetary gearing assembly output speed n_3 and half – shaft rotational speed n_4. Three solenoid valve block pressure sensors (9) were also connected to the module, as well as six pressure sensors in clutch actuators (11). For determining the position of range selector lever (10) the binary sensors of gearbox were used. The controller, by means of output module, controls the operation of the solenoids of valve block (8). The information about actual controller operation parameters are displayed on LCD screen (6). The gear shift can be performed automatically or manually.
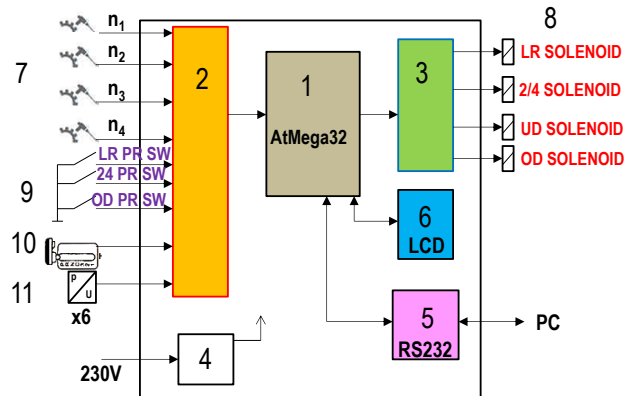

Fig. 3. Block scheme of the gearbox controller:
1 – AtMega32 microcontroller, 2 – input module, 3 – output module, 4 – power supply system, 5 – communication port, 6 – LCD screen, 7 – rotational speed sensors, 8 – solenoid valve block, 9 – solenoid valves pressure sensors, 10 – range selector lever sensor, 11 – pressure sensors inside actuators, (LR – Lowreverse, UD – Underdrive,OD – Overdrive)

For controlling the gearbox operation, measurement data acquisition and visualization the individual computer application "A604.exe" was made in Borland Delphi 3.0 programming environment (Fig. 4).
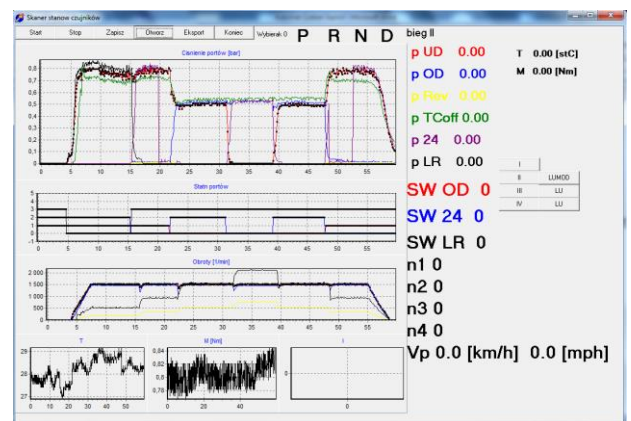

Fig. 4. "A604.exe" application – example of recorded measurement session

The specific description of presented controller, which includes electronic systems schemes and applied algorithms saved in microcontroller, will be presented in next authors' publications.

5. THE PROCEDURE OF DIAGNOSTIC RESEARCH ON THE STAND AND SAMPLE RESULTS

The basic research, which enables the evaluation of mechanic and hydraulic systems operation of the gearbox, is the measurement of pressure values in specific actuators of clutch baskets and comparing them with nominal values given by producer (Tab. 4). The pressure courses also enable the evaluation of gearing changing process. To perform the evaluation, the research must be run for every possible operation modes of the automatic transmission and ensure proper rotational speed values for each of these modes. For correct conclusion about changing gearings, the research should be run both ways: increasing and decreasing.

The test was run on the gearbox after the major repair, which came from Chrysler Voyager with mileage ca. 160k km. In this gearbox the lowreverse clutch was replaced because of its crack. Taking into account the significant vehicle mileage, all clutch disc set and inner seals were also replaced.

In the test the electrical motor was used instead of internal combustion engine and the test under load was skipped. It was a result of the fact that it was necessary to lock up the differential., because the gearbox came from the vehicle with integrated drive assembly. The stand is dedicated to test the gearboxes from cars with classical drive assembly.

The test was run in accordance to producer's recommendation in oil temperature ca. 80 ºC and recommended vehicle longitudinal speeds on individual gearings. Rotational speeds with which the gearbox was propelled during research in selector positions P, R and N was set to 1500 rpm.

Basing on the registered pressure courses in individual clutches actuators the average values of pressure during operation on individual gearings were stated. Gained results were set in Tab. 4. The values were within the ranges given by the producer.

During tests of researched gearbox, gearing changing was performed in robust way both directions: up and down. No differences were observed in time values of engaging specific gears. The research in 4th gear and with lockup clutch engaged did not result in any slips, what indicates the proper operation.

It was stated that the major renovation was done correctly and all elements of gearbox: mechanic and hydraulic ones, work properly and it can be mounted in the vehicle.

Tab. 4. Comparison of measured pressures with the producer's data (* Chrysler)

Selector range	Transmission control state	Pressure in clutch actuators [MPa]					
		Underdrive	Overdrive	Reverse	Lockup off	2/4	Lowreverse
P	P	**0.00** (0 ÷ 0.014) *	**0.00** (0 ÷ 0.034) *	**0.00** (0 ÷ 0.014) *	**0.492** (0.414 ÷ 0.758) *	**0.00** (0 ÷ 0.014) *	**0.832** (0.793 ÷ 0.99) *
R	R	**0.00** (0 ÷ 0.014) *	**0.00** (0 ÷ 0.048) *	**1.195** (1.14 ÷ 1.61) *	**0.645** (0.345 ÷ 0.689) *	**0.00** (0 ÷ 0.014) *	**1.148** (1.14 ÷ 1.61) *
N	N	**0.00** (0 ÷ 0.014) *	**0.00** (0 ÷ 0.034) *	**0.00** (0 ÷ 0.014) *	**0.621** (0.4137 ÷ 0.758) *	**0.00** (0 ÷ 0.014) *	**0.878** (0.793 ÷ 0.99) *
D 28 km/h	1st	**0.809** (0.758 ÷ 0.99) *	**0.00** (0 ÷ 0.034) *	**0.00** (0 ÷ 0.014) *	**0.633** (0.4137 ÷ 0.758) *	**0.00** (0 ÷ 0.014) *	**0.879** (0.793 ÷ 0.99) *
D 56 km/h	2nd	**0.832** (0.758 ÷ 0.99) *	**0.00** (0 ÷ 0.034) *	**0.00** (0 ÷ 0.014) *	**0.656** (0.4137 ÷ 0.758) *	**0.855** (0.793 ÷ 0.99) *	**0.00** (0 ÷ 0.014) *
D 80 km/h	3rd	**0.516** (0.517 ÷ 0.65) *	**0.527** (0.517 ÷ 0.65) *	**0.00** (0 ÷ 0.014) *	**0.551** (0.4137 ÷ 0.62) *	**0.00** (0 ÷ 0.014) *	**0.00** (0 ÷ 0.014) *
D 112 km/h	4th	**0.00** (0 ÷ 0.014) *	**0.539** (0.517 ÷ 0.65) *	**0.00** (0 ÷ 0.014) *	**0.551** (0.4137 ÷ 0.62) *	**0.539** (0.517 ÷ 0.65) *	**0.00** (0 ÷ 0.014) *
D 126 km/h	4th+ lockup	**0.00** (0 ÷ 0.014) *	**0.527** (0.517 ÷ 0.65) *	**0.00** (0 ÷ 0.014) *	**0.00** (0 ÷ 0.034) *	**0.539** (0.517 ÷ 0.65) *	**0.00** (0 ÷ 0.014) *

6. SUMMARY

The built stand lets evaluate the automatic gearboxes operation, mainly in terms of mechanic and hydraulic systems, using in controlling the own acting system. Possible measurements and tests to perform:
- shifting gears in automatic or manual mode,
- correctness of gearbox operation with cold or hot oil,
- leak tightness of executing elements of hydraulic steering system,
- correctness of oil pump operation – oil pressing test,
- elaboration of operation loudness: fluid coupling, pump, clutches or planetary gear systems,
- correctness of operation at established, constant gearbox operation parameters,
- test checking the solenoid valves operation, fluid coupling (lock – up engaging),
- measurement of operation oil temerature,
- measurement of output rotational speed on output transmission shaft on each gearing,
- measurement of torque on transmission input and output shaft.

The built stand can be used for research purposes, as well as the base for mathematical models verification, describing the researched system operation. It is also possible to use it in gearbox diagnosis after the repair, before mounting in the vehicle. Given results are presented in graphic form or as the data stored in tables, depending on individual needs of person who diagnoses the gearbox. The stand can be fitted to individual needs of every service or workshop.

REFERENCES

1. *Automatic Transmission Service Group: Introduction: Chrysler A – 604*, Florida 1994 – 2005.
2. **Bemporad A., Borodani P., Mannelli M.** (2003), Hybrid control of an automotive robotized gearbox for reduction of consumptions and emissions, 6th International Workshop on Hybrid Systems – Computation and Control (HSCC 2003), Prague, Czech Republic, Apr 03 – 05, Edited by: Maler O., Pnueli A., *Hybrid systems: Computation and control proceedings*, Vol. 2623, 81 – 96.
3. **Bosch Folders** (2005), *Elektronic steering of EGS gearbox*, WKL, Warsaw
4. **Bozca M.** (2010), Torsional vibration model based optimization of gearbox geometric design parameters to reduce rattle noise in an automotive transmission, *Mechanism and Machine Theory*, Vol. 45, 1583–1598.
5. **Haj – Fraj A., Pfeiffer F.** (2001), Optimal control of gear shift operations in automatic transmissions, *Journal of the Franklin Institute*, Vol. 338, 371–390.
6. Advanced Digital Technology Co. Ltd. (2014), http://adigitec.com/ data/ADT%20Brochure%20130215%20Light%20version.pdf.
7. FEV GmbH(2014), http://www.fev.com/fileadmin/fev–resources/ TecInfo/Test_System/173_TecInfo_FEV_Transmission_Test _Bench.pdf.
8. Klotz GmbH (2014), http://www.klotz.de/en/measurement_testing/ automatic_transmissions.html.
9. Mustang Advanced Engineering (2014), http://www.mustangdyne. com/mustangae/wp – content/uploads/downloads/2011/03/MAE – transmission2012.pdf.
10. International Corporate Headquarters, Power Test, Inc. (2014), http://www.pwrtst.com/transmission/test – stand.htm#.
11. SuperFlow Dynamometers & Flowbenches(2014), http://www.superflow.com/Dynamometers/transmission/edect.php.
12. **Kulkarni M., Shim T., Zhang Y.** (2007), Shift dynamics and control of dual – clutch transmissions, *Mechanism and Machine Theory*, Vol. 42, 168–182
13. **Merkisz J., Mazurek S.** (2006), *OBDII EOBD On – board diagnostics*, WKL, Warszawa.
14. **Ognjanovic M., Milutinovic M.** (2013), Design for Reliability Based Methodology for Automotive Gearbox Load Capacity Identification, *Strojniški vestnik – Journal of Mechanical Engineering*, Vol. 59/5, 311 – 322.
15. **Remond D., Soleilhac P., Play D., Coppens P., Villars F.** (1998), Transmission error measurements on automotive gearbox, *Mechanique Inustielle et ma Materiaux*, Vol. 51/2, 61 – 63.
16. **Rumble A. W.** (2000), Techniques for enhancing correlation between objective tonal noise measurements from automotive transmissions on test stands and subjective assessments in – vehicle, IMECHE – Vehicle Noise and Vibration, Vol. 2000/1, 127 – 137.
17. **Ślaski G.** (2010), Savings the fuels due to modern solutions in automatic gearboxes, *InterdisciplinaryScientific Conference Ecological and Energetic Threats and New Challenges materials,* PWSZ, Gniezno, 64 – 74.
18. **Ślaski G.** (2012), The purposefulness of application and control issues of friction brake within test bench simulation reproducing the drivetrain dynamics, *The Archives of Automotive Engineering*, 4/58, 57 – 66
19. **Ślaski G., Walkowiak J.** (2011), Test bench simulation reproducing the drivetrain dynamics of a car with automatic transmission – control and results of experimental tests, *The Archives of Automotive Engineering*, 3/53, 61 – 80.
20. **Sobieraj W.** (2005), Automatic gearboxes, *Instalator Polski*, 4.
21. **Walker P. D., Zhang N., Tamba R.** (2011), Control of gear shifts in dual clutch transmission powertrains, *Mechanical Systems and Signal Processing*, Vol. 25, 1923–1936
22. **Wen – Miin H., Yu – Lien H.** (2011), Connecting clutch elements to planetary gear trains for automotive automatic transmissions via coded sketches, *Mechanism and Machine Theory*, Vol 46, 44–52.

EFFECT OF PLASMA NITRIDING PROCESS CONDITIONS ON CORROSION RESISTANCE OF 440B MARTENSITIC STAINLESS STEEL

Magdalena ŁĘPICKA[*], **Małgorzata GRĄDZKA-DAHLKE**[*]

[*]Faculty of Mechanical Engineering, Department of Materials and Biomedical Engineering, Bialystok University of Technology,
ul. Wiejska 45 C, 15-351 Białystok, Poland

magdalena.lepicka@gmail.com, m.dahlke@pb.edu.pl

Abstract: Martensitic stainless steels are used in a large number of various industrial applications, e.g. molds for plastic injections and glass moldings, automotive components, cutting tools, surgical and dental instruments. The improvement of their tribological and corrosion properties is a problem of high interest especially in medical applications, where patient safety becomes a priority. The paper covers findings from plasma nitrided AISI 440B (PN-EN or DIN X90CrMoV18) stainless steel corrosion resistance studies. Conventionally heat treated and plasma nitrided in N_2:H_2 reaction gas mixture (50:50, 65:35 and 80:20, respectively) in two different temperature ranges (380 or 450°C) specimens groups were examined. Microscopic observations and electrochemical corrosion tests were performed using a variety of analytical techniques. As obtained findings show, plasma nitriding of AISI 440B stainless steel, regardless of the process temperature, results in reduction of corrosion current density. Nevertheless, applying thermo-chemical process which requires exceeding temperature of about 400°C is not recommended due to increased risk of steel sensitization to intergranular and stress corrosion. According to the results, material ion nitrided in 450°C underwent leaching corrosion processes, which led to significant disproportion in chemical composition of the corroded and corrosion-free areas. The authors suggest further research into corrosion process of plasma nitrided materials and its degradation products.

Key words: Stainless Steels, Corrosion, Surface Modification Techniques, Plasma Nitriding, Surgical Instruments

1. INTRODUCTION

The improvement of performance of martensitic stainless steels is a problem of high interest. Martensitic stainless steels are used in a large number of various industrial applications, e.g. molds for plastic injections and glass moldings, automotive components, cutting tools, surgical and dental instruments (Pinedo and Monteiro, 2004; Wu, et al., 2010). The improvement of their tribological and corrosion properties is a problem of high interest especially in medical applications. Necessity to undergo cyclical sterilisation processes and intermittent contact with hard tissues and body fluids (Marciniak, 1992; Paszenda and Tyrlik-Held, 2003) create unusually hard working conditions. Due to that reassurance of patient safety becomes a priority for medical instruments manufacturers.

Plasma nitriding, also referred to as ion nitriding, is a thermo-chemical surface treatment used in industry for more than 30 years (Soltani Asadi and Mahboubi, 2012) to treat especially steels. Its main aim is to introduce elemental nitrogen to the surface of a metal part for subsequent diffusion into the material (Sirin and Kaluc, 2012; Mashreghi et al., 2013). As a result, nitrogen-rich phases form at the steel's surface (Basu et al., 2008) - a compound, "white" layer and a diffusion zone (Sirin and Kaluc, 2012; Mashreghi et al., 2013). The outer and considerably thinner layer (usually ca. 25 µ thick) (Podgornik et al., 1998) consists of γ'-Fe_4N or ε-$Fe_{2,3}$N inter-metallic phases (Sirin and Kaluc, 2012; Mashreghi et al., 2013). It is commonly called as "white layer" due to its white colour after Nital etch on the mictoscopy or, simply, referred to as "compound layer" (Sirin and Kaluc, 2012). On the other hand, the diffusion zone consists of a nitrogen rich solid solution and fine coherent nitride precipitates (Sirin and Kaluc, 2012; Mashreghi et al., 2013). The studies have shown that both γ'-Fe_4N or ε-$Fe_{2,3}$N are characterised by excellent tribological characteristics and good corrosion properties (Li and Bell, 2008; Xi et al., 2008a; Xi et al., 2008b; Zhao et al., 2012; Mashreghi et al., 2013). Their proportion in the nitride-affected layer depends upon the plasma activity, treatment duration, microstructure of the sample and its temperature (Tuckart et al., 2007). Although the compound layer has a relatively high hardness of 950-1200 HV, the high internal stresses between the various lattice structures make it brittle, which can lead to spalling during service (Podgornik et al.,1998). Tuckart et al. (Tuckart et al., 2007) have shown that after some incubation time, even without any external disturbance, cracks are generated and propagate in the nitride layers.

In the previous work (Łępicka and Grądzka-Dahlke, 2013), the effect of heat treatment and plasma nitriding on the corrosion resistance of AISI 440B martensitic stainless steel has been investigated. The results showed that plasma nitriding does not significantly affect AISI 440B martensitic stainless steel corrosive characteristics as far as the uniform nitride layer over the entire detail surface is obtained. Therefore, in this study the effects of plasma nitriding in various nitrogen to hydrogen ratios on the corrosion resistance of AISI 440B martensitic stainless steel have been evaluated.

2. MATERIALS AND METHODS

As in the previous research (Łępicka and Grądzka-Dahlke, 2013), the AISI 440B (PN-EN X90CrMoV18) stainless steel was

selected for further analyses. Chemical composition of the substrate is presented in Tab. 1.

Tab. 1. 440B stainless steel chemical compotision (wt%)

	C	Mn	Si	S	P
EDX	n/o	0.74	0.84	-	0.03
PN-EN 10088 -1:2005	0.85 ÷0.95	max 1.00	max 1.00	max 0.040	max 0.030
	Cr	**Mo**	**V**	**Fe**	
EDX	19.25	0.98	0.09	balance	
PN-EN 10088 -1:2005	17.00 ÷19.00	0.90 ÷1.30	0.07 ÷0.12	balance	

The research material has been prepared accordingly to the manufacturing process of surgical drill bits. Specimens were heat treated and plasma nitrided. The effect of plasma nitriding conditions on subjected material corrosion resistance has been investigated.

Specimens were subjected to heat treatment, consisting of quenching in oil, from an austenitising temperature of 1030°C, and tempering. The tempering temperature is extremely important when considering desired properties of the steel. Tempering in low temperatures (up to 250°C) provides the highest hardness. However, the following procedure, plasma nitriding, is performed at higher temperatures.

Specimens were prepared in the form of discs with 8 mm diameter and 6 mm height. Pre-cut material was subjected to two-phase heat treatment: quenching in oil, from austenitising temperature of 1030°C, and tempering in 250°C. The substrate material has been finished by means of sandblasting, what is typical for surgical instruments manufacturing process.

The as-received samples were divided into 7 groups and subjected to 6 plasma nitriding processes, differing in the process temperature and working gases concentrations. The plasma nitriding process was carried out at 380 or 450°C temperature, under the working pressure of 200 Pa. The nitriding process, as earlier, lasted 2 hours. In order to determine the most promising treatment conditions, the authors chose three concentrations of working gases, namely:

a) 50% H, 50% N, i.e. 100 ml/min H_2 + 100 ml/min N_2,
b) 65% H, 35% N, i.e. 130 ml/min H_2 + 70 ml/min N_2,
c) 80% H, 20% N, i.e. 160 ml/min H_2 + 40 ml/min N_2.

All analysed samples are summarised in Tab. 2. The reference material was non-treated AISI 440B martensitic stainless steel (Tab. 2, series 7).

The obtained materials corrosive characteristics were demarcated using computer controlled ATLAS 9833 (Atlas-Sollich) corrosion system. Potentiodynamic polarisation scans with constant scan rate of 0.001 V/s were performed in open to air, maintained at 21°C 0.9 wt% $NaCl_{aq}$ solution. The electrode set consisted of a saturated calomel electrode (SCE, 0.242 V in 25°C vs SHE at 25°C), platinum auxiliary electrode (31.4 mm² contact surface) and a AISI 440B martensitic stainless steel sample, which circular area of 50.24 mm2 contacted with the testing solution. Tests were performed as follows: (I) cleansing sample from debris in filled with ethyl alcohol bath ultrasonic cleaner, (II) rinsing metallic specimen with distilled water, (III) placing the prepared sample in a three-neck flask pre-filled with 250 cm³ 0.9% $NaCl_{aq}$ solution, (IV) stabilization for 120 minutes, (V) performance of polarisation scan from -0.6 V to potential of up to +2 V. The corrosion potential (E_{corr}), corrosion current logarithm (log i_{corr})

(Tafel method) and the pitting potential (E_p) were determined.

Tab. 2. Specimens summary table

Series no.	Plasma nitriding process temperature (°C)	Gaseous mixture concentration
1	380	50% N_2 + 50% H_2
2		35% N_2 + 65% H_2
3		20% N_2 + 80% H_2
4	450	50% N_2 + 50% H_2
5		35% N_2 + 65% H_2
6		20% N_2 + 80% H_2
7	Reference sample	Without modification

The post-test samples pit and morphology structure were studied by scanning electron microscopy (SEM – Hitachi S-3000N microscope), confocal laser scanning microscopy (CLSMO – Olympus LEXT OLS 4000 microscope) and energy-dispersive X-ray analyser (EDX).

3. RESULTS AND DISCUSSION

The applied thermo chemical treatment parameters resulted in a change in the corrosion resistance of tested steels, as shown in Figs. 1-6.

The first group of investigated samples consisted of specimens plasma nitrided at temperatures in the range of 380°C (Fig. 1). First and foremost, it can be observed that the reactive gas composition has a minor impact on corrosion characteristics; curves which present ion nitrided material almost overlap. It is vital that regardless of the reaction gas mixture, with respect to the non-nitrided specimen, the corrosion potential of plasma nitrided material shifts towards the less noble values. However, the corrosion currents of modified samples is about twice lower. What is more, pitting potential ($E_p \approx 1$ V for series 2 and series 3) is observed only for samples ion nitrided in low-nitride gas mixture.

A similar trend can be observed considering steel plasma nitrided in higher temperatures (Figure 2). As in the previous case, the corrosion currents of modified specimens are significantly lower than the one of the reference material. The lower the corrosion current is, the lower the corrosion rate of the considered material occurs. However, pitting potential can be noticed for both modified specimens at the potential of ca. 900 mV. As it was mentioned in the previous work (Łępicka and Grądzka-Dahlke, 2013), heat treatment of martensitic stainless steels in temperatures exceeding 420°C may lead to deterioration of their corrosion characteristics. For that reason, the low-temperature (LTN) plasma nitriding ought be suggested in mass production rather than the high-temperature one.

As it can be seen in Fig. 3, the reference material is distinguished by the most positive corrosion potential, and, at the same time, the highest corrosion rate of all considered samples. The plasma nitriding process, irrespective of the reactive gas composition, results in reduction of the corrosion processes rate. The best results are obtained when using the low-temperature process. Clearly, this kind of surface modification has its drawbacks, emerging mainly from the difficulties connected with designing the high-effective mass production process, but its advantages stand out among all demerits. The main one is ability to obtain

improvement in corrosion characteristics without sacrificing hardness of the modified detail. It is an extremely important factor when considering thermo-chemicall process application in surgical drill bits production. The operational part of that type of surgical tools ought be characterised mainly by high hardness and adequate wear resistance.
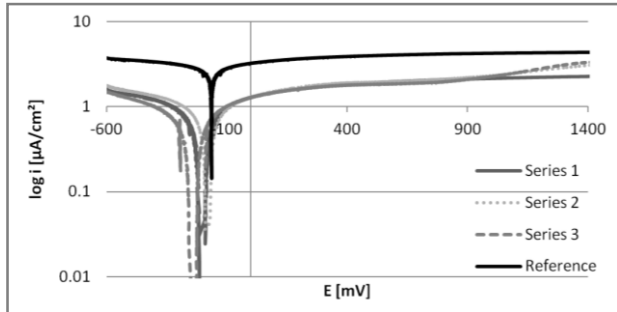

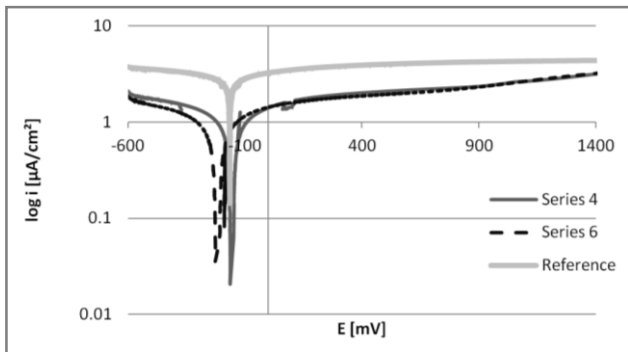**Fig. 1.** Polarisation curves of plasma nitrided in 380°C 440B steel in 0.9 wt% NaCl solution (undeaerated, unstirred)

Fig. 2. Polarisation curves of plasma nitrided in 450°C 440B steel in 0.9 wt% NaCl solution (undeaerated, unstirred)
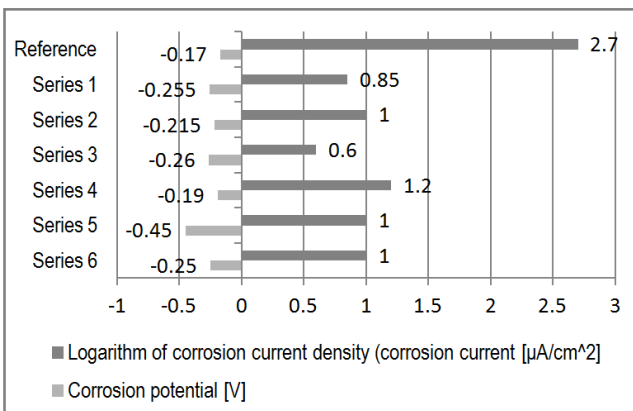

Fig. 3. Selected corrosion potentials and logarithms of corrosion currents densities of the examined samples

Fig. 4 presents surface morphology of the reference sample after potentiodynamic test. As it can be seen, even at the magnification of 1000× no corrosion pits can be distinguished – only traces of machining are visible. Chemical composition of the specimen, mesured by the means of EDX, covers the chemical composition of ISO standard AISI 440B martensitic stainless steel.
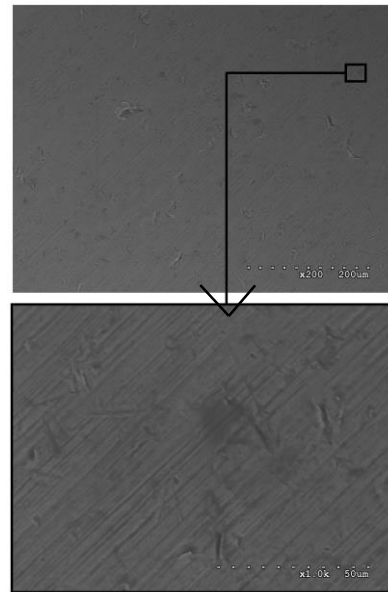

Fig. 4. Surface morphology of the reference material. SEM images, 200 and 1000× magnification
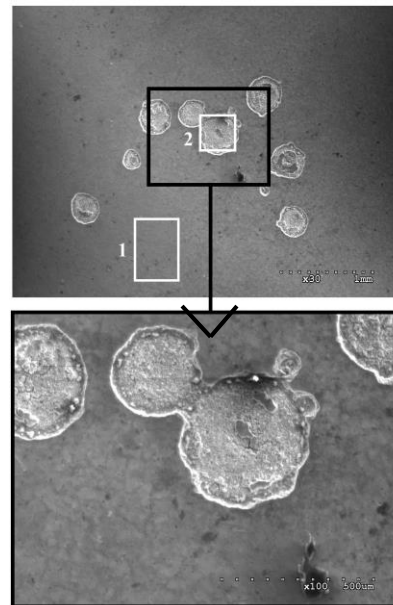
Fig. 5. Series 4 sample after potentiodynamic test. SEM images, 30 and 100× magnification; 1 – non-corroded surrounding material, 2 – pit area

Tab. 3. Chemical composition of areas presented in Fig. 5 (wt%)

	C	Mn	Si	S	P
Area no. 1	n/o	0.77	0.96	-	0.04
Area no. 2	n/o	1.05	0.49	-	0.02
	Cr	Mo	V	Fe	
Area no. 1	19.55	1.10	0.07	77.52	
Area no. 2	45.21	2.50	0.17	50.56	

Plasma nitrided specimens surface morphology significantly differs from the reference one. First and foremost, corrosion pits of circular shape are visible even with the unaided eye (Fig. 5). Surface condition suggests that, as opposed to the reference

material, uniform corrosion processes were not present. What is more, the corrosion pits areas are chromium-rich and low in iron (Tab. 3). This suggests selective dissolution of alloying elements. This phenomenon can occur e.g. when chromium carbides are present in a stainless steel alloy. In such case, the adjacent to the carbides, low in chromium areas become the anodic, highly susceptible to corrosion processes regions. High disproportion between the anode and cathode areas size and quantity leads to dynamic material dissolution at the grain boundaries (Łępicka and Grądzka-Dahlke, 2013). Next possible scenario assumes that the material reached its pitting potential, as it was mentioned before. Continuity of obtained in the thermo-chemical process nitride layer was broken, leading to a rapid iron dissolution. Corrosion pits gradually increased in size and depth, causing the observed damages visibility.
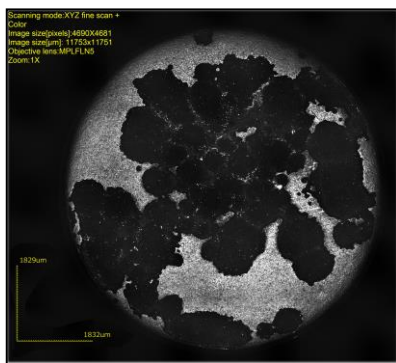

Fig. 6. Series 5 sample after potentiodynamic test. CLSMO image.

What is important, such disproportions in chemical composition were observed only for material ion nitrided in 450°C (Series 4-6). Knowing that the higher temperature of the thermal process is, the bigger is the risk of making martensitic stainless steel susceptible to intergranular corrosion, this finding suggests that chromium carbides were highly likely to precipitate. If indeed so, selective leaching, often referred to dealloying or selective corrosion, occured.

Similar findings were obtained for other series nitrided in 450°C. Fig. 6 presents macroscopic view of series 5 sample. Depth of the corrosion pits, measured by the means of CLSMO microscope, reached up to 7 μm.

4. SUMMARY

The aim of the conducted study was to evaluate corrosion resistance of 440B type martensitic stainless steel after plasma nitriding in two different process temperatures. According to the literature, ion nitriding in 380°C is recommended in manufacturing process rather than plasma nitriding in higher temperatures due to increased likelihood of fatigue and stress corrosion occurrence after applying thermo-chemical process in temperatures exceeding 400°C. Received research results confirm these theses.

The obtained findings analysis enabled authors to draw following conclusions:

- With regard to the reference material, plasma nitriding results in reduction of corrosion current density, that is it helps reducing corrosion processes rate.
- The lower nitrogen ratio in the gaseous mixture is, the better anticorrosive properties material exhibits.

- Further analysis into corrosion processes and degradation products of plasma nitrided material is suggested.

REFERENCES

1. **Basu A., Dutta Majumdar J., Alphonsa J., Mukherjee S., Manna I.** (2008), Corrosion resistance improvement of high carbon low alloy steel by plasma nitriding, *Materials Letters*, Vol. 62, No. 17-18, 3117-3120.
2. **Łępicka M., Grądzka-Dahlke M.** (2013), Effect of Heat Treatment and Plasma Nitriding on Corrosion Resistance of X90CrMoV18 Martensitic Stainless Steel, *Acta Mechanica et Automatica*, Vol. 7, No. 3, 155-159.
3. **Li C. X., Bell T.** (2006), Corrosion properties of plasma nitrided AISI 410 martensitic stainless steel in 3.5% NaCl and 1% HCl aqueous solutions, *Corrosion Science,* Vol. 48, No. 8, 2035-2049.
4. **Mashreghi A. R., Soleimani S. M., Saberifar S.** (2013), The investigation of wear and corrosion behavior of plasma nitrided DIN 1.2210 cold work tool steel, *Materials and Design*, Vol. 46, 532-538.
5. **PN-EN 10088-1:2005,** Stainless steels, List of stainless steels.
6. **PN-EN ISO 7153-1:2002,** Surgical instruments, Metallic materials. Stainless steel.
7. **PN-EN ISO 8044:2002,** Corrosion of metals and alloys - Basic terms and definitions.
8. **Podgornik B., Vizintin J., Leskovsek V.** (1998), Tribological properties of plasma and pulse plasma nitrided AISI 4140 steel, *Surface and Coatings Technology*, Vol. 108-109, 454-460.
9. **Sirin S. Y., Kaluc, E.** (2012), Structural surface characterization of ion nitrided AISI 4340 steel, *Materials and Design*, Vol. 36, 741-747.
10. **Soltani Asadi Z., Mahboubi F.** (2012), Effect of component's geometry on the plasma nitriding behavior of AISI 4340 steel, *Materials and Design*, Vol. 34, 516-521.
11. **Tuckart W., Forlerer E., Iurman L.** (2007), Delayed cracking in plasma nitriding of AISI 420 stainless steel, *Surface & Coatings Technology,* Vol. 202, No. 1, 199-202.
12. **Wu K., Liu G. Q., Wang L., Xu B. F.** (2010), Research on new rapid and deep plasma nitriding techniques of AISI 420 martensitic stainless steel, *Vacuum,* Vol. 84, No.6, 870-875.
13. **Xi Y., Liu D., Han D.** (2008a), Improvement of corrosion and wear resistances of AISI 420 martensitic stainless steel using plasma nitriding at low temperature, *Surface & Coatings Technology,* Vol. 202, No. 12, 2577–2583.
14. **Xi Y., Liu D., Han D.** (2008b), Improvement of erosion and erosion–corrosion resistance of AISI420 stainless steel by low temperature plasma nitriding, *Applied Surface Science,* Vol. 254, No. 18, 5953–5958.
15. **Zhao Y., Yu B., Dong L., Du H., Xiao J.** (2012), Low-pressure arc plasma-assisted nitriding of AISI 304 stainless steel, *Surface and Coatings Technology*, Vol. 210, 90-96.

DOUBLY PERIODIC CRACKS IN THE ANISOTROPIC MEDIUM WITH THE ACCOUNT OF CONTACT OF THEIR FACES

Olesya MAKSYMOVYCH*, Iaroslav PASTERNAK*, Heorhiy SULYM**, Serhiy KUTSYK*

*Lutsk National Technical University, Lvivska Str. 75, 43018 Lutsk, Ukraine
**Bialystok Technical University, Wiejska Str. 45C, 15-351 Bialystok, Poland

olesyamax@meta.ua, pasternak@ukrpost.ua, h.sulym@pb.edu.pl, sergosidpr@bigmir.net

Abstract: The paper presents complex variable integral formulae and singular boundary integral equations for doubly periodic cracks in anisotropic elastic medium. It utilizes the numerical solution procedure, which accounts for the contact of crack faces and produce accurate results for SIF evaluation. It is shown that the account of contact effects significantly influence the SIF of doubly periodic curvilinear cracks both for isotropic and anisotropic materials.

Key words: Anisotropic, Doubly Periodic, Singular Integral Equation, Crack

1. INTRODUCTION

The doubly periodic problems are widely considered in scientific literature, since they are crucial for understanding of the effect of cracks interaction on stress state of defective solids (see Sawruk, 1981). Wang (2004) presented extremely accurate and efficient method for computing the interaction of a set or multiple sets of general doubly periodic cracks in elastic medium. Xiao and Jiang (2009) studied the orthotropic medium with doubly periodic cracks of unequal size under antiplane shear. Chen et al. (2003) have studied various multiple crack problems in elasticity. Xiao et al. (2011) obtained the closed-form solution for stress and electric displacement intensity factors and effective properties of piezoelectric materials with a doubly periodic set of conducting rigid line inclusions. Malits (2010) studied the doubly periodic arrays of rigid line inclusions in an elastic solid. Pasternak (2012) presented the general Somigliana integral identities and boundary integral equations for doubly periodic cracks in anisotropic magnetoelectroelastic medium.

However, equations of Pasternak (2012) contain both singular and hypersingular integrals, therefore, this paper is focused on the development of singular integral equation for doubly periodic cracks in anisotropic medium. Also the contact of crack faces is accounted for, thus, the paper presents new general approach that can be used both in theoretical and applied analysis, in particular, in rock mechanics.

2. OBTAINING OF SINGULAR INTEGRAL EQUATIONS BASED ON THE LEKHNITSKII FORMALISM

Consider a doubly periodic problem of elasticity for an infinite anisotropic plate, which representative volume element contains a set of cracks L_j $(j = 1, ..., J)$. Assume that crack faces are symmetrically loaded with tractions (X_T, Y_T) and average stress $\langle \sigma_x \rangle$, $\langle \sigma_y \rangle$, $\langle \sigma_{xy} \rangle$ act in the medium.

2.1. Governing equations for anisotropic plates

Consider an arbitrary curve Γ that lays in the 2D domain D occupied by the plate, and assume its positive path. One can introduce the traction vector $\vec{S}_\Gamma$ in the tangential element of the curve Γ, which normal vector is placed at the right to the chosen positive path of the curve. The projections (X_Γ, Y_Γ) of the traction vector $\vec{S}_\Gamma$ and displacement (u, v) derivatives by the arc coordinate at the curve Γ can be evaluated based on the Lekhnitskii complex functions as (Bozhydarnyk, 1998; Grigolyuk & Filshtinskiy, 1994):

$$Y_\Gamma = -2\text{Re}[\Phi(z_1)z_1' + \Psi(z_2)z_2']$$
$$X_\Gamma = 2\text{Re}[s_1\Phi(z_1)z_1' + s_2\Psi(z_2)z_2']$$
$$u' = 2\text{Re}[p_1\Phi(z_1)z_1' + p_2\Psi(z_2)z_2']$$
$$v' = 2\text{Re}[q_1\Phi(z_1)z_1' + q_2\Psi(z_2)z_2']$$

(1)

where: $z_j = x + s_j y$, $u' = du/ds$, $v' = dv/ds$, $z_j' = dx/ds + s_j dy/ds$, $j = 1,2$ ds is a differential of arc Γ; s_j are the complex roots (with positive imaginary part) of Lekhnitskii characteristic equation (Bozhydarnyk, 1998; Grigolyuk & Filshtinskiy, 1994); $p_j = \alpha_{11}s_j^2 + \alpha_{12} - \alpha_{16}s_j$, $q_j = \alpha_{12}s_j + \alpha_{22}/s_j - \alpha_{26}$ and α_{ij} are elastic compliances (Bozhydarnyk, 1998; Grigolyuk and Filshtinskiy, 1994).

Assume that the functions u', v', X_Γ, Y_Γ in Eq. (1) are known at Γ. Then according to Maksymovych (2009) one can obtain:

$$\Phi(z_1) = \frac{-v' + s_1 u' + p_1 X_\Gamma + q_1 Y_\Gamma}{\Delta_1 z_1'}$$
$$\Psi(z_2) = \frac{-v' + s_2 u' + p_2 X_\Gamma + q_2 Y_\Gamma}{\Delta_2 z_2'}$$

(2)

where:
$$\Delta_1 = \alpha_{11}(s_1 - s_2)(s_1 - \bar{s_1})(s_1 - \bar{s_2}),$$
$$\Delta_2 = \alpha_{11}(s_2 - s_1)(s_2 - \bar{s_1})(s_2 - \bar{s_2}).$$

2.2. Conditions for the complex functions at the boundary contours

Assume that the projections (X_Γ, Y_Γ) of traction vector and the moment M_L about the origin of all forces applied to the contour L are known. Then one can obtain the following conditions:

$$\int_{L_1} \Phi(z_1)dz_1 = -\frac{p_1 X_L + q_1 Y_L}{\Delta_1}$$

$$\int_{L_2} \Psi(z_2)dz_2 = -\frac{p_2 X_L + q_2 Y_L}{\Delta_2} \tag{3}$$

$$\text{Re}\left[\int_{L_1} \Phi(z_1)dz_1 + \int_{L_2} \Phi(z_2)dz_2\right] = -M_L/2$$

where L_j are the curves in the coordinate systems (x_j, y_j), which are the mappings of the curve L with the affine transformations $x_j = x + \text{Re}(s_j)y$, $y_j = \text{Im}(s_j)y$.

2.3. Integral equations for displacement discontinuities in an infinite cracked plate

The complex variable integral equations for cracked anisotropic plates, in general, are written for the discontinuities of complex functions at cracks, which do not have direct physical meaning. At the same time, complex variable integral equations for isotropic plates are written for the displacement discontinuities, which significantly simplify the study and solution of fracture mechanics problems. In particular, these equations allow considering the problems for cracks with contacting faces. Therefore, this section develops this approach for cracked anisotropic plates.

Assume that the tractions applied to the crack faces are symmetric with respect to a crack. Denoting the displacement discontinuities $[u]$, $[v]$ with g_1, g_2, respectively, based on Eq. (2) one obtains the formulae for discontinuities of complex potentials at the crack:

$$[\Phi(z_1)] = \frac{-g_2' + s_1 g_1'}{\Delta_1 z_1'}, [\Psi(z_2)] = \frac{-g_2' + s_2 g_1'}{\Delta_2 z_2'}$$

Then the following integral formulae can be obtained for an anisotropic plate containing a set of cracks (Bozhydarnyk, 1998; Maksymovych, 2009):

$$\Phi(z_1) = \int_L \frac{G_1'}{t_1 - z_1} ds + \Phi_s(z_1)$$

$$\Psi(z_2) = \int_L \frac{G_2'}{t_2 - z_2} ds + \Psi(z_2) \tag{4}$$

where $G_1' = A_1 g_1' + A_2 g_2'$, $G_2' = B_1 g_1' + B_2 g_2'$ and $A_1 = \frac{is_1}{2\pi\Delta_1}$ $A_2 = \frac{i}{2\pi\Delta_1}$, $B_1 = \frac{is_2}{2\pi\Delta_2}$, $B_2 = \frac{i}{2\pi\Delta_2}$

It should be mentioned that for internal cracks the following crack tip displacement continuity conditions hold:

$$\int_L G_1'(s)ds = 0 \quad (i = 1,2) \tag{5}$$

Now consider the doubly periodic lattice defined by the periods ω_1 and ω_2. The first period is assumed to be real-valued, and the

second one is complex-valued. Then the periods in the mathematical planes z_k are denoted as $\omega_i^{(k)}$ $(i = 1,2)$, moreover $\omega_1^{(k)} = \omega_2$ and $\omega_2^{(k)} = x_\omega + s_k y_\omega$, where $x_\omega + iy_\omega = \omega_2$ and $y_\omega > 0$.

According to Grigolyuk & Filshtinskiy (1994), Sawruk (1981), the integral formulae (4) for the doubly periodic problems can be replaced with:

$$\Phi(z_1) = \int_L G_1'(s)\xi(t_1 - z_1)ds + A_S$$

$$\Psi(z_2) = \int_L G_2'(s)\xi(t_2 - z_2)ds + B_S \tag{6}$$

where $\xi(z_k) = \xi(z_k|\omega_1^{(k)}, \omega_2^{(k)})$ is a Weierstrass zeta function for the periods $\omega_1^{(k)}$ and 2; and A_S, B_S are unknown constants to be determined.

Using the conditions (5) and the property $\xi(z_k + \omega_n^{(k)}) = \xi(z_k) + \delta_n^{(k)}$ it is easy to show that the complex potentials (6) are periodic (thus, the stresses and strains calculated based on these potentials are periodic too). Here $\delta_n^{(k)} = 2\xi(\omega_n^{(k)}/2)$. At the same time, the potentials (6) (and the same as (4)) are dependent on the displacement discontinuities $g_1 + ig_2$ at the curve L. Therefore, (6) presents the solution of doubly periodic problem for cracked domain.

For determination of the constants A_S and B one should first determine the traction vector acting at the lines parallel to the main periods (Grigolyuk & Filshtinskiy, 1994). The projections of the resultant vector of tractions acting at the arbitrary curve AB can be determined with the following equation:

$$Y_{AB} = -2\text{Re}[\varphi(z_1) + \psi(z_2)]_{AB}$$

$$X_{AB} = 2\text{Re}[s_1\varphi(z_1) + \psi\Psi(z_2)]_{AB}$$

First assume that AB is a line parallel to the Ox axis. Then accounting for (6), one obtains that:

$$\varphi(z_1)_{AB} = \int_{z_1}^{z_1+\omega_1^{(1)}} \Phi(z_1)dz_1$$

$$= \int_L G_1'(s)\left(\int_{z_1}^{z_1+\omega_1^{(1)}} \xi(t_1 - z_1)dz_1\right)ds + A_S\,\omega_1^{(1)}$$

According to Sawruk (1981):

$$\int_{z_1}^{z_1+\omega_1^{(1)}} \xi(t_1 - z_1)dz_1 = \delta_1^{(1)}(t_1 - z_1) + const.,$$

therefore:

$$\varphi(z_1)_{AB} = \delta_1^{(1)}\int_L G_1'(s)(t_1 - z_1)ds + A_S\,\omega_1^{(1)}$$

$$= \delta_1^{(1)}\int_L G_1'(s)t_1 ds + A_S\,\omega_1^{(1)}$$

The same concerns the function $\psi(z_2)$:

$$\psi(z_2)_{AB} = \delta_1^{(2)}\int_L G_2'(s)t_2 ds + B_S\,\omega_1^{(2)}$$

Thus, the following relations are obtained for the bottom edge of the representative volume element:

$$Y_1 = -2\mathrm{Re}\big(\delta_1^{(1)}J_1 + \delta_1^{(2)}J_2 + A_S\omega_1^{(1)} + B_S\omega_1^{(2)}\big)$$

$$X_1 = 2\mathrm{Re}\big(s_1\delta_1^{(1)}J_1 + s_2\delta_1^{(2)}J_2 + A_S s_1\omega_1^{(1)} + B_S s_2\omega_1^{(2)}\big)$$

(7)

where $J_k = \int_L G_k'(s)t_k ds$.

Applying the same procedure for the right edge of the representative volume element one obtains:

$$Y_1 = -2\mathrm{Re}\big(\delta_2^{(1)}J_1 + \delta_2^{(2)}J_2 + A_S\omega_2^{(1)} + B_S\omega_2^{(2)}\big)$$

$$X_1 = 2\mathrm{Re}\big(s_1\delta_2^{(1)}J_1 + s_2\delta_2^{(2)}J_2 + A_S s_1\omega_2^{(1)} + B_S s_2\omega_2^{(2)}\big)$$

(8)

The right hand sides of Eqs. (7) and (8) are known and equal:

$$Y_1 = -\omega_1\langle\sigma_y\rangle$$

$$X_1 = -\omega_1\langle\tau_{xy}\rangle$$

$$Y_2 = |\omega_2|(\langle\tau_{xy}\rangle > cos\alpha - \langle\sigma_y\rangle sin\alpha)$$

$$X_2 = |\omega_2|(\langle\sigma_x\rangle > cos\alpha - \langle\tau_{xy}\rangle sin\alpha)$$

where α is an angle between the second period ω_2 and the Oy axis.

Eqs. (7) and (8) are considered as a linear algebraic equations system for determination of the unknown constants A_S and B_S. First consider Eq. (7) and the first equation in (8):

$$-2\mathrm{Re}\big((A_S + B_S)\omega_1 + \delta_1^{(1)}J_1 + \delta_1^{(2)}J_2\big) = Y_1$$

$$2\mathrm{Re}\big(\omega_1(s_1A_S + s_2B_S)\omega_1 + s_1\delta_1^{(1)}J_1 + s_2\delta_1^{(2)}J_2\big) = X_1$$

$$-2\mathrm{Re}\big(x_\omega(A_S + B_S) + y_\omega(s_1A_S + s_2B_S)\big)$$
$$- 2\mathrm{Re}\big(\delta_2^{(1)}J_1 + \delta_2^{(2)}J_2\big) = Y_2$$

These equations result in the condition:

$$2\mathrm{Re}\big[\big(\delta_1^{(1)}\omega_2^{(1)} - \delta_2^{(1)}\omega_1^{(1)}\big)J_1$$
$$+ \big(\delta_1^{(2)}\omega_2^{(2)} - \delta_2^{(2)}\omega_1^{(2)}\big)J_2\big]$$
$$= x_\omega X_1 + y_\omega X_1 + \omega_1 Y_2 = 0$$

Accounting for $\delta_1^{(k)}\omega_2^{(k)} - \delta_2^{(k)}\omega_1^{(k)} = 2\pi i$ one obtains that $4\pi\mathrm{Re}i(J_1 + J_2) = 0$.

The relation:

$$2\mathrm{Re}\left(\frac{s_1^j}{\Delta_1} + \frac{s_2^j}{\Delta_2}\right) = 0 \;\; \text{for } j = 0,1,2$$

shows that this condition is satisfied identically.

Thus, for determination of the unknown constants we have only three equations (Eq. (7) and the second equation in (8)). The solution of this system is sought in the following form:

$$A_S = -\frac{\delta_1^{(1)}}{\omega_1}J_1 + \Phi_\infty + A, \;\; B_S = -\frac{\delta_1^{(2)}}{\omega_1}J_2 + \Psi_\infty + B$$

where Φ_∞ and Ψ_∞ are complex potentials corresponding to the stress state of uncracked plate under the load $\langle\sigma_x\rangle$, $\langle\sigma_y\rangle$, $\langle\tau_{xy}\rangle$ applied at infinity.

Then for determination of the constants A and B one obtains the following system:

$$2\mathrm{Re}(A + B) = 0, \;\; 2\mathrm{Re}(s_1A + s_2B) = 0$$

$$2\mathrm{Re}(As_1^2 + Bs_2^2) = -\frac{4\pi}{y_\omega\omega_1}\mathrm{Re}i(s_1J_1 + s_2J_2)$$

Solving the latter one can obtain the expressions for the unknown constants up to the values which do not influence the stress field:

$$A = -\frac{1}{y_\omega\omega_1\Delta_1}\int_L g_1't_1 ds, \;\; B = -\frac{1}{y_\omega\omega_1\Delta_2}\int_L g_1't_2 ds$$

For convenience one can present the Weierstrass zeta function in the form (Sulym, 2007):

$$\xi(z) = \frac{\delta_1}{\omega_1}z + S(z;\,\omega_1,\omega_2)$$

where:

$$S(z;\,\omega_1,\omega_2) = \frac{\pi}{\omega_1}\bigg\{ctg\frac{\pi z}{\omega_1} + \sum_{n=1}^{N}ctg\left(\frac{\pi z}{\omega_1} + n\pi\frac{\omega_2}{\omega_1}\right)$$
$$+ \sum_{n=1}^{N}ctg\left(\frac{\pi z}{\omega_1} - n\pi\frac{\omega_2}{\omega_1}\right)\bigg\}$$

for $N \to \infty$.

These relations allow to rewrite (6) as:

$$\Phi(z_1) = \int_L [g_1'\Phi_1(t_1 - z_1) + g_2'\Phi_2(t_1 - z_1)]ds + \Phi_\infty$$

(9)

$$\Psi(z_1) = \int_L [g_1'\Psi_1(t_2 - z_2) + g_2'\Psi_2(t_2 - z_2)]ds + \Psi_\infty$$

where $\Phi_1(z) = A_1\left[S_1(z) + \frac{\gamma}{s_1}z\right]$, $\Psi_1(z) = B_1\left[S_z(z) + \frac{\gamma}{s_2}z\right]$
$\Phi_2(z) = A_1S_1(z)$, $\Psi_2(z) = B_1S_2(z)$, $S_k(z) = S\big(z;\,\omega_1,\omega_2^{(k)}\big)$
$\gamma = \frac{2\pi i}{y_\omega\omega_1}$.

The kernels of integral formulae (9) are written in the form of sums of the kernels for singly periodic problems and contain additional terms, which has a multiplier γ. It should be mentioned, that in the literature one can found the attempts to derive the analogous formulae with direct summation. However, now it is obvious that these approaches are incorrect. The reader is referred to Pasternak (2012), where for the first time the mathematically strict and correct approach of direct summation for anisotropic magneto-electroelastic material with doubly periodic sets of defect was presented.

3. NUMERICAL SOLUTION OF THE INTEGRAL EQUATIONS FOR PARTICULAR PROBLEMS

Integral formulae (9) have the same structure as those obtained for other problems of elasticity for cracked anisotropic plates obtained by Bozhydarnyk (1998) and Maksymovych (2009). Therefore, numerical determination of the displacement discontinuities incorporated in these formulae can be determined within the algorithm proposed by Maksymovych (2009). For evaluation of the kernels of the integral equations it is convenient to use the following relation:

$$S(z;\,\omega_1,\omega_2) = \lambda_1\{ctg\lambda_1 z$$

$$+ 4\sin(2\lambda_1 z)\sum_{n=1}^{\infty}\frac{\lambda^n}{(1 - \lambda^n e^{2i\lambda_1 z})(1 - \lambda^n e^{-2i\lambda_1 z})}\}$$

where $\lambda_1 = \frac{\pi}{\omega_1}$, $\lambda = \exp\left(2\pi i \frac{\omega_2}{\omega_1}\right)$ and $|\lambda| < 1$.

This series converges fast. In particular, for isotropic material with a square lattice it is enough to leave only two terms in the sum.

3.1. Verification of the approach

For verification of the proposed approach consider a doubly periodic set of line cracks of length $2l$ inclined at $30°$ to the Ox axis. The centers of the cracks form the equilateral triangular lattice. The only nonzero average stress is $\langle \sigma_y \rangle = p$. The material of the plate is highly anisotropic fiberglass CF1, whose properties are given by Maksymovych (2009). Table 1 compares the normalized stress intensity factors (SIF) $F_{I,II} = K_{I,II}/(p\sqrt{\pi l})$ obtained with the proposed approach and by the boundary element method (BEM) developed by Pasternak (2012) with a crack face meshed with only 20 elements. Good agreement of the results is observed, which testifies the validity and efficiency of the developed approach.

Tab. 1. Verification of the approach

$\lambda_1 = \frac{2l}{\omega_1}$	F_I present	F_I BEM	Deviation %	F_{II} present	F_{II} BEM	Deviation %
0.05	0.739	0.739	0.064	0.426	0.426	0.032
0.10	0.714	0.714	0.029	0.411	0.411	0.070
0.20	0.687	0.687	0.055	0.394	0.394	0.118
0.30	0.733	0.733	0.068	0.421	0.421	0.103
0.40	0.897	0.897	0.034	0.514	0.514	0.069
0.50	1.344	1.344	0.014	0.768	0.768	0.004
0.60	2.355	2.351	0.191	1.280	1.277	0.224
0.70	2.560	2.549	0.412	1.281	1.276	0.368
0.80	2.579	2.565	0.541	1.196	1.190	0.502
0.90	2.586	2.568	0.691	1.112	1.105	0.658
0.95	2.597	2.578	0.713	1.078	1.071	0.671

3.2. Doubly periodic curved cracks with contacting faces

Consider a doubly periodic curved cracks, whose shape is defined by the parabola equation $y = k\left(\frac{x^2}{l^2} - 1\right)$ for $-l \le x \le l$. Here we account for the possible contact of crack faces using the algorithm developed by Maksymovych (2009). The only nonzero average stress is $\langle \sigma_y \rangle = p$. The normalized stress intensity factors $F_{I,II} = K_{I,II}/(p\sqrt{\pi l})$ for the left (A) and right (B) tip of the parabola cracks with $k = 1$ in the isotropic material are presented in Tab. 2.

The calculations held show that the contact of crack faces occurs near the right tip of the crack approximately at a one third of its length. The table also shows significant influence of the account for the crack faces contact on the calculated values of SIF. Following table also shows the results of the problem with the same geometry, however, the material of the medium is anisotropic fiberglass CF1 (CF190 corresponds to the same material with the principal anisotropy axes rotated at a right angle).

For all considered particular problems the crack faces contact

occurs near the right tip, excepting material CF190 and $\frac{\omega_1}{k} = 2.5$, where the faces contact at the right of the crack center. Tab. 3 shows that for the contact of crack faces the SIF K_{IB} for an anisotropic material (in contrast with the isotropic one) differs from zero, moreover, for the CF190 material SIF is significantly big. To testify this phenomenon, consider the crack tip normal displacement discontinuities. According to Bozhydarnyk (1998) they equal:

$$[u_n] = 4a_{11}\frac{\sqrt{r}}{\sqrt{2\pi}}(u_{11}K_I + u_{12}K_{II}) \tag{10}$$

where r is a distance to the tip; $u_{11} = -\text{Re}[i(s_1 - \bar{s}_2)g_2\bar{g}_1]$, $u_{12} = \text{Re}[i(s_1 - \bar{s}_2)d_2\bar{g}_1]$, $d_j = \cos\varphi + s_j\sin\varphi$, $g_j = \sin\varphi - s_j\cos\varphi$, and φ is an angle between the tangent to the crack at its tip and Ox axis.

It should be mentioned that for an orthotropic material, for which $s_j = i\beta_j$, the following relations hold:

$$u_{11} = (\beta_1 + \beta_2)\cos^2\varphi(k^2 + \beta_1\beta_2),$$
$$u_{12} = -(\beta_1 + \beta_2)\cos^2\varphi k(1 - \beta_1\beta_2).$$

Tab. 2. Doubly periodic parabola cracks in the isotropic medium

$\frac{\omega_1}{l}$	F_{IA}	F_{IIA}	F_{IB}	F_{IIB}	F_{IA}	F_{IIA}	F_{IB}	F_{IIB}
	Not accounting for crack faces contact				Accounting for crack faces contact			
2.5	1.782	0.880	-1.782	0.880	1.684	0.434	0	0.941
3.0	1.394	0.709	-1.394	0.709	1.340	0.412	0	0.783
3.5	1.249	0.638	-1.250	0.638	1.207	0.395	0	0.717
4.0	1.174	0.599	-1.175	0.599	1.137	0.384	0	0.681
4.5	1.129	0.575	-1.129	0.575	1.095	0.376	0	0.659
5.0	1.098	0.558	-1.098	0.558	1.066	0.371	0	0.644
5.5	1.077	0.547	-1.077	0.547	1.046	0.366	0	0.633
6.0	1.061	0.538	-1.061	0.538	1.032	0.363	0	0.626
6.5	1.048	0.532	-1.049	0.532	1.021	0.360	0	0.620
7.0	1.039	0.527	-1.039	0.527	1.012	0.358	0	0.615

Tab. 3. Doubly periodic parabola cracks in the anisotropic medium

$\frac{\omega_1}{l}$	F_{IA}	F_{IIA}	F_{IB}	F_{IIB}	F_{IA}	F_{IIA}	F_{IB}	F_{IIB}	$\frac{F_{IB}}{F_{IIB}}$
	CF1				CF190				
2.5	1.028	-0.604	0.162	0.393	1.633	-0.495	-0.525	0.605	-0.867
3.0	0.880	-0.394	0.065	0.157	1.399	-0.372	-0.560	0.521	-1.075
3.5	0.826	-0.326	0.025	0.061	1.303	-0.317	-0.533	0.495	-1.075
4.0	0.799	-0.298	0.003	0.007	1.253	-0.283	-0.520	0.484	-1.075
4.5	0.784	-0.286	-0.012	-0.028	1.221	-0.260	-0.514	0.478	-1.075
5.0	0.775	-0.281	-0.021	-0.052	1.201	-0.243	-0.510	0.474	-1.075
5.5	0.769	-0.280	-0.028	-0.069	1.187	-0.230	-0.507	0.472	-1.075
6.0	0.766	-0.282	-0.033	-0.081	1.177	-0.219	-0.505	0.470	-1.075
6.5	0.764	-0.284	-0.037	-0.089	1.170	-0.211	-0.503	0.468	-1.075
7.0	0.763	-0.288	-0.039	-0.095	1.165	-0.203	-0.501	0.466	-1.075

From Eq. (10) it follows that under the crack faces contact at the tip the following condition hold:

$$\frac{K_{\mathrm{I}}}{K_{\mathrm{II}}} = -\frac{u_{12}}{u_{11}} \qquad (11)$$

For the CF190 material $k = 2$, and thus, $u_{12}/u_{11} = 1.0751$. One can see that the ration of SIFs presented in the last column of Tab. 3 is in good agreement with this estimation, thus, the crack faces contact condition (11) holds with high accuracy.

4. CONCLUSION

The paper derives compact and easy to use singular integral equations for doubly periodic cracks in an anisotropic medium. The study of the influence of anisotropy and contact of crack faces showed its significance in the calculated values of stress intensity factors. Also it is proved the mode I SIF can be nonzero for an anisotropic material with crack, which faces are in contact.

REFERENCES

1. **Bozhydarnyk V. V.** (1998), *Two-dimensional problems of the theory of elasticity and thermoelasticity of structurally inhomogeneous solids*, Svit, Lviv (in Ukrainian).
2. **Chen Y. Z., Hasebe N., Lee K. Y.** (2003), *Multiple crack problems in elasticity*, Vol. 1. WIT, London.
3. **Grigolyuk E. I., Filshtinskiy L. A.** (1994), *Regular piecewise-homogeneous structures with defects*, Fizmatgiz, Moscow (in Russian).
4. **Maksymovych O.** (2009), Calculation of the stress state of anisotropic plates with holes and curvilinear cracks accounting for contact of their faces, *Herald of Ternopil State Technical University,* 2009, No. 3, 36–42 (in Ukrainian).
5. **Malits P.** (2010), Doubly periodic array of thin rigid inclusions in an elastic solid, *Q. J. Mech. Appl. Math.*, 63, No. 2, 115–144.
6. **Pasternak I.** (2012), Doubly periodic arrays of cracks and thin inhomogeneities in an infinite magnetoelectroelastic medium, *Eng. Anal. Bound. Elem.*, 36, No. 5, 799–811.
7. **Sawruk M. P.** (1981), *Two-dimensional problems of elasticity for solids with cracks*, Naukova dumka, Kyiv (in Russian).
8. **Sulym H. T.** (2007), *Bases of mathematical theory of thermoelastic equilibrium of deformable solids with thin inclusions*, NTSh, Lviv (in Ukrainian).
9. **Wang G. S.** (2004), The interaction of doubly periodic cracks, *Theor. Appl. Fract. Mech.*, 42, 249–294.
10. **Xiao J., Jiang C.** (2009), Exact solution fro orthotropic materials weakened by doubly periodic cracks of unequal size under antiplane shear, *Acta Mechanica Solida Sinica,* 22, No. 1, 53–63.
11. **Xiao J. H., Xu Y. L., Jiang C. P.** (2011), Exact solution to the antiplane problem of doubly periodic conducting rigid line inclusions of unequal size in piezoelectric materials, *Z. Angew. Math. Mech.*, 91, No. 5, 413–424.

MINIMUM ENERGY CONTROL OF 2D POSITIVE CONTINUOUS-DISCRETE LINEAR SYSTEMS

Tadeusz KACZOREK*

*Faculty of Electrical Engineering, Bialystok University of Technology, ul. Wiejska 45D, 15-351 Bialystok, Poland

kaczorek@isep.pw.edu.pl

Abstract: The minimum energy control problem for the 2D positive continuous-discrete linear systems is formulated and solved. Necessary and sufficient conditions for the reachability at the point of the systems are given. Sufficient conditions for the existence of solution to the problem are established. It is shown that if the system is reachable then there exists an optimal input that steers the state from zero boundary conditions to given final state and minimizing the performance index for only one step ($q = 1$). A procedure for solving of the problem is proposed and illustrated by a numerical example.

Key words: 2D Continuous-Discrete, Linear, Positive, Reachability, Minimum Energy Control

1. INTRODUCTION

A dynamical system is called positive if its trajectory starting from any nonnegative initial state remains forever in the positive orthant for all nonnegative inputs. An overview of state of the art in positive theory is given in the monographs Farina and Rinaldi (2000) and Kaczorek (2001). Variety of models having positive behavior can be found in engineering, economics, social sciences, biology and medicine, etc.

The positive continuous-discrete 2D linear systems have been introduced in Kaczorek (1998), positive hybrid linear systems in Kaczorek (2007) and the positive fractional 2D hybrid systems in Kaczorek (2008a). Different methods of solvability of 2D hybrid linear systems have been discussed in Kaczorek et al. (2008) and the solution to singular 2D hybrid linear systems has been derived in Sajewski (2009). The realization problem for positive 2D hybrid systems has been addressed in Kaczorek (2008b). Some problems of dynamics and control of 2D hybrid systems have been considered in Dymkov et al. (2004) and Gałkowski et al. (2003). The problems of stability and robust stability of 2D continuous-discrete linear systems have been investigated in Bistritz (2003), Busłowicz (2010a, b), Narendra (2010), Sajewski (2009) and Xiao (2001, 2003). Recently the stability and robust stability of general model and of Roesser type model of scalar continuous-discrete linear systems have been analyzed by Busłowicz (2010). New stability tests for positive standard and fractional linear systems have been proposed in Kaczorek (2011a). Stability of continuous-discrete 2D linear systems has been considered in Kaczorek (2011b).

The minimum energy control problem for standard linear systems has been formulated and solved by Klamka (1976, 1983, 1991) and for 2D linear systems with variable coefficients in Kaczorek and Klamka (1986). The controllability and minimum energy control problem of fractional discrete-time linear systems has been investigated by Klamka (2010). The minimum energy control of fractional positive continuous-time linear systems has been addressed in Kaczorek (2012, 2014) and for descriptor positive discrete-time linear systems in Kaczorek (2013).

In this paper the minimum energy control problem for positive 2D continuous-discrete linear systems will be formulated and solved.

The paper is organized as follows. In section 2 the basic definitions and theorems of the positive continuous-discrete linear systems are recalled. Necessary and sufficient conditions for the reachability of the positive systems are given in section 3. The minimum energy control problem is formulated and solved in section 4. A procedure for computation of the optimal inputs and the minimum value of the performance index are proposed and illustrated by numerical example in section 5. Concluding remarks are given in section 6.

The following notation will be used: $\Re$ – the set of real numbers, $\Re^{n \times m}$ – the set of $n \times m$ real matrices, $\Re_+^{n \times m}$ – the set of $n \times m$ matrices with nonnegative entries and $\Re_+^n = \Re_+^{n \times 1}$, M_n – the set of $n \times n$ Metzler matrices (real matrices with nonnegative off-diagonal entries), I_n – the $n \times n$ identity matrix.

2. PRELIMINERIES

Consider the general model of linear continuous-discrete system described by the equation:

$$\dot{x}(t, i+1) = A_0 x(t, i) + A_1 \dot{x}(t, i) + A_2 x(t, i+1)$$
$$+ B_0 u(t, i) + B_1 \dot{u}(t, i) + B_2 u(t, i+1) \tag{1}$$

where: $\dot{x}(t, i) = \frac{\partial x(t,i)}{\partial t}$, $x(t, i) \in \Re^n$, $u(t, i) \in \Re^m$ are the state and input vectors and $A_k \in \Re^{n \times n}$, $B_k \in \Re^{n \times m}$, $k = 0, 1, 2$.

Boundary conditions for (1) are given by:

$$x_{0i} = x(0, i), i \in Z_+,$$
$$x_{t0} = x(t, 0), \dot{x}_{t0} = \dot{x}(t, 0), t \in \Re_+ \tag{2}$$

The transition matrix of the model (1) is defined as follows:

$$T_{ij} = \begin{cases} I_n, \text{for } i = 1 = 0 \\ A_0 T_{i-1,j-1} + A_1 T_{i,j-1} + A_2 T_{i-1,j} \\ = T_{i-1,j-1} A_0 + T_{i,j-1} A_1 + T_{i-1,j} A_2, \text{for } \substack{i+j > 0 \\ i,j \in Z_+} \\ 0, \text{for } i > 0 \text{ or } j < 0 \end{cases} \tag{3}$$

Theorem 1. The solution of the equation (1) with boundary conditions (2) has the form (proof is given in Kaczorek (2012)):

$$
\begin{aligned}
x(t,i) \\
= \sum_{k=0}^{\infty}\sum_{l=0}^{\infty}\Bigg(& T_{k,i-l-1}B_0\int_0^t \frac{(t-\tau)^k}{k!}u(\tau,l)d\tau \\
& + T_{k,i-l}B_2\int_0^t \frac{(t-\tau)^k}{k!}u(\tau,l)d\tau \\
& - T_{k,i-l-1}B_1\frac{t^k}{k!}u(0,l) + T_{k,i-l}\frac{t^k}{k!}x(0,l) \\
& - T_{k,i-l-1}A_1\frac{t^k}{k!}x(0,l)\Bigg) \\
+ \sum_{k=1}^{\infty}\sum_{l=0}^{\infty}\Bigg(& T_{k,i-l-1}B_1\int_0^t \frac{(t-\tau)^{k-1}}{(k-1)!}u(\tau,l)d\tau\Bigg) \\
+ \sum_{l=0}^{\infty} & T_{0,i-l-1}B_1 u(t,l) \\
- \sum_{k=0}^{\infty}\Bigg(& T_{k,i}B_2\int_0^t \frac{(t-\tau)^k}{k!}u(\tau,0)d\tau \\
& + T_{k,i}A_2\int_0^t \frac{(t-\tau)^k}{k!}x(\tau,0)d\tau + T_{k,i}\frac{t^k}{k!}x(0,0)\Bigg) \\
+ \sum_{k=1}^{\infty}\Bigg(& T_{k,i}\int_0^t \frac{(t-\tau)^{k-1}}{(k-1)!}x(\tau,0)d\tau\Bigg) + T_{0,i}x(t,0)
\end{aligned}
\tag{4}
$$

Definition 1. The general model (1) is called positive if $x(t,i)\in \Re_+^n$, $t\in\Re_+$, $i\in Z_+$ for any boundary conditions $x_{0i}\in\Re_+^n$, $x_{t0}\in\Re_+^n, \dot{x}_{t0}\in\Re_+^n, t\in\Re_+$ and all inputs $u(t,i)\in\Re_+^m$, $\dot{u}(t,i)\in\Re_+^m, t\in\Re_+, i\in Z_+$.

Theorem 2. The general model (2.1) is positive if and only if:

$$
\begin{aligned}
& A_2\in M_n, \qquad A_0,\,A_1\in\Re_+^{n\times n} \\
& A_0 + A_1A_2\in\Re_+^{n\times n},\ \ B_0,B_1,B_2\in\Re_+^{n\times m}
\end{aligned}
\tag{5}
$$

Proof is given in in Kaczorek (2012).

3. REACHABILITY OF POSITIVE SYSTEMS

Definition 2. The model (1) is called reachable at the point (t_f,q) if for any given final state $x_f\in\Re^n$ there exists an input $u(t,i),\ 0\le t\le t_f,\ 0\le i\le q$ which steers the system form zero boundary conditions to the state x_f, i.e. $(t_f,q)=x_f$.

A square real matrix is called monomial if its every column and its every row has only one positive entry and the remaining entries are zero. The inverse of monomial matrix is also a monomial matrix (Kaczorek, 2012).

Theorem 3. The model (1) with $B_1 = B_2 = 0$ is reachable at the point $(t_f,1)$ if and only if the matrix $A_2\in M_n$ is diagonal and the matrix $B_0\in\Re_+^{n\times m}$ is monomial.

Proof. Sufficiency. If $A_2\in M_n$ is diagonal then $e^{A_2 t}$ is also diagonal and if $B_0\in\Re_+^{n\times m}$ is monomial then $B_0B_0^T$ is also monomial. In this case the matrix:

$$
R_f = \int_0^{t_f} e^{A_2\tau}B_0B_0^T e^{A_2^T\tau}d\tau, \quad t_f > 0
\tag{6}
$$

is also monomial and $R_f^{-1}\in\Re_+^{n\times n}$.

The input:

$$
u(t) = u(t,0) = B_0^T e^{A_2^T(t_f-\tau)}R_f^{-1}x_f
\tag{7}
$$

steers the state of the system (1) from zero boundary conditions to x_f. The solution of (1) for $i = 0$, $t = t_f$ has the form:

$$
x(t_f,1) = \int_0^{t_f} e^{A_2(t_f-\tau)}B_0 u(\tau)d\tau
\tag{8}
$$

and substitution (7) onto (8) we obtain:

$$
x(t_f,1) = \int_0^{t_f} e^{A_2(t_f-\tau)}B_0B_0^T e^{A_2^T(t_f-\tau)}d\tau R_f^{-1}x_f = x_f
\tag{9}
$$

The necessity can be proved in a similar way as in Kaczorek (2012, 2013a).

4. MINIMUM ENERGY CONTROL PROBLEM FOR POSITIVE SYSTEMS WITH BOUNDED INPUTS

4.1. Problem formulation

Consider the positive 2D continuous-discrete system (1) with $A_2\in M_n$ and $B_0\in\Re_+^{n\times m}$ monomial and $B_1 = B_2 = 0$. If the system is reachable in time $t\in[0,t_f]$, then usually there exists many different inputs $u(t)\in\Re_+^n$ that steers the state of the system from zero boundary conditions to $x_f\in\Re_+^n$. Among these inputs we are looking for an input $u(t)\in\Re_+^n$ that minimizes the performance index:

$$
I(u) = \int_0^{t_f} u^T(\tau)Qu(\tau)d\tau
\tag{10}
$$

where: $Q\in\Re_+^{n\times n}$ is a symmetric positive defined matrix and $Q^{-1}\in\Re_+^{n\times n}$.

The minimum energy control problem for the positive 2D continuous-discrete linear systems (1) can be stated as follows: Given the matrices: diagonal $A_2\in M_n$, monomial $B_0\in\Re_+^{n\times n}$, t_f, $q = 1$ and $Q\in\Re_+^{n\times n}$ of the performance index (10), $x_f\in\Re_+^n$ and $t_f > 0$, find an input $u(t)\in\Re_+^n$ for $t\in[0,t_f]$ that steers the state vector of the system from zero boundary conditions to $x_f\in\Re_+^n$ and minimizes the performance index (10).

4.2. Problem solution

To solve the problem we define the matrix:

$$
W = W(t_f,Q) = \int_0^{t_f} e^{A_2(t_f-\tau)}B_0Q^{-1}B_0^T e^{A_2^T(t_f-\tau)}d\tau
\tag{11}
$$

From (11) and Theorem 3 it follows that the matrix (11) is monomial if and only if the positive system (1) is reachable at the point $[t_f,1]$. In this case we may define the input:

$$
\hat{u}(t) = Q^{-1}B_0^T e^{A^T(t_f-\tau)}W^{-1}x_f \text{ for } t\in[0,t_f]
\tag{12}
$$

Note that the input (12) satisfies the condition $\hat{u}(t)\in\Re_+^n$ for $t\in[0,t_f]$ if:

$$
Q^{-1}\in\Re_+^{n\times n} \text{ and } W^{-1}\in\Re_+^{n\times n}
\tag{13}
$$

Theorem 4. Let the positive system (1) be reachable at the point $[t_f, 1]$ and let $\bar{u}(t) \in \Re_+^n$ for $t \in [0, t_f]$ be an input that steers the state of the positive system (1) from zero boundary conditions to $x_f \in \Re_+^n$. Then the input (12) also steers the state of the system from zero boundary conditions to $x_f \in \Re_+^n$ and minimizes the performance index (10), i.e. $I(\hat{u}) \le I(\bar{u})$. The minimal value of the performance index (10) is equal to:

$$I(\hat{u}) = x_f^T W^{-1} x_f \qquad (14)$$

Proof. If the conditions (13) are met then the input (12) is well defined and $\hat{u}(t) \in \Re_+^n$ for $t \in [0, t_f]$. We shall show that the input steers the state of the system from zero boundary conditions to $x_f \in \Re_+^n$. Substitution of (12) into (8) for $t = t_f$ and zero boundary conditions yields:

$$
\begin{aligned}
x(t_f, 1) &= \int_0^{t_f} e^{A_2(t_f-\tau)} B_0 \hat{u}(\tau) d\tau \\
&= \int_0^{t_f} e^{A_2(t_f-\tau)} B_0 Q^{-1} B_0^T e^{A_2^T(t_f-\tau)} d\tau W^{-1} x_f = x_f
\end{aligned}
\qquad (15)
$$

since (11) holds. By assumption the inputs $\bar{u}(t)$ and $\hat{u}(t)$, $t \in [0, t_f]$ steers the state of the system from zero boundary conditions to $x_f \in \Re_+^n$. Hence:

$$
\begin{aligned}
x_f &= \int_0^{t_f} e^{A_2(t_f-\tau)} B_0 \bar{u}(\tau) d\tau \\
&= \int_0^{t_f} e^{A_2(t_f-\tau)} B_0 \hat{u}(\tau) d\tau
\end{aligned}
\qquad (16a)
$$

or:

$$\int_0^{t_f} e^{A_2(t_f-\tau)} B_0 [\bar{u}(\tau) - \hat{u}(\tau)] d\tau = 0 \qquad (16b)$$

By transposition of (16b) and postmultiplication by $W^{-1} x_f$ we obtain:

$$\int_0^{t_f} [\bar{u}(\tau) - \hat{u}(\tau)]^T B_0^T e^{A_2^T(t_f-\tau)} d\tau W^{-1} x_f = 0 \qquad (17)$$

Substitution of (12) into (17) yields:

$$
\begin{aligned}
&\int_0^{t_f} [\bar{u}(\tau) - \hat{u}(\tau)]^T B_0^T e^{A_2^T(t_f-\tau)} d\tau W^{-1} x_f \\
&= \int_0^{t_f} [\bar{u}(\tau) - \hat{u}(\tau)]^T Q(\tau) d\tau = 0
\end{aligned}
\qquad (18)
$$

Using (18) it is easy to verify that:

$$
\begin{aligned}
\int_0^{t_f} \bar{u}(\tau)^T Q \bar{u}(\tau) d\tau &= \int_0^{t_f} \hat{u}(\tau)^T Q \hat{u}(\tau) d\tau \\
&+ \int_0^{t_f} [\bar{u}(\tau) - \hat{u}(\tau)]^T Q [\bar{u}(\tau) - \hat{u}(\tau)] d\tau
\end{aligned}
\qquad (19)
$$

From (19) it follows that $I(\hat{u}) \le I(\bar{u})$ since the second term in the right-hand side of the inequality is nonnegative.

To find the minimal value of the performance index (10) we substitute (12) into (10) and we obtain:

$$
\begin{aligned}
I(\hat{u}) &= \int_0^{t_f} \hat{u}^T(\tau) Q \hat{u}(\tau) d\tau \\
&= x_f^T W^{-1} \int_0^{t_f} e^{A_2(t_f-\tau)} B_0 Q^{-1} B_0^T e^{A_2^T(t_f-\tau)} d\tau W^{-1} \\
&= x_f^T W^{-1} x_f
\end{aligned}
\qquad (20)
$$

since (11) holds.

We have the following two important conclusions:

Conclusion 1. If the matrix $A_2 \in M_n$ is diagonal and the matrix $B_0 \in \Re_+^{n \times m}$ is monomial then there exists an input (7) that steers the state of the positive system (1) from zero boundary conditions to $x_f \in \Re_+^n$ and minimize the performance index (10).

Conclusion 2. For $q = 1$ the optimal input (7) and the minimal value of the performance index (14) are independent of the matrices A_0 and A_1 of the positive system (1).

The considerations can be easily extended to $q > 1$.

5. PROCEDURE AND EXAMPLE

From the considerations of section 4 we have the following procedure for computation the optimal inputs that steers the state of the system from zero boundary conditions to $x_f \in \Re_+^n$ and minimize the performance index (10).

Procedure 1.

Step 1. Knowing $A_2 \in M_n$ compute $e^{A_2 t}$.

Step 2. Knowing the matrices A_2, B_0, Q for some t_f and using (11) compute the matrix W.

Step 3. Using (12) compute $\hat{u}(\tau)$.

Step 4. Using (10) compute the minimal value of the performance index $I(\hat{u})$.

Example 1. Consider the positive system (1) with matrices:

$$A_2 = \begin{bmatrix} -1 & 0 \\ 0 & -2 \end{bmatrix}, \quad B_0 = \begin{bmatrix} 0 & 1 \\ 1 & 0 \end{bmatrix} \qquad (21)$$

and the performance index (10) with:

$$Q = \begin{bmatrix} 2 & 0 \\ 0 & 2 \end{bmatrix} \qquad (22)$$

Compute the optimal input $\hat{u}(t)$ for $t \in [0, 1]$ and $q = 1$ that steers the state of the system from zero boundary conditions to $x_f = [1 \quad 1]^T \in \Re_+^2$ (T denote the transpose) and minimize the performance index.

By Theorem 3 the positive system (1) with (21) is reachable at the point $(t_f = 1, q = 1)$. Using the Procedure 1 we obtain the following:

Step 1. In this case we have:

$$e^{A_2 t} = \begin{bmatrix} e^{-t} & 0 \\ 0 & e^{-2t} \end{bmatrix} \qquad (23)$$

Step 2. Using (11), (21) and (23) we obtain:

$$
\begin{aligned}
W &= \int_0^{t_f} e^{A_2(t_f-\tau)} B_0 Q^{-1} B_0^T e^{A_2^T(t_f-\tau)} d\tau \\
&= \int_0^{t_f} \begin{bmatrix} e^{-2\tau} & 0 \\ 0 & e^{-4\tau} \end{bmatrix} = \begin{bmatrix} \frac{1}{4}(1-e^{-2}) & 0 \\ 0 & \frac{1}{8}(1-e^{-4}) \end{bmatrix}
\end{aligned}
\qquad (24)
$$

Step 3.   Using (12) and (22)-(24) we obtain:

$$\hat{u} = Q^{-1} B_0^T e^{A_2^T(t_f-\tau)} W^{-1} x_f$$

$$= \frac{1}{2} \begin{bmatrix} 0 & e^{2(t-1)} \\ e^{(t-1)} & 0 \end{bmatrix} \begin{bmatrix} \frac{1}{4}(1-e^{-2}) & 0 \\ 0 & \frac{1}{8}(1-e^{-4}) \end{bmatrix}^{-1} \begin{bmatrix} 1 \\ 1 \end{bmatrix}$$

$$= \begin{bmatrix} \dfrac{4e^{2(t-1)}}{(1-e^{-4})} \\ \dfrac{2e^{(t-1)}}{(1-e^{-2})} \end{bmatrix}$$

(25)

Step 4.   The minimal value of the performance index is equal to:

$$I(\hat{u}) = x_f^T W^{-1} x_f$$

$$= \begin{bmatrix} 1 & 1 \end{bmatrix} \begin{bmatrix} \frac{1}{4}(1-e^{-2}) & 0 \\ 0 & \frac{1}{8}(1-e^{-4}) \end{bmatrix}^{-1} \begin{bmatrix} 1 \\ 1 \end{bmatrix}$$

$$= \frac{4}{(1-e^{-2})} + \frac{8}{(1-e^{-4})}$$

(26)

6. CONCLUDING REMARKS

The minimum energy control problem for the 2D positive continuous-discrete linear systems has been formulated and solved. Necessary and sufficient conditions for the reachability at the point $(t_f, q = 1)$ of the systems have been established (Theorem 3). Sufficient conditions for the existence of solution to the minimum energy control problem of the positive 2D continuous-discrete linear systems have been given (Theorem 4). The procedure for computation of the optimal input and the minimal value of performance index has been proposed and illustrated by numerical example. It has been shown that if the system is reachable then there exists an optimal input that steers the state from zero boundary conditions to given final state and minimizing the performance index for only one step for $q = 1$. The consideration can be easily extended to $q > 1$ and for (1) with nonzero matrices $B_k, k = 0,1,2$. In the subsequent paper the considerations will be extended to the descriptor positive 2D continuous-discrete linear systems.

REFERENCES

1. **Bistritz Y.** (2003), A stability test for continuous-discrete bivariate polynomials, *Proc. Int. Symp. on Circuits and Systems*, Vol. 3, 682-685.
2. **Busłowicz M.** (2010), Robust stability of the new general 2D model of a class of continuous-discrete linear systems, *Bull. Pol. Acad. Sci. Techn.*, Vol. 57, No. 4, 561-565.
3. **Busłowicz M.** (2010), Stability and robust stability conditions for a general model of scalar continuous-discrete linear systems, *Measurement Automation and Monitoring*, Vol. 56, No. 2, 133-135.
4. **Dymkov M., Gaishun I., Rogers E., Gałkowski K. and Owens D.H.** (2004), Control theory for a class of 2D continuous-discrete linear systems, *Int. J. Control,* Vol. 77, No. 9, 847-860.
5. **Farina L. and Rinaldi S.** (2000), *Positive Linear Systems; Theory and Applications*, J. Wiley, New York.
6. **Gałkowski K., Rogers E., Paszke W. and Owens D.H.** (2003), Linear repetitive process control theory applied to a physical example, *Int. J. Appl. Math. Comput. Sci.*, Vol. 13, No. 1, 87-99.
7. **Kaczorek T.** (1998), Reachability and minimum energy control of positive 2D continuous-discrete systems, *Bull. Pol. Acad. Sci. Tech.*, Vol. 46, No. 1, 85-93.
8. **Kaczorek T.** (2001), *Positive 1D and 2D systems*, Springer Verlag, London.
9. **Kaczorek T.** (2007), Positive 2D hybrid linear systems, *Bull. Pol. Acad. Sci. Tech.*, Vol. 55, No. 4, 351-358.
10. **Kaczorek T.** (2008a), Positive fractional 2D hybrid linear systems, *Bull. Pol. Acad. Tech.*, Vol. 56, No. 3, 273-277.
11. **Kaczorek T.** (2008b), Realization problem for positive 2D hybrid systems, *COMPEL*, Vol. 27, No. 3, 613-623.
12. **Kaczorek T.** (2011a), New stability tests of positive standard and fractional linear systems, *Circuit and Systems*, Vol. 2, No. 4, 261-268.
13. **Kaczorek T.** (2011b), Stability of continuous-discrete linear systems described by general model, *Bull. Pol. Acad. Sci. Tech.*, Vol. 59, No. 2, 189-193.
14. **Kaczorek T.** (2012), *Selected Problems of Fractional Systems Theory*, Springer-Verlag, Berlin.
15. **Kaczorek T.** (2013), Minimum energy control of fractional positive continuous-time linear systems, Proc. of Conf. MMAR, Międzyzdroje, Poland.
16. **Kaczorek T.** (2013), *Minimum energy control of positive fractional descriptor continous time linear systems*, IET Control Theory and Applications, Vol. 8 No. 4, 219-225.
17. **Kaczorek T.** (2014), Minimum energy control of descriptor positive discrete-time linear systems, Compel, Vol. 33, No.3, 1-14.
18. **Kaczorek T., Klamka J.** (1986), Minimum energy control of 2D linear systems with variable coefficients, *Int. J. of Control*, Vol. 44, No. 3, 645-650.
19. **Kaczorek T., Marchenko V. and Sajewski Ł.** (2008), Solvability of 2D hybrid linear systems - comparison of three different methods, *Acta Mechanica et Automatica*, Vol. 2, No. 2, 59-66.
20. **Klamka J.** (1976), Relative controllability and minimum energy control of linear systems with distributed delays in control, *IEEE Trans. Autom. Contr.*, Vol. 21, No. 4, 594-595.
21. **Klamka J.** (1983), Minimum energy control of 2D systems in Hilbert spaces, *System Sciences*, Vol. 9, No. 1-2, 33-42.
22. **Klamka J.** (1991), *Controllability of Dynamical Systems*, Kluwer Academic Press, Dordrecht.
23. **Klamka J.** (2010), Controllability and minimum energy control problem of fractional discrete-time systems, Chapter in *New Trends in Nanotechnology and Fractional Calculus*, Eds. Baleanu D., Guvenc Z.B., Tenreiro Machado J.A., Springer-Verlag, New York, 503-509.
24. **Narendra K.S. and Shorten R.** (2010), Hurwitz stability of Metzler matrices, *IEEE Trans. Autom. Contr.*, Vol. 55, No. 6, 1484-1487.
25. **Sajewski Ł.** (2009), Solution of 2D singular hybrid linear systems, *Kybernetes*, Vol. 38, No. 7/8, 1079-1092.
26. **Xiao Y.** (2001), Stability test for 2-D continuous-discrete systems, *Proc. 40th IEEE Conf. on Decision and Control*, Vol. 4, 3649-3654.
27. **Xiao Y.** (2003), Stability, controllability and observability of 2-D continuous-discrete systems, *Proc. Int. Symp. on Circuits and Systems*, Vol. 4, 468-471.